UCLouvain
Institute for Information
and Communication Technologies,
Electronics and Applied Mathematics

Flexible MEMS-based Platform for High-Strain Characterization of Silicon and Vanadium Dioxide Devices

Loïc LAHAYE

Thesis submitted in partial fulfillment
of the requirements for the degree of
Doctor in Applied Sciences

Dissertation committee:

Prof. Denis FLANDRE (UCLouvain, advisor)
Prof. Jean-Pierre RASKIN (UCLouvain, advisor)
Prof. Dimitri LEDERER (UCLouvain, secretary)
Prof. Adrian M. IONESCU (EPFL, Switzerland)
Prof. Aurelian CRUNTEANU (Université de Limoges, France)
Prof. Laurent FRANCIS (UCLouvain, chairman)

Version of September 4, 2026.

N'oublie pas qu'il y a demain ...

Abstract

In the recent years, the field of strain sensing shifted from the development of conventional strain gauges to the engineering of novel, multifunctional sensors. Strain sensors found new application domains in smart packaging, wearable sensors and health monitoring that require conformable gauges sensitive to multiple physical stimuli in addition to strain such as temperature. Research initially went toward the use of organic piezoresistive materials that can be rendered multifunctional and propose simple read-out circuitry. However, they have limitations in terms of long-term reliability, miniaturisation and output signal quality. To try and cope with these issues, conventional inorganic materials such as silicon or germanium were fabricated onto flexible substrates but do not propose multifunctional sensing.

Vanadium dioxide, VO_2, is a promising candidate to fill this need since the VO_2 crystal is able to transition between different crystallographic states when stimulated. Depending on the magnitude of the stimulation, it can either partially transition from an M1 to an M2 state or completely transition from an insulating M1 state to a metallic R one. These transitions lead to massive changes in the material properties and can be triggered by mechanical, electrical, thermal, optical and magnetic stimulation, making VO_2 multifunctional. Looking into strain, the mechanical stimulation generates a partial M1 to M2 reconfiguration accompanied by a massive change of resistivity with reported gauge factors between 250 and 500. Researchers have tried to integrate vanadium dioxide devices onto a flexible substrate for multifunctional sensing but had to use either low-temperature deposition or complex layer transfer. The first approach gives low-quality vanadium dioxide due to low crystallinity while the second is complex and hard to scale. This work proposes to integrate high-quality, thermally annealed, sputtered p-VO_2 on a thin-polyimide membrane to characterise its gauge

factor under high-strain.

The first chapter proposes a monolithic process for the fabrication of microelectronics on a flexible membrane for high-strain studies. The process integrates single crystal silicon (c-Si) devices with electrical connections on a 3.6 µm-thick and 2.7 mm-diameter PI membrane, without limitation or complex layer transfer. c-Si is used instead of p-VO_2 to serve as a first demonstrator. It introduces the methodology and tools used in the rest of the work.

The second chapter introduces a *Comsol* FEM model to study the behavior of the bulged membrane and compute the local strain field inside the c-Si devices. The bulged membrane is observed to enter in a plastic deformation regime and to diverge from the expected cube-root deflection profile. The plastic deformation of the membrane is simulated by the *Swift* plastic model in *Comsol*. The *Comsol* model is fitted on an *in situ* measurement of the membrane deflection and the local strain field in the c-Si is computed. An asymmetrical, biaxial strain field with a maximum magnitude of 0.36 % of local strain is obtained in the c-Si. The strain field is checked by computing the expected silicon Raman peak-shift using the Ganesan equation and comparing it to an experimental measurement.

The third chapter explores the integration of thermally annealed, sputtered p-VO_2 on a polyimide membrane. A 2.5 mm-wide and 3.2 µm-thick polyimide membrane carrying a 220 nm-thick layer of p-VO_2 is fabricated. The deposition and characterization process is presented. The study shows that p-VO_2 requires an adhesion layer to stick to the polyimide. The fabricated sample is used to measure the Young's modulus of p-VO_2 since its value is not readily available in literature. A Young's modulus of 120 GPa is found.

Finally, the fourth chapter fabricates patterned p-VO_2 resistors on a 1 mm-wide and 2.5 µm-thick polyimide membrane. A biaxial strain of 0.3 % is induced in the p-VO_2. A continuous and exponential variation of the gauge factor is observed up to 4180 at 0.2 % of strain. This phenomenon is attributed to the intrinsic piezoresistive effect in VO_2 and grain dislocation. The chapter shows that the crystal is subjected to irreversible damage past 0.1 % of strain. These results set clear limits on the use of p-VO_2 as a high-strain sensor.

Acknowledgements

Je voudrais commencer ces remerciements en soulignant la chance que j'ai eue de pouvoir exercer ce métier de chercheur, au cours de ces quatre dernières années. Certes, le job n'est pas toujours des plus reposants, mais il offre, en mon sens, une opportunité unique de grandir en tant que personne, bien au-delà de ce que mes années d'études m'ont apporté. La raison principale derrière cela est l'importante liberté offerte par la thèse. Une liberté de gérer soi-même son travail, ses objectifs et ses collaborations, et surtout, de gérer son temps. Ces quatre dernières années furent une expérience extrêmement riche par ce qu'elle permet de réaliser, dans et en dehors de l'université.

À ce titre, je souhaite adresser mon premier remerciement au Professeur Jean-Pierre Raskin. Merci Jean-Pierre d'avoir cru en moi dès le début et de m'avoir donné la chance de découvrir ce monde. Merci également de prolonger cette confiance pour la suite de l'aventure qui nous attend. J'espère ne pas te décevoir. Je n'ai pas les mots pour décrire à quel point je te remercie pour cette opportunité. Une grande part de ce que j'ai pu accomplir ces dernières années te revient. Merci !

Mon second remerciement va naturellement au Professeur Denis Flandre qui a dû conjuguer avec ma personnalité parfois peu académique. Tu as toujours répondu présent quand j'ai eu besoin d'aide et, à ta manière bien à toi, as su me pousser dans mes retranchements à de très nombreuses reprises. Tu m'as fait confiance dès le début, en m'accompagnant avec une rigueur que j'admire.

Je souhaite également remercier tous les membres de mon jury pour leur temps, considération, et relecture approfondie de mes travaux. J'en profite également pour remercier toutes les personnes qui m'ont aidé pendant cette

thèse. J'entends par là l'ensemble du staff de Winfab, Welcome et tout le personnel administratif et technique. Une pensée particulière pour Benoît Hubert, Christian Renaux, Pascal Simon, Anne Gillet et Isabelle Dargent. Merci pour tous les rires partagés.

J'aimerais ensuite remercier deux chercheurs sans qui je ne serais pas la même personne aujourd'hui : Nicolas Roisin et Anne-Sophie Collin. Je ne sais pas quel miracle m'a fait croiser votre route, mais vous êtes les architectes du chercheur que je suis devenu. Au-delà de ça, vous êtes surtout deux amis exceptionnels en qui j'ai toute confiance. Merci de faire partie de ma vie. Une pensée aussi pour Karim El Khoury et Massinissa Nabet. Vous avez été deux exemples importants pendant ma thèse, et dès le début. Massi, je rejoins enfin l'équipe des grands !

Ces quatre années n'auraient cependant pas été les mêmes sans toi, Clémentine. Merci d'avoir été ma partenaire de galère, de thèse, de rédaction, et une amie pendant toute cette aventure. Le thé n'aura plus le même gout sans toi …

Une pensée également pour tous les membres du Bureauf et Sympathisants qui se reconnaîtront. Une pensée particulière aux vieux copains qui m'ont fait vivre tant de beaux moments pendant le début de ma thèse : Antoine Enel, Noémie Bidoul, Jérémy Trips, Alex Pip et Roselien Vercauteren.

Merci également à Ottilie Bonfanti. Merci d'être the best pal et de m'avoir fait vivre tant de fous rires. You da best !

Enfin, pour le volet UCLouvain, impossible pour moi de ne pas mentionner mon compagnon de douleur et de bataille. Capitaine d'un bateau en pleine tempête : Augustin Wattiez ! Nous y sommes, mon ami ! 2531 est derrière nous !

Comme mentionné dans le début de ces remerciements, la richesse d'une thèse se trouve également dans ce qu'elle permet de faire autour. Je tiens donc à remercier du fond du cœur mes partenaires de La Ruve : Antoine Passau, Lola Cornet et Céline Delforge. Nous sommes au début d'une belle histoire, que j'ai hâte d'écrire avec vous !

Une pensée toute particulière pour Céline, qui partage ma vie pour, je l'espère, de nombreuses années. Aucun projet, aussi fou soit-il, ne me paraît impossible avec toi à mes côtés. On n'aura peut-être pas eu notre gare, mais la suite ne peut être que meilleure. Comme on dit : "En roooouute !"

Un mot spécial va bien entendu à Thomas Tasiaux. Merci de me suivre depuis si longtemps. Merci pour ces très nombreuses années passées ensemble. Tu m'as fait grandir sur tellement d'aspects, et m'offres une perspective sur le monde que je ne saurais développer sans toi. Merci d'être mon ami, dans les bons et les mauvais moments, au quotidien, depuis si longtemps.

Avant d'en arriver au mot de la fin, je souhaite remercier du fond du cœur mes parents, pour m'avoir permis d'aller jusque-là ! En arriver à la personne que je suis est le fruit de votre travail, de votre confiance et de votre soutien. Je remercie également Nicolas Lahaye pour ses nombreuses relectures.

Enfin, j'aimerais terminer ces remerciements en disant : Rond comme un ballon. Rapide comme un avion. C'est Brieuc.

Merci à tous.

Contents

List of Figures . . . . . **ix**

List of Tables . . . . . **xi**

Acronyms and notations . . . . . **xiii**

Introduction **1**

1 Thin polyimide membrane as a platform for high-strain studies **13**
1.1 Design 15
1.2 Process 16
1.3 Bulge test setup 21
1.4 Deflection measurement 23
1.5 Conclusion 27
1.6 Take home messages 28

2 Modeling and validation of the straining platform with c-Si demonstrators **29**
2.1 Membrane modeling 31
Model fitting 32
Experiment modeling 35
2.2 Deflection results 36
2.3 Strain results 39
2.4 Raman validation: theory 40
2.5 Raman validation: results 42
2.6 Conclusion 44
2.7 Take home messages 45

3 p-VO_2 integration on a thin-polyimide membrane **47**
3.1 VO_2 synthesis 49

Sputtering 51
Annealing 55
3.2 p-VO_2 blanket on polyimide membrane 61
Motivation 61
Process 62
Young's modulus recovery 65
3.3 Conclusion 69
3.4 Take home messages 69

4 p-VO_2 resistors: Impact of high-strain on the gauge factor . . 71
4.1 p-VO_2 resistors on PI membrane 73
Design 73
Process 74
4.2 Experimental setup 78
4.3 Deflection Results 80
4.4 Strain Results 83
Slippage assessment 85
4.5 Resistance and Gauge Factor 87
4.6 Conclusion 91
4.7 Take home messages 92

Conclusions and perspectives 94

Author's publication list 109

Bibliography 111

List of Figures

1 Thesis outline 12

1.1 Design schematics: Layout of a 1 × 1 cm^2 die with a 2.5 mm-diameter circular polyimide membrane carrying c-Si devices . . 15
1.2 Process flow schematics: Summary of the fabrication process used to integrate silicon resistors on a large, free-standing, polyimide membrane 17
1.3 Polyimide precursor patterning 19
1.4 Fabrication results 21
1.5 Instrumentation setup to measure p-VO_2 resistors on a polyimide membrane under pressure 22
1.6 White light interferometer 23
1.7 Polytec measurement 25
1.8 Maximal deflection vs pressure 26

2.1 Fitting of the stack layers 33
2.2 Fitting of the stack yield stress 34
2.3 Fitting of the stack hardening exponent 35
2.4 Model of the 2.7 mm-wide and 3.6 µm-thick polyimide membrane 37
2.5 Deflection measurement of a 3.6 µm-thick 2.7 mm-diameter circular polyimide membrane 38
2.6 Strain field simulation: Strain field inside a 0.3 µm-thick c-Si device on a 3.6 µm-thick 2.7 mm-diameter polyimide membrane under increasing pressure 39
2.7 Raman silicon peak shift: Raman peak shift measured into a 0.3 µm-thick c-Si resistor on a 3.6 µm-thick 2.7 mm-diameter polyimide membrane under increasing pressure levels 43

3.1 Reactive sputtering setup 50
3.2 VO_2 reactive sputtering calibration curve 53

3.3 Grain size as a function of the annealing temperature 56
3.4 Grain size as a function of the amount of oxygen 58
3.5 Raman spectrum of V_xO_y compounds as a function of the amount of oxygen 59
3.6 Resistance vs temperature 61
3.7 Integration of VO_2 thin film on a polyimide membrane 63
3.8 Young's Modulus of VO_2 68

4.1 Design Schematics: Layout showing a 3 x 3 mm^2 die featuring a 1 x 1 mm^2 square shaped membrane and a set of four electrically contacted p-VO_2 2T devices 73
4.2 Process flow schematics: Summary of the fabrication process to integrate p-VO_2 resistors on a free standing, 1-mm wide, polyimide membrane. 76
4.3 Process results: Microscopic image of a 1 mm-wide, 2.5 µm-thick polyimide membrane carrying a set of four p-VO_2 resistors alongside its edges 78
4.4 Model of the 2.7 mm-wide and 3.6 µm-thick polyimide membrane 80
4.5 Displacement results of a 1 mm-wide, 2.5 µm-thick polyimide membrane under pressure 82
4.6 Strain simulation results: Biaxial strain in a p-VO_2 resistor placed alongside the edge of a 1 mm-wide and 2.5 µm-thick polyimide membrane. Each panel provides the strain for its corresponding pressure cycle. The strain induced during the up and down sweeps of the pressure cycle is shown by a light blue line with squares and a dark blue line with dots. The red crosses (x) and plus (+) indicate matching data points between pressure cycles. The inset of the first cycle illustrates the origin of the biaxial strain. 84
4.7 Picture of the 1 mm-wide and 2.5 µm-thick polyimide membrane used in the experiment after being pressurised to 100 kPa. The pictures are taken with various microscope filters and at different locations to highlight the lack of delamination at the membrane's edge. 86
4.8 Electrical measurements: IV measurements of p-VO_2 resistors under increasing tensile strain 88
4.9 Gauge factor of p-VO_2 and c-VO_2 devices under strain 90

List of Tables

1 Summary of multifunctional strain sensors 6

3.1 Young's modulus of different types of VO_2 available in the literature. 65

Acronyms and notations

Microfabrication and processing

ALD	Atomic Layer Deposition
CVD	Chemical Vapour Deposition
DRIE	Deep Reactive Ion Etching
ICP	Inductively Coupled Plasma
MEMS	Micro Electromechanical Systems
PAD	Polymer Assisted Deposition
PECVD	Plasma Enhanced Chemical Vapour Deposition
PEB	Post Exposure Bake
PLD	Pulsed Laser Deposition
RIE	Reactive Ion Etching
RTA	Rapid Thermal Annealing

Materials and Compounds

a-	Amorphous (e.g. a-VO_2)
c-	Crystalline (e.g. c-VO_2)
p-	Polycrystalline (e.g. p-VO_2)
Al	Aluminium
Au	Gold
BHF	Buffered Hydrofluoric Acid
Cr	Chromium
KOH	Potassium Hydroxide
M1	Monoclinic 1 Crystallographic Configuration
M2	Monoclinic 2 Crystallographic Configuration
PDMS	Polydimethylsiloxane
PGMEA	Propylene Glycol Methyl Ether Acetate
PI	Polyimide
R	Rutile Crystallographic Configuration
SF_6	Sulfur Hexafluoride

Si	Silicon
SiO_2	Silicon Dioxide
TMAH	Tetramethylammonium Hydroxide
V	Vanadium
VO_2	Vanadium Dioxide

Notations

E	Young's Modulus [GPa]
ϵ	Strain [-]
$\epsilon_{0,\mathrm{eff}}$	Effective *Swift* Reference Strain [-]
$\hbar$	Reduced Planck's constant [J.s]
λ	Raman Wavelength [nm]
n_{eff}	Effective *Swift* Hardening Exponent [-]
PDP	Phonon Deformation Potential
p, q, r	Phonon Deformation Potential Coefficients
σ	Stress [MPa]
$\sigma_{y,\mathrm{eff}}$	Effective *Swift* Yield Stress [MPa]
ν	Poisson's ratio [-]
ω	Raman Wavenumber [cm^{-1}]

Others

FEM	Finite Element Method
GF	Gauge Factor
SEM	Scanning Electron Microscope
TEM	Transmission Electron Microscope
XRD	X-Ray Diffraction

Introduction

Context

Strain engineering is an ever growing scientific enquiry [1, 2]. Over the years, the development of strain sensors started to shift from conventional strain gauges to the design of novel, multifunctional, flexible sensors that allow to measure wide range of strain while responding to other physical stimuli such as temperature [3, 4, 5, 6]. This shift started with the demand for strain sensing in applications such as smart flexible sensors [7, 8, 9], intelligent packaging [10, 6] and, in particular, human body monitoring [11, 12, 13, 14, 15, 16].

Human body monitoring gained major traction with the progress in machine learning and signal processing that facilitates the interpretation and decoupling of effects from multifunctional sensors [17, 18, 19, 20, 21, 22]. This traction is motivated by the wide range of applications such as e-skins [20, 23, 24], soft robotics [25, 26, 27, 28, 29], full body motion tracking (macrostrain) [30, 31, 32, 33] or cardiovascular disease prevention (microstrain) [34, 35, 36, 37, 38, 39].

Conventional strain sensors can be classified into three different categories: capacitive, piezoelectric and piezoresistive devices [40, 41, 42]. Among the three, the most promising in terms of sensitivity and miniaturisation are the piezoelectric and piezoresistive based devices [1]. Capacitive sensing benefits from simple processing techniques [43, 44, 45] but is, by nature, difficult to miniaturize [42, 46]. This renders them unsuitable for applications such as blood flow monitoring or internal implants. In addition, they suffer from parasitic capacitance and their read-out circuitry is generally complex due to the small changes of capacitance with strain [1, 42].

Piezoelectricity and piezoresistivity have been in direct opposition since the 1980s and each has their own advantages [1]. On one hand, piezoelectric devices rely on the generation of electrical charges upon deformation. Their primary advantage is that the sensor itself does not require a power source since the charge generation is an intrinsic material property [42, 1]. However, they only allow the measurement of high and dynamic strain [42, 40].

On the other hand, piezoresistivity relies on the change of resistance of a deformed material. This means that the sensors are not self-powered. However, their fabrication, like piezoelectric devices, only depends on the integration of one active material. Furthermore, they allow the measurement of static, dynamic and subtle deformations [42, 40]. Finally, they offer the possibility for simple read-out circuitry as the transduction is done via a measurement of the variation of resistance of the device [1, 40, 47, 48]. These advantages make piezoresistive devices good candidates to integrate on flexible substrates for health monitoring.

Table 1 presents some promising candidates for multimodal sensing available in the literature. The table is not meant to be exhaustive as the literature on multimodal sensing is broad but aims at depicting a picture of the dominant trends. The table is inspired from [49, 50] and expanded to include silicon, vanadium dioxide and other materials. More specifically, it presents materials or sensors that demonstrated multimodal sensing capabilities while integrated on a thin flexible substrate. This is why material such as bulk silicon is not presented despite its well known high gauge factor of up to 200 [51, 52, 53].

Looking into it, the dominant research directions are toward the development of sensors relying on 2D materials (MXene, TMDs) [50] and conductive polymers [54, 55, 56, 57, 58, 59, 60] which include composites such as CNT [61, 62, 63, 64, 65, 66] and semiconducting polymers [11, 67, 68, 69, 70].

However, those materials are hard to fabricate at the microscale for implants [71, 72], prone to sensitivity degradation [73, 74, 75], offer poor output signal quality [76, 77] and are incompatible with most conventional microfabrication techniques [78, 79, 80]. However, they remain promising as most of them can be rendered multifunctional, as presented in the table [81, 82].

To cope with those limitations, flexible MEMS strain sensors based on conventional inorganic materials are investigated [71]. Silicon has been extensively studied as it is well known to be able to react to strain [51], temperature [83] and light [84]. Silicon based diodes have been widely used as temperature sensors [83] and c-Si resistors are commonly used in pressure sensors [85] with recent work reporting pressure sensors built from SOI wafers with a sensitivity of up to 0.461 μV/V/Pa [86], underlying the potential of the material. Looking into the use of silicon as coupled strain and temperature sensor, most work rely on the integration of multiple silicon based sensors, each designed for one specific stimulus, onto a single die [87, 88]. While effective, this approach increases process complexity and is at the cost of device density [87]. Recently, [87] proposed to solve this limitation by directly exploiting the intrinsic response of c-Si to strain and temperature. They manage to obtain a multimodal sensor, presented in Table 1, based on a single 200 nm-thick c-Si serpentine fabricated from an SOI wafer and transfered to a final PI substrate. While successful, their approach relies on a non-monolithic fabrication process while featuring limited sensing performances, as presented in Table 1.

In a nutshell, researchers have been looking for a single inorganic material that can be fabricated on flexible MEMS with standard microfabrication techniques while featuring a high gauge factor and sensitivity to temperature for multifunctional implantable sensors [89, 87]. In this regard, Vanadium Dioxide stands out as a particularly promising candidate as it intrinsically offers a high sensitivity to multiple stimulation like magnetic, optical, electrical, thermal and mechanical [90]. Table 1 presents a dual strain-temperature flexible sensor based only on pre-transition measurements [89]. However, what sets vanadium dioxide apart is its ability to encode physical stimulations into spikes by exploiting the insulator to metal phase change of the material [91, 92, 93, 94, 95, 96]. Encoding of the stimulation into spikes bears the potential of substantial boost in sensitivity and decrease in sensory power consumption as reported by [97] which reports the fabrication of a temperature sensor with an intrinsic sensitivity of up to -2.19%/°C and an spike encoded sensitivity of up to 5.5%/°C. Those consideration sets VO_2 as a prime candidate for integration into flexible, multimodal sensors which is discussed in the remainder of this chapter.

Stimulus	Transduction mode	KPI	Response range	Processing	Refs.
MXene					
$Ti_3C_2T_x$	Pressure	Resistive	-1.89% kPa^{-1}	0-100 kPa	Inkjet printing	[98]
	Temperature		-0.22% $°C^{-1}$	25-50°C		
$Ti_3C_2T_x$	Strain	Triboelectric	-	0-400%	Brush Coating	[99]
	Pressure		2.35 V/kPa	0.3-1.0 kPa		
$Ti_3C_2T_x$	Pressure	Resistive	1878.05 kPa^{-1}	8-125 kPa	Drop Coating	[100]
	Humidity		0.67% $(\%RH)^{-1}$	11.5-98.1 % RH		
TMDs[1]					
InSe	NO_2	Resistive	51.7% ppm^{-1}	100 ppb - 2ppm	Drop Casting	[101]
	Temperature		-0.45% $°C^{-1}$	25-150°C		
InSe	Optical	-	$\Delta E_g^{max} = -26$ mEv @ 0.13 % ϵ_{biax}	-		[102]
	Strain	-	450-100 Gauge Factor	0-0.48% ϵ_{biax}		
Bi_2Te_3	Pressure	Resistive	120 Pa^{-1}	0-30 kPa	3D structure	[103]
	Temperature	Thermoelectric	-426.4 μVK^{-1}	ΔT : 0.1-85 K		
Graphene					
Graphene	Strain	Resistive	2203.5 Gauge Factor	0-6.8%	LDW + transfer	[104]
	Pressure		678.2 kPa^{-1}	0-500 kPa		
G:GO:rGO[2]	Pressure (G)	Capacitive	0.0175-0.0025 pF kPa^{-1}	0-400 kPa	CVD + lamination	[105]
	Thermal (rGO)	Resistive	-0.0035 $M\Omega K^{-1}$	0-100°C		
	Humidity (GO)	Capacitive	0.005- 0.14 pF $(\%RH)^{-1}$	20-90% RH		

(Continues)

	Stimulus	Transduction mode	KPI	Response range	Processing	Refs.
Heterojunction						
TiO_2/WS_2	Pressure	Resistive	12.07% N^{-1}	-	Screen printing	[106]
	Temperature	Resistive	0.22%°C^{-1}	25-50°C		
	Light	Photoelectric	75 mA/W	0.024-1.68 mW/cm^2		
	NO_2	Resistive	3.6 ppm^{-1}	0.2-2 ppm		
Metal						
Te NWs [3]	Strain	Piezoelectric	0.454 V	0.044-0.308 %	Thermal evaporation	[50]
	Temperature	thermoelectric	225.1 μV K^{-1}	ΔT : 0.1-6.3 K		
Polymers and Composites						
SPMF [4]	Pressure	Resistive	10.8% kPa^{-1}	0-100 kPa	Impregnation + ultrasonic mixing	[107]
	Temperature	Thermoelectric	38.2 μV K^{-1}	ΔT : 0-40 K		
PVA hydrogel	Pressure	Piezoionic	1.6 mV K^{-1}	60 Pa - 2 MPa	Mold forming	[108]
	Temperature	Thermoelectric	1.94 kPa^{-1}	30-42°C		
CNT [5]	Force	Resistive	1510 kPa^{-1}	2.5-255.7 kPa	Electrospinning	[109]
	Temperature		-	40-110 °C		
$BMIMBF_4$ (Ionogel)	Force	Resistive	-	1-700%	photopolymerization	[110]
	Temperature		-	-40-300°C		

(Continues)

	Stimulus	Transduction mode	KPI	Response range	Processing	Refs.
Silicon						
c-Si/SOI	Strain	Resistive	GF: -13.88 $\epsilon < 0$ GF: 11.72 $\epsilon > 0$	0-0.4%	Transfer printing	[87]
	Temperature	Resistive	0.23% °C^{-1}	29-53°C		
VO_2						
p-VO_2	Strain	Resistive	GF: 400	0-0.1%	PAD	[89]
	Temperature		1.12×10^{-2}K^{-1}	270-320 K		

Table 1 Summary of multifunctional strain sensors

Vanadium Dioxide as a multifunctional sensor

Vanadium dioxide (VO_2) is praised for its many outstanding characteristics. At the heart of them all lies the ability of the VO_2 crystal to transition between different crystallographic arrangements with different physical properties [90, 111]. In addition to the well documented full transition of the VO_2 crystal from a high-resistivity monoclinic (M1) state to a low-resistivity rutile (R) one [112, 113, 114], the material is known for its high sensitivity to different external stimuli. This includes magnetic, optical, electrical, thermal and mechanical, making VO_2 a true inorganic multifunctional material [90].

Looking into the mechanical stimulation, when strained, the M1 crystal partially transitions to an intermediate M2 configuration [113, 114, 115, 116, 117, 118, 119, 120]. This partial reconfiguration is accompanied by an increase of resistance coming from the intrinsic difference in resistivity of both phases ($\rho_{M2} = 3 * \rho_{M1}$) [116, 117]. This leads to intrinsically high and strain dependent gauge factors (GF). Previous work report GFs varying from 175 to 150 for c-VO_2 nanobeams [117] and from 620 to 370 for epitaxial layers [121] subjected to 0.3 % of tensile strain. Such values far surpass the ones of metallic gauges (up to 2) or silicon (up to 200) [53].

In order to study or exploit the properties of strained VO_2, an appropriate strain platform must be developed. A popular choice for strain induction is to rely on the mismatch between two material's thermal expansion coefficient generating stress during the fabrication process [122, 123]. This approach led to the development of MEMS-based techniques allowing strain studies to be carried out up to the mechanical limits of the material [124, 125]. However, those techniques do not provide a dynamical control of the induced strain. Different devices, tailored to reach various strains, must be fabricated to cover a large range of deformation with sufficient step resolution [124, 125]. This leads to process and design complications as well as device-to-device variation in the measurement.

[1]TMDs: Transition metal dichalcogenide monolayers.
[2]G:GO:rGO: Graphene: Graphene Oxide: reduced Graphene Oxide. The KPI values were computed from the plots in the paper but not given as is.
[3]NW: nano wire.
[4]SPMF: SWCNT and PEDOT:PSS decorated porous MF
[5]Carbon nano tube

Another approach is to actively induce strain in a material or device via an external actuation mechanism. One technique is to rely on a bulge or blister test using a micro-fabricated membrane subject to increasing pressure. One way to do so is to use a thin, stress compensated, oxide based, membrane carrying the device or material of interest. While this approach has been extensively studied, as reported in [126, 85], it is generally used for pressure sensing rather than for inducing high-strain. Indeed, those membranes are prone to breaking and typically allow to reach strain of up to 0.04 % as in [127]. Other fabrication processes, like Silicon-on-Nothing (SON), can be used to build the membrane but they face similar challenges while only reaching 0.036 % of strain [128].

A promising path to reach higher deformation is to build the membrane out of polymer. Their lower Young's modulus allow for more bulging and deformation of the membrane before fracture, which enables to induce a higher strain in the device or material of interest. A first example comes from [129] which integrates a 2D-layer of MoS_2 onto PDMS and reaches between 2 and 3 % of strain during the blister test. Another one, from [130], reports the integration of 10 nm-thick silicon resistors on a polyimide (PI) membrane. They demonstrate the induction of 3.5 % of strain in the silicon resistors [130].

This approach is of particular interest for vanadium dioxide for which a recent trend has been its integration on polymeric flexible substrates for high-strain sensing [117, 89, 121, 131, 132]. While the use of PDMS or polyimide allows to reach high-strain in the studied material, the practice comes with some drawbacks. The first one is bound to the use of soft plastics that exhibit poor resistance to heat or strong chemicals [133]. This renders them incompatible with conventional processing techniques. The integration of electronic devices or materials must be done via either a direct low-temperature deposition, like in [133], or complex transfer and subsequent alignment of layers, like in [130]. Other examples of flexible electronic processing, that illustrate their complex nature, are well described in literature, including [134, 135, 136, 137].

These processing limitations are particularly problematic for VO_2 since they limit the use of well-established, cleanroom compatible, techniques such as sputtering [138].

Direct low-temperature deposition [139, 140, 141, 142, 131, 143, 144] can be used but produces VO_2 layers of poor quality due low crystallinity [145, 146, 140]. Another approach is to use layer transfer [146, 89] to integrate high-quality [145, 147] thermally-annealed p-VO_2 deposited by sputtering [148] or PLD [149] but it is notoriously complex and hard to scale [146, 89]. Monolithic direct integration of sputtered p-VO_2 layers onto flexible substrate is of interest but remains out of reach due to the limited thermal budget of polymers [150, 150, 151] and the high-temperature annealing required to reach the desired level of VO_2 crystallinity [152, 153, 154]. Up-to-now, no such demonstration has been carried out.

A further issue is the lack of fundamental understanding of the mechanics governing the behavior of polymer based membranes. While conventional MEMS membranes benefit from a rich literature allowing to predict both the behavior of the membrane and the strain induction in the device under test [155, 156, 157, 158, 159], this is not the case for complex polymeric stacks. Furthermore, the strain field in the active material layer is often simplified and treated as uniaxial or symmetrically biaxial, like in [130], without formal validation which is detrimental in experiments requiring precise knowledge of the strain field components.

In this work, we propose to study the piezoresistive properties of highly strained p-VO_2 fabricated by sputtering. More specifically, the thesis proposes to characterise the evolution of the gauge factor of sputtered p-VO_2 under high-strain as a first step toward its use in multifunctional sensors. It tries to answer the following scientific question:

Can thermally annealed sputtered p-VO_2, integrated on a flexible substrate, be used for high-strain multifunctional sensing applications?

To answer it, the question is decomposed in four smaller scientific contributions. Each one of them is addressed in a dedicated chapter. The outline of the thesis is explained here below while its structure and main storyline is illustrated in Fig. 1.

Chapter 1

The first chapter of this thesis details a processing technique that allows the monolithic integration of microelectronics on polyimide without process limitation or thermal budget. A demonstration of the process is made by fabricating c-Si resistors on a 2.7 mm-wide and 3.6 µm-thick polyimide membrane. The focus of the chapter is on the following scientific question:

How to integrate c-Si devices, in a monolithic way and without process limitation, on a thin polyimide membrane?

In addition, this first chapter introduces a compact *bulge test* setup to measure the membrane under pressure. This experimental setup allows the *in situ* measurement of the membrane and devices using a white-light interferometer or a Raman spectrometer while leaving enough space for electrical probing of the devices.

Finally, an initial measurement of the membrane maximal deflection under load is presented along with the required data processing.

Chapter 2

A *Comsol Multiphysics* finite element method (FEM) model of the membrane is presented. This model is built to predict the maximal deflection of the membrane with pressure in both an elastic and a plastic deformation regime. The first chapter identified that the membrane enters in a plastic deformation mode past a given pressure point. The *Swift* plastic deformation model is used in *Comsol* to consider this phenomenon. The model is presented along with its fitting parameters.

The chapter details how fitting the *Comsol* model on an *in situ* maximal deflection measurement of the membrane allows to correctly compute the local strain tensor inside of the c-Si device. A Raman spectroscopy experiment is introduced to validate the computed strain field. The variation of the Raman peak shift in the c-Si devices is computed based on the strain tensor obtained with *Comsol* and compared to experimental data.

The first goal of this chapter is to prove that the local strain field in a device fabricated on a polyimide membrane can be computed using a fitted *Comsol* model.

This is of primary importance to allow the use of the fabricated membranes for strain studies. The second one is to challenge the absolute maximal strain level induced in the device by the membrane. This test allows to determine whether or not the proposed polyimide membrane is suited for high-strain studies.

In short, the scientific question under consideration is:

Can a Comsol simulation model the plastic deformation of a polyimide membrane to compute the local strain field induced in the carried c-Si devices and how much strain can be induced in the c-Si resistors?

Chapter 3

The monolithic fabrication process is used to integrate thermally annealed sputtered p-VO_2 on a 2.5 mm-wide and 3.2 µm-thick polyimide membrane. The synthesis and deposition protocols are presented along with the characterization tools required to assess the quality of the fabricated p-VO_2.

The first objective of this chapter is to check the process feasibility and the proper adhesion between the polyimide and the p-VO_2. To do so, the deposited layer of p-VO_2 is left unpatterned. This allows the realisation of a pull test to demonstrate the adhesion of the two layers.

The as-fabricated membrane, with its blanket layer of p-VO_2, is next used to recover the Young's modulus of the p-VO_2 via a bulge measurement and a fitting of the *Comsol* model. Recovering the Young's modulus of the material is paramount for proper computation of the strain in p-VO_2 devices fabricated on a PI membrane.

The goal of this chapter is to prepare the ground for the integration of patterned p-VO_2 devices on PI membranes in the next chapter. It answers this scientific question:

How to integrate thermally annealed p-VO_2 on a thin, released, polyimide membrane to recover its Young's modulus?

Chapter 4

Finally, the impact of high-strain on the gauge factor of p-VO_2 is tackled. Thermally annealed, sputtered and patterned p-VO_2 resistors are fabricated with a monolithic process on a 1 mm-wide and 2.5 µm-thick polyimide membrane.

The membrane is mounted on the *bulge test* setup and the variation of the electrical resistance of the p-VO_2 resistors with pressure is measured. An *in situ* measurement of the maximal deflection at each pressure step is made.

The *Comsol* model is fitted on the experimental data to obtain the local strain inside of the resistors which allows the computation of the gauge factor as a function of the applied strain.

This last chapter answers the last question of this work:

How does the gauge factor of patterned p-VO_2 fabricated via reactive sputtering and thermal annealing behave under high-strain?

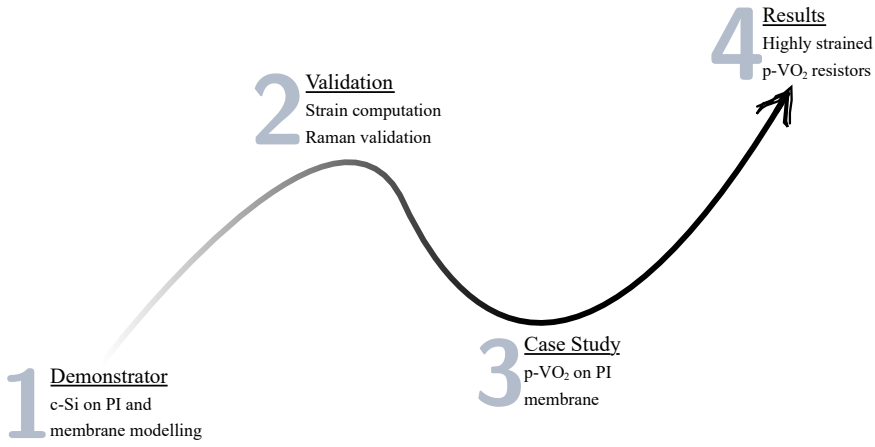


Fig. 1 Outline of the thesis. The first chapter details the monolithic integration of c-Si resistors on a polyimide membrane. The second one models the strain induced in the devices upon bulging. The third chapter investigates the integration of p-VO_2 on polyimide while the last one studies the gauge factor of highly strained p-VO_2 resistors.

1

Thin polyimide membrane as a platform for high-strain studies

The goal of this thesis is to evaluate the properties of highly strained sputtered polycrystalline vanadium dioxide devices using a polyimide based membrane. p-VO_2 deposited by sputtering requires high-temperature thermal annealing to go from amorphous to polycrystalline [148, 152, 153, 154]. This renders the use of low temperature monolithic fabrication processes on flexible substrates from the literature impossible [145]. The alternative is to use a layer transfer method but those are challenging to develop and hard to scale [146].

This chapter proposes to solve those limitations by integrating the material of interest onto the flexible substrate during a post process step. Polyimide is spin coated as the last layer in the process which makes it monolithic, wafer scale and without thermal budget. A demonstration of the feasibility of the process is done by designing and integrating single crystalline (c-Si) resistors on a 3.6 µm-thick and 2.7 mm-diameter polyimide MEMS membrane.

The behavior of the as-fabricated membrane is studied by assembling a *bulge-test* setup to measure the deflection of the membrane under a white light interferometer.

The decision to demonstrate the process with c-Si and not p-VO_2 comes from two reasons:

- **Ease of processing:** The demonstration process starts from a silicon-on-insulator (SOI) wafer. The focus is on process design and polyimide handling instead of on processing of the active material.
- **Known material properties:** c-Si is a well known material. All of its mechanical properties are available in literature as-opposed to p-VO_2 for which information like the Young's modulus are hard to find [160, 161, 162]. Furthermore, c-Si has a well studied Raman response to strain [163, 164]. This allows to validate the strain field computed by a *Comsol* model [165]. This is the topic of the next chapter.

In a nutshell, this chapter tries to answer the following scientific question:

How to integrate c-Si devices, in a monolithic way and without process limitation, on a thin polyimide membrane?

To answer that question, this chapter presents:

- **A monolithic fabrication process** of microelectronics on a flexible substrate without process limitation related to the thermal budget of polyimide. A complete fabrication scheme is presented and 2.7 mm-wide and 3.6 µm-thick polyimide membranes with c-Si resistors are fabricated.
- **A bulge-test setup** used to inflate the polyimide membrane under a white light interferometer or a Raman spectrometer with access for probes to electrically characterise the device under test.
- **A deflection measurement** of the bulged membrane. The membrane is inflated at increasing pressure level and measured by white light interferometry. This is done to obtain an experimental pressure-maximal deflection profile. The data processing to go from the raw measurements to the maximal deflection curve is presented.

1.1 Design

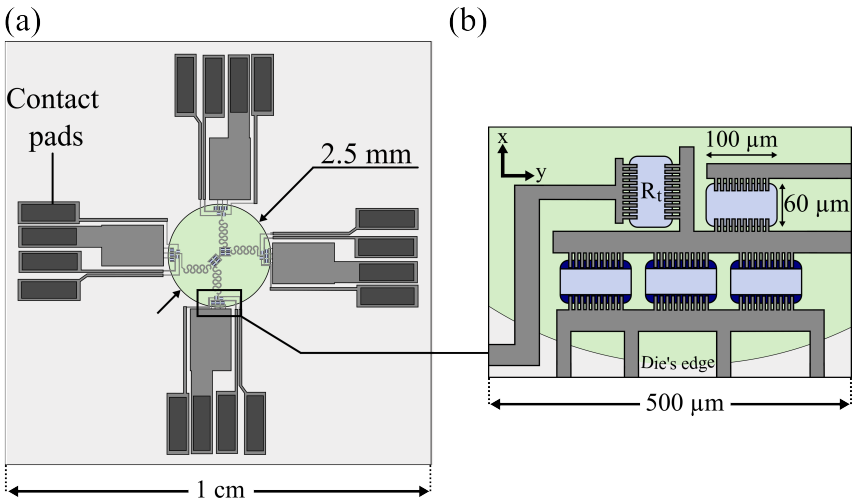


Fig. 1.1 Design schematics: (a) Layout showing a 1x1 cm^2 die featuring a 2.5 mm-diameter circular membrane. (b) Zoom on a subset of devices located on the membrane edge. R_t stands for transversal resistor regarding the orientation of its electrical connections relative to ε_{xx} in local coordinate. The x and y axes are shown as black arrows. The aluminium lines are in gray, the pad openings in dark gray, the membrane in green and the die in light blue. NPN devices and other resistors are visible on the layout but out of the scope of this work.

Figure 1.1(a) represents the layout of a die carrying a 2.5 mm-diameter circular membrane. The circular shape of the membrane was selected to make the process compatible with either an XeF_2 isotropic or a Bosch anisotropic release. Each die features four sets of two c-Si p-type resistors and four NPN junctions positioned alongside the membrane's perimeter to maximise the amount of induced strain [85, 166]. All devices share the same 60 µm by 100 µm dimensions as visible in Fig. 1.1(b). Electrical connections are made by 1 µm-wide aluminium fingers and 20 µm-wide aluminium traces that extend from the die onto the released membrane. 500 µm by 1500 µm contact pads are visible in dark gray on the figure. The study carried out in this work is performed on R_t which stands for transversal resistor.

It is defined by the current flowing perpendicularly to the direction of the ε_{xx} strain component in local coordinate. All other structures visible on the layout are out of the scope of this work.

1.2 Process

The integration of p-type silicon resistors on a thin polyimide membrane is illustrated in Fig. 1.2. The process starts in Fig. 1.2(a) with a silicon-on-insulator (SOI) wafer from *SOITEC* featuring a top 300 nm-thick (100) oriented c-Si layer, a buried oxide (BOX) of 1050 nm and a bulk c-Si substrate of 725 µm.

To define the resistors, 60 µm by 100 µm silicon mesas are patterned in Fig. 1.2(b) by photolithography and anisotropic CHF_3 inductively coupled plasma reactive ion etching (ICP-RIE from *Corial*). The top silicon layer is thermally oxidised as a preparation step for ion implantation resulting in a 27 nm-thick silicon dioxide layer. A boron implantation step is performed to obtain p-type resistors. The implantation was performed by *Ion Beam Service (IBS)* with a requested dose of 4.2×10^{13} atoms/cm^2 at an energy of 10 keV. Doping atoms are then activated by a 30-minutes-long annealing at 850°C to complete the implantation phase. The final boron atom concentration in the silicon is estimated using a *Silvaco Athena* simulation to reach a maximal value of 3.5×10^{18} cm^{-3}. A 180 nm-thick silicon dioxide layer is then deposited by plasma-enhanced chemical vapour deposition (PECVD by *Oxford Instruments*) to passivate the doped silicon resistors after stripping of the top 27 nm-thick thermal oxide used for the implantation process.

Figure 1.2(c) deals with the electrical contacts definition. Access to the silicon mesas are first opened in the top silicon dioxide layer by a photolithographic step and a buffered HF (HF + NH_4F in a 1:7 ratio) isotropic wet etch. The electrical connections are built by sputtering (sputterer from *VST)* a 600 nm layer of Al/Si (99 % aluminium and 1 % silicon) and defined by photolithography and ICP-RIE BCL_3 anisotropic dry etch. A 432°C thermal annealing under a flow of forming gas is finally performed to obtain an ohmic contact between the p-doped silicon and the aluminium.

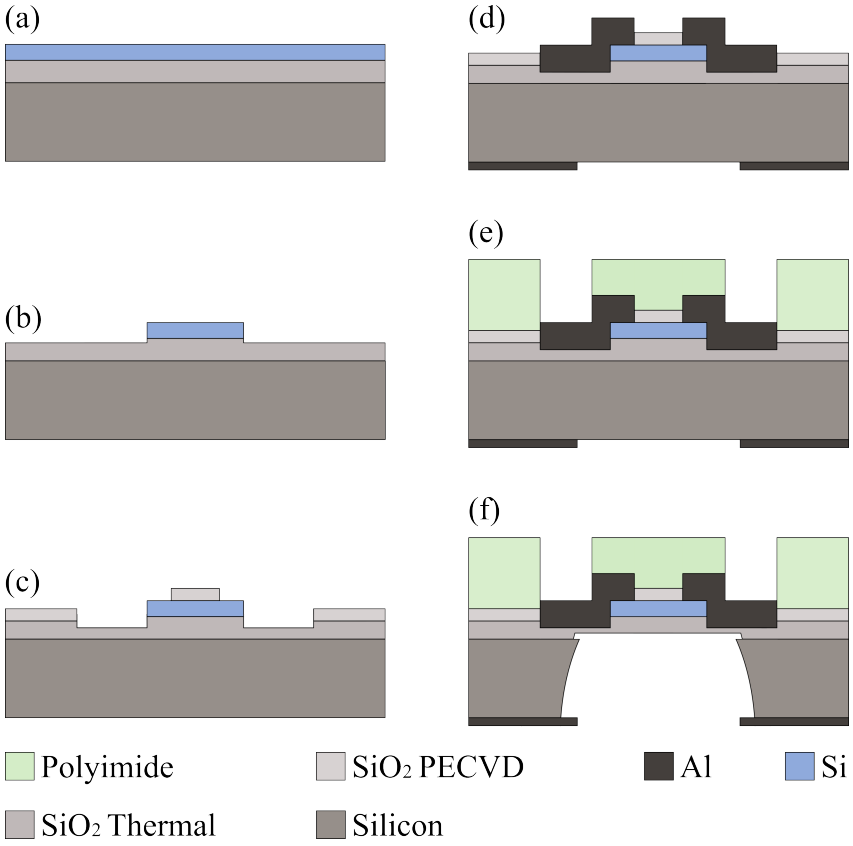


Fig. 1.2 Process flow schematics: Summary of the fabrication process used to integrate silicon resistors on a large, free-standing, polyimide membrane. (a) Initial (100) SOI wafer with a top 300 nm c-Si layer, 1050 nm buried oxide (BOX) and c-Si substrate. (b) ICP-RIE patterning, doping and passivation with 180 nm of PECVD silicon dioxide of the top silicon to pattern 60 µm by 100 µm p-type c-Si mesas. (c) Electrical contacts deposition by sputtering a 600 nm-thick Al/Si layer, patterned with dry etching. (d) Back grinding of the c-Si substrate and definition of a 300 nm-thick aluminium mask. (e) Spin coating of a 3.6 µm-thick polyimide layer and contact pads opening by indirect photolithography. (f) Release of the polyimide membrane by an isotropic XeF_2 dry etch of the c-Si substrate and isotropic BHF wet etch of the BOX.

Figure 1.2(d) summarizes the preparation required for the release of the membrane. The wafer is back-grinded from 725 µm to 280 µm in order to reduce the time needed to release the membrane. A 300 nm-thick aluminium mask is deposited by thermal evaporation (evaporator from *VST*) and patterned by photolithography and H_3PO_4/IPA isotropic wet etch on the back side of the wafer to define the membrane geometries.

Polyimide is chosen as flexible substrate, as in [130, 167]. Its integration as the last layer is done by spin coating a PI precursor, PI2545 [168] from *HDMicroSystem*, as shown in Fig. 1.2(e). The process detailed hereafter is adapted from [168]

Prior to the application of PI2545, the wafer is cleaned by an acetone, methanol and deionised water (DI) rinse before being dried overnight at 120°C, under an argon flow. An adhesion promoter, VM652 [169], is applied to the wafer in a puddle for twenty seconds before spinning the wafer dry at 4000 RPM for one minute. The VM652 is then activated by baking the sample on a hot plate for one minute at 120°C.

The polyimide precursor is dispensed onto the wafer and spin coated. Due to the honey-like viscosity of the precursor, a slow initial spin coating of 500 RPM for five seconds is done to spread the layer before spin coating at the nominal speed to get the desired precursor thickness. A final rotation speed of 1500 RPM maintained for one minute is used. The precursor is next soft baked on a hot plate at 140°C for six minutes to drive out excessive solvent.

PI2545 is not a photosensitive resist [168]. This means that a conventional photolithography cannot be used to develop and pattern the layer of polyimide. However, the uncured precursor is easily etched by TMAH based solvent, such as a conventional photolithography developer like MIF726 [170]. An indirect photolithography is performed by a doing a transfer of the pattern during the development of a classical, photosensitive resist. This process is illustrated in Fig. 1.3.

Fig. 1.3 shows a schematic of an indirect patterning of a layer of polyimide precursor. The schematic shows a simplified stack but all parameters and resist polarities are the same. First, a layer of positive tone resist, AZMIR701 [171], is spin coated at 4000 RPM (Fig. 1.3(b)) on the layer of uncured PI precursor (Fig. 1.3(a)). The resist is soft baked for ninety seconds at 90°C.

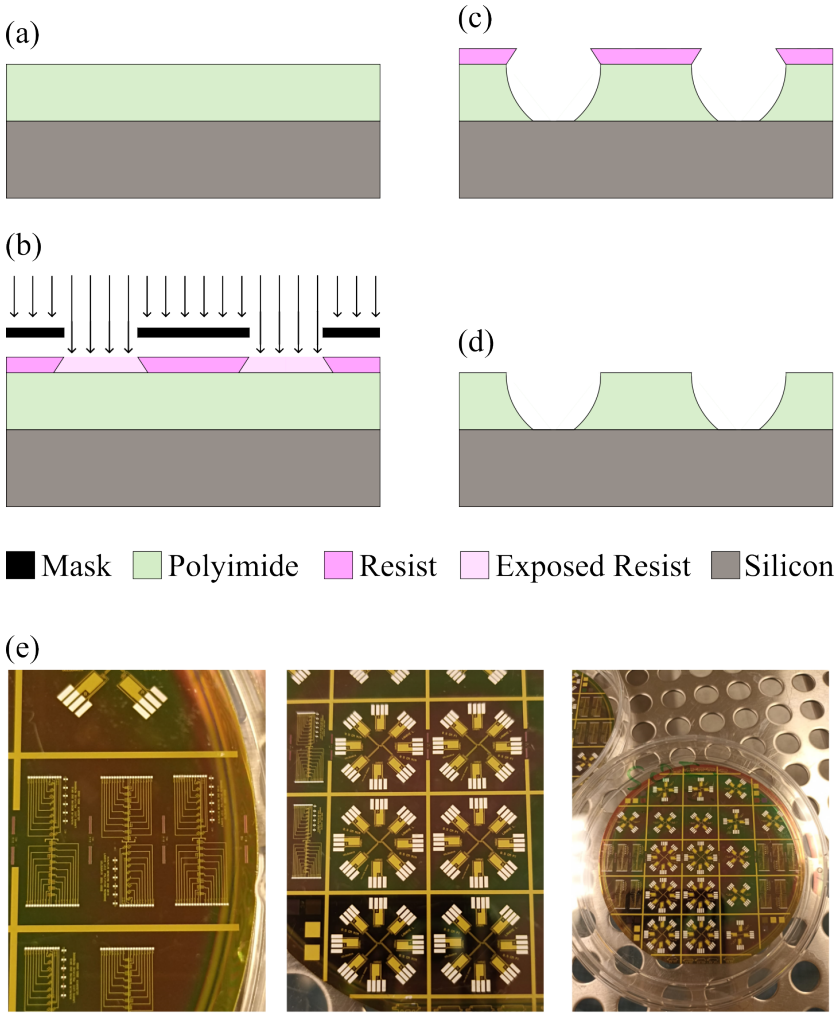


Fig. 1.3 Process schematic of the PI2545 precursor patterning: (a) Spin coating of the precursor and soft bake. (b) Spin coating of a conventional photoresist, soft bake, exposure and PEB. The schematic shows a positive tone. (c) Puddle development with a TMAH-based developer. The photoresist gets developed and the underlying, uncured, polyimide precursor is etched away by the developer. (d) Selective removal of the photoresist with PGMEA and final cure. (e) Picture of a fully processed wafer. The wafer carries silicon resistors, PN and NPN junctions. The wafer is coated with a 3.6 µm-thick layer of polyimide which gives it its golden tint. The white squares are the contact pads made out of aluminium. The polyimide layer was patterned by an indirect photolitography of the polyimide precursor.

The layer is exposed using a 365 nm light source with a constant dose of 180 mJ/cm^2 in vacuum contact. A post exposure bake is done to partially harden the resist at 110°C for ninety seconds. Fig. 1.3(c) represents the development process. A puddle development, without vibration, of one minute with MIF726 [170] developer is done. First, the exposed part of the resist is developed. The developer then quickly etches away the uncured polyimide, leaving openings. At this stage, the top resist must be removed before the final cure.

To do so, PGMEA is dispensed in three steps in a puddle. Each puddle is left for a duration of one minute. PGMEA is very efficient at selectively removing the top layer of photoresist from the polyimide layer [168]. Acetone is shown to degrade uncured polyimide and must be avoided. The layer of precursor is finally annealed for one hour at 350°C. The cured layer is measured to be 3.6 µm-thick by profilometry and ellipsometry. Fig. 1.3(e) shows a macroscopic picture of the wafer with patterned polyimide. The white squares are the opened areas in the polyimide layer, showing the aluminium contact pads.

At this stage the wafer is diced to form 1 cm by 1 cm dies. As illustrated in Fig. 1.1(a) and 1.4(a), each die carries one 2.5 mm-diameter membrane.

Figure 1.2(f) illustrates the membrane release which is done in two consecutive steps. A dry isotropic XeF_2 etch of the back c-Si is done (machine from *Xatic*), resulting in a slight 100 µm over etch and a final membrane of 2.7 mm-diameter.

Finally, the BOX is thinned by a timed isotropic BHF wet etch. A residual silicon dioxide layer of around 200 nm-thick is left to avoid the BHF to enter in direct contact with the silicon devices on the membrane's back side. Fig. 1.4(a) shows a picture of a released membrane. Fig. 1.4(b) shows a zoom on a subset of c-Si devices.

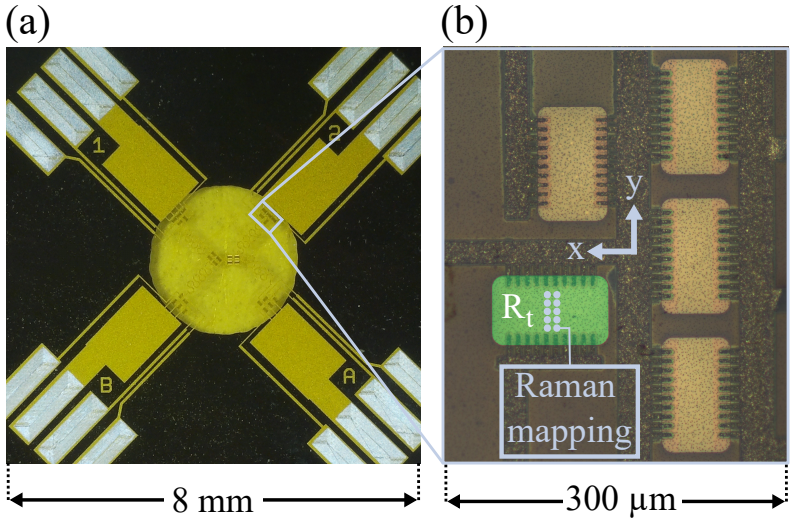


Fig. 1.4 Fabrication results: (a) Top view of a 3.6 µm-thick and 2.5 mm-wide polyimide membrane. (b) Zoom on a subset of devices positioned along the membrane's edge. The device highlighted in green is a p-type resistor arranged in a transverse configuration regarding the direction of the current relative to the direction of the strain. The blue dots represent the 10 mapping points measured by the Raman spectroscope (see next chapter). Uncoloured devices are out of the scope of this chapter.

1.3 Bulge test setup

An instrumentation setup is designed to allow the pressurisation of the PI membrane to induce strain in the silicon devices. The setup, illustrated in Fig. 1.5(a), is made out of a pressure vessel with a device mounted on top. The die to be tested is first glued on an aluminium plate with M-bond 200 [172]. The aluminium plate is pierced to allow the pressure to be transferred to the membrane. The sub-assembly is mounted on the pressure vessel by four screws while an O-ring ensures proper sealing between the plate and the vessel.

The pressure vessel is made out of a machined acrylic block that allows the connection of a pressure generator at the inlet ΔP.

The pressure generator is a KAL-100 from *Halstrup Walcher* which allows the production of controlled pressure in the 0 to 100 kPa range with a 0.05 % accuracy [173]. The assembly is compact enough to be placed under a white light interferometer or a Raman spectrometer as shown in Fig. 1.5(b). Probes can be brought to the device under test. The setup allows to measure the electrical response of the device under strain while doing an *in situ* measurement of the membrane's deflection.

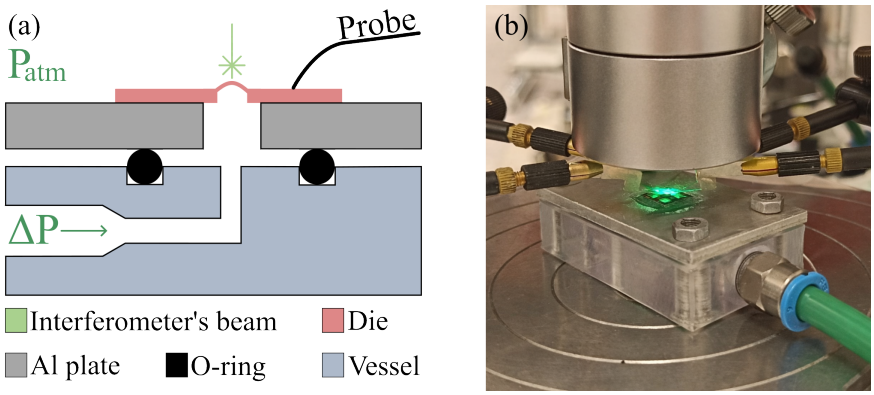


Fig. 1.5 Instrumentation setup: (a) Schematic of the pressure bulge test setup. A die carrying a polyimide membrane is glued on a 5 mm-thick aluminium plate which is itself mounted on a pressure vessel via four screws. Air tightness is ensured by an O-Ring. The pressure vessel is connected to a pressure generator and the whole setup is placed under the lens of a white light interferometer. Probes are used as electrical connexions to the devices. (b) Picture of the installed setup. The green light is the spot of the interferometer.

1.4 Deflection measurement

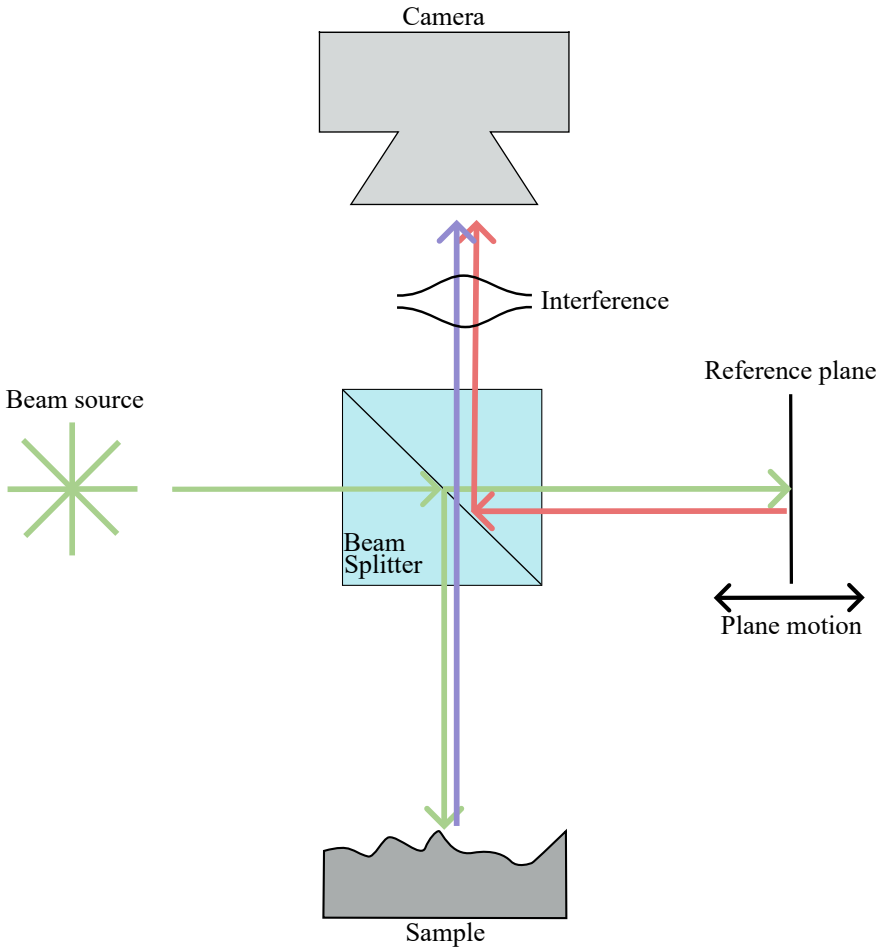


Fig. 1.6 Schematic of a white light interferometer. Adapted from [174]

The measurement of the deflection is carried out by a white light interferometer from *Polytec* [174]. This non-destructive measurement allows to obtain the local deflection profile of the bulged membrane [175]. Fig. 1.6 represents a schematic of a Michelson interferometer, adapted from [174]. The measurement principle relies on the creation and the capture of an

interference pattern on the measurement camera [175, 174]. First, a white light beam is emitted by a photodiode and guided through a beam splitter. Half the beam gets directed toward the sample and the other half goes to a reference plane mounted on a motor in order to change its distance to the beam splitter. Both beams are reflected, one by the reference plane and the other by the sample, and recombine in the beam splitter before being measured by the camera. When both optical paths, to the plane and to the sample, are of the same length, a constructive interference between the beams appears and leads to a spot of maximal light intensity on the pixels of the camera. A measurement of the height of the sample is made by recording the position of the reference plane. The reference plane is then moved, in a predefined range, to get a sweep of interferences across the whole sample and, in consequence, a 3D measurement of the surface topography of the sample.

To get a measurement of the deflection of the membrane as a function of the pressure, a die carrying a released polyimide membrane is mounted on the bulge test setup. The pressure is increased by steps up to a maximum of 100 kPa, which is the limit of the *kal-100* [173]. At each step a measurement of the deflection profile is made by white light interferometry.

Fig. 1.7(a) shows a selection of raw deflection profiles measurements made with the white light interferometer. The measured sample is the 2.7 mm-wide and 3.6 µm-thick polyimide membrane fabricated in this chapter. The represented deflection profiles are measured at 0, 20, 40, 60 and 80 kPa. The raw measured Polytec profiles are levelled to remove the die inclination. This processing is illustrated by the difference between Fig. 1.7(a) and Fig. 1.7(b). The levelling is done by fitting a first order polynomial to the die's edge and subtracting it to every measurement point. This produces a levelled set of deflection curves on which the maximal deflection is measured.

Fig. 1.8 shows a plot of the maximal deflection as a function of the applied pressure. This plot is obtained by measuring the maximal deflection point on each measured and levelled deflection profile. The presented results are the ones of a 2.7 mm-wide and 3.6 µm-thick polyimide membrane bulged to 80 kPa. The 0 kPa pressure point is not reported because the released membranes do not have a flat profile due to residual stress in the stack inducing buckling [176].

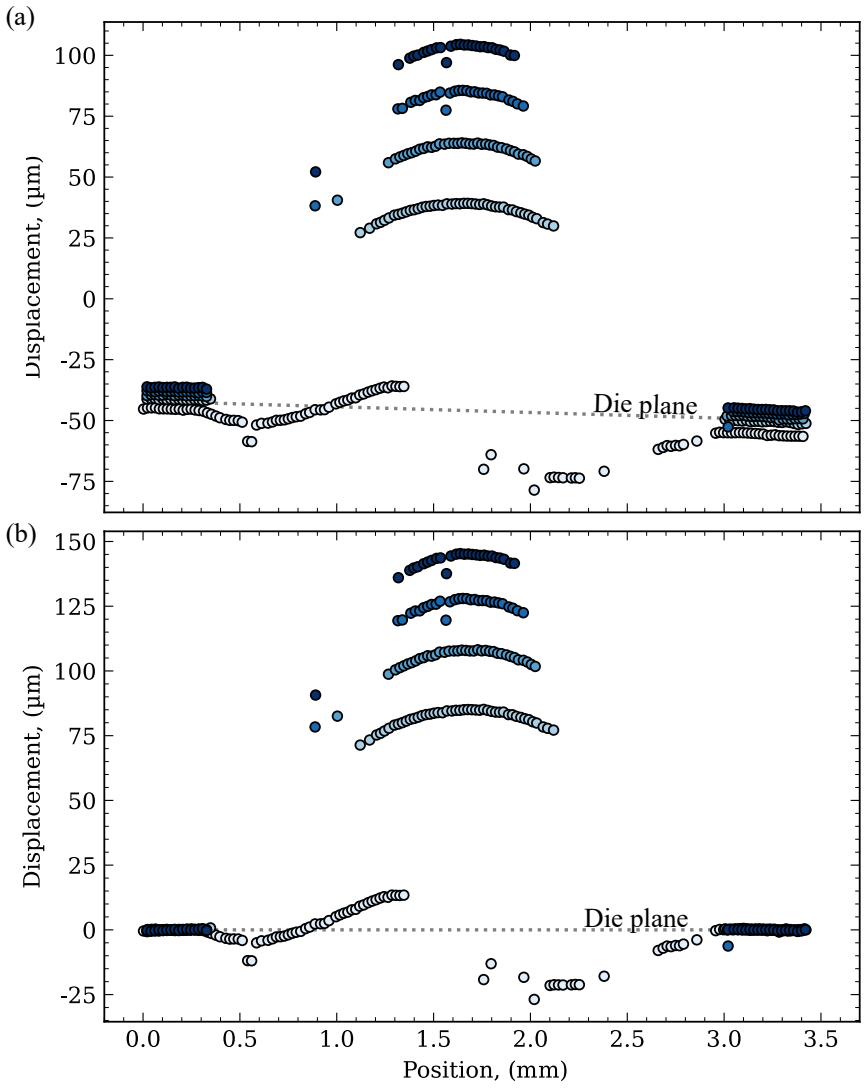


Fig. 1.7 (a) Raw Polytec measurements of a 2.7 mm-wide and 3.6 µm-thick polyimide membrane bulged to 80 kPa. The represented deflection profiles are measured at 0, 20, 40, 60 and 80 kPa. The measurements are tilted due to the inclination of the die during the measurement. (b) Levelled deflection profiles. The presented deflection profiles are the same as in (a) but levelled by subtracting a first order polynomial fitted on the die's edge.

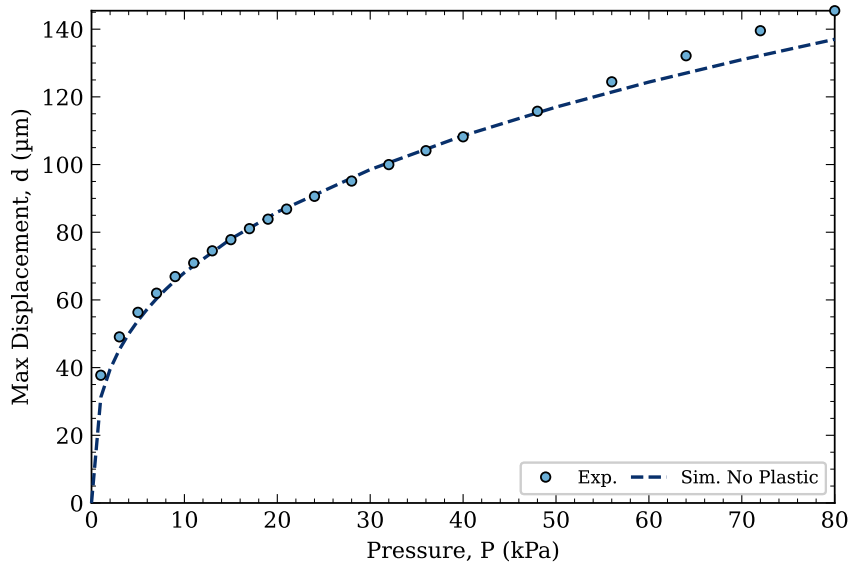


Fig. 1.8 Measurement of the maximal deflection of a 2.5 mm-wide and 3.6 µm-thick polyimide membrane bulged to 80 kPa of pressure. The zero kPa pressure point is not measured since the released membrane is not plane due to residual stresses in the stack.

Fig. 1.8 also shows a preliminary simulation result obtained by modeling the stack in *Comsol Multiphysics*. It considers that the stack follows a fully elastic deformation when pressurised. This is the same assumption as found in [177, 178]. This gives birth to a non-linear cube-root trend which is expected for large deflection scenarios of thin film membranes [177, 178]. As can be seen in Fig. 1.8, both the experimental result and the *No Plastic* simulation follow the same trend up to 50 kPa. Past this pressure point, the experimental measurement starts to deviate from the cube-root trend of the *No Plastic* result. This deviation comes from the entrance of the stack in a plastic deformation regime [179]. This non elastic profile, means that conventional models of membrane deflection cannot be used to estimate its deflection and the local strain in the devices.

1.5 Conclusion

This chapter reports the integration of c-Si resistors on a 3.6 µm-thick and 2.7 mm-diameter polyimide MEMS membrane using a monolithic processing scheme. p-doped, patterned, c-Si resistors are fabricated without process limitation or thermal budget. This is done by spin coating a polyimide precursor at the end of the process.

This technique allows to use high-temperature processing technique and enables the integration of any materials onto a flexible substrate. Furthermore, this process does not require a layer transfer as opposed to [180, 130]. This means that no specialised alignment tools or techniques are required. Also, it makes the process wafer scale due to the spin coating approach. The developed process is however not adapted, in its current form, for mass production of flexible devices due to the required silicon substrate etching. Completely free-standing devices would required a complete sacrifice of the substrate which makes the process unlikely economically viable. A solution would be to design a sacrificial buffer between the active layer and the handling substrate.

A compact *bulge test* setup is assembled to pressurise the membrane to induce strain in the devices. The *bulge* setup allows for precise induction of pressure up to 100 kPa [173]. It can be placed under a white light interferometer or Raman spectrometer for characterization while allowing probes to be brought to the device. The complete platform, membrane and instrumentation, makes for an interesting framework to electrically characterise devices under strain.

The membrane is measured, in a preliminary test, up to 80 kPa. Its maximal deflection with the pressure follows an expected cube-root trend up to 50 kPa [181, 177, 178]. Past this point, it diverges from the cube-root profile and reaches a final deflection of 145 µm. This deviation is expected to come from the entry of the stack in a plastic deformation regime [182]. This is an issue since it makes the use of available elastic model impossible [181, 177, 178]. This also means that we lack a model to predict the strain induced in the device under test.

In the next chapter, the plastic deformation hypothesis is tested. A *Comsol* FEM model that takes the plastic effect into consideration is presented. It will be used to compute the strain induced in the microfabricated devices integrated on the polyimide membrane.

1.6 Take home messages

- A process for the monolithic and wafer scale integration of devices made from c-Si, or other materials, on wide and thin polyimide membrane is presented.
- A *bulge test* setup to pressurise the membrane up to 100 kPa is introduced. It allows for multiphysics and *in situ* characterization of microfabricated devices.
- A 2.7 mm-wide and 3.6 µm-thick PI membrane is shown to reach a maximal deflection of 145 µm at 80 kPa. The membrane enters in a plastic deformation regime leading to the need of proper *Comsol* modeling.

2

Modeling and validation of the straining platform with c-Si demonstrators

In the previous chapter, c-Si resistors were fabricated on 2.7 mm-wide and 3.6 µm-thick polyimide membrane. However, preliminary testing showed that the membrane maximal deflection profile cannot be predicted by large deflection models [177, 178, 179].

This chapter introduces a *Comsol* FEM model to simulate the membrane's behavior under pressure. The goal is to compute the strain field induced locally in the device under test, as a function of the applied pressure. This is required since no direct measurement of the strain in the device is possible in a membrane configuration as opposed to direct tensile testing [124, 125]. The fabrication of flexible MEMS membrane for high-deformation application only makes sense if the local strain in the device under test can be obtained as a function of the pressure. To do so, proper modeling of the stack is required.

The parameters of the FEM model are fitted on the measured deflection profile and the local strain in the c-Si devices located alongside the edge of the membrane is recovered.

2 | Modeling and validation of the straining platform with c-Si demonstrators

The integration of c-Si devices as the first demonstrator is intentional as it allows to use Raman spectroscopy to confirm the FEM results. The fabricated c-Si devices are measured under a Raman spectrometer to recover a pressure/peak-shift relation. This experimental result is compared to a computation of the peak-shift made using the results of the FEM model and the phonon-deformation potential (PDP) theory.

This part of the manuscript tries to answer the following scientific question:

Can a Comsol simulation model the plastic deformation of a polyimide membrane to compute the local strain field induced in the carried c-Si devices and how much strain can be induced in the c-Si resistors?

To answer that question, this chapter presents:

- **A Comsol** model of the membrane that takes into account the plastic deformation of the stack.
- **A fitting** of the model on an experimental measurement of the maximal deflection of the membrane, as a function of the pressure.
- **Strain field computation** locally in the c-Si device. The full strain tensor is recovered from the model.
- **Raman validation** of the strain field. The shift of the c-Si Raman peak is measured as a function of the pressure and used to validate the strain field computation made by the plastic *Comsol* model.

2.1 Membrane modeling

Due to the radical differences between the presented membrane stack which uses a low Young's modulus polyimide and a conventional silicon bulk micro-machined or stress compensated MEMS membrane, the behavior of the membrane cannot be predicted by usual analytic models like in [155, 157]. Those models provide analytical pressure-deflection relationship as well as hypothesis and analytical estimations of the strain components around the edges of the membrane. Furthermore, as shown in Fig. 1.8, the stack enters in a plastic deformation regime past a certain pressure level. This renders the use of analytical models for large deflection membranes, like the ones of [181, 177, 178], impossible as well.

To cope with this, a *Comsol Multiphysics* model of the membrane geometry and stack is built. *Comsol* is an integrated FEM software that allows to simulate single or coupled physics of complex geometries and designs. The goal of the model are the following:

- Compute the maximal deflection of the membrane as a function of the pressure in both the elastic and plastic deformation regime.
- Compute the pressure-strain relation locally inside of the microfabricated devices in both deformation regimes.

A numerical twin of the membrane is built based on real measurements of the stack and *xy*-dimensions of the as-fabricated sample. The metallic lines extending from the die to the membrane as-well as the microfabricated devices of interest are also modelled. The simulation uses the *Solid Mechanics* module from *Comsol* to compute the stress, strain and displacement of each node in the mesh [183].

Regarding the plastic behavior of the stack, the *Swift* model [184] is implemented into *Comsol* to compute the actual stress and strain in the plastic regime [184]:

$$\sigma_{\text{eff}} = \sigma_{\text{y,eff}}\left(1 + \frac{\varepsilon}{\varepsilon_{0,\text{eff}}}\right)^{n_{\text{eff}}} \tag{2.1}$$

σ and ε are the actual stress and strain while $\sigma_{\text{y,eff}}$, $\varepsilon_{0,\text{eff}}$ and n_{eff} are respectively the effective yield stress, reference strain and hardening coefficients

to be fitted on experimental data. In this work, only the effective yield stress and hardening exponent are used as fitting parameters. This is because preliminary testing showed that neither the maximal deflection nor the strain curve, relative to pressure, are impacted by the reference strain. According to [184], the reference strain is used when the material under test is pre-strained, which is not the case in this work.

Model fitting

In order to get a proper estimation of the local strain in the fabricated devices, the model is fine tuned by fitting the maximal deflection of the membrane, relative to the pressure, with experimental data. The model is fitted following the protocol presented here below. Note that for each new fitting step, the parameters from the previous ones are preserved.

Experimental measurement

The fabricated sample must be fully characterised. The model takes as input the thickness of all the different layers as well as the real *xy*-dimensions of the membrane. An experimental measurement of the maximal deflection of the membrane, relative to the pressure must also be made.

Stack fitting

In some cases, getting a precise measurement of the thickness of each layer in the stack is not possible. For instance, the process presented in this chapter ends with a *"timed isotropic BHF wet etch"* of the BOX. This means that the exact thickness of the residual SiO_2 is unknown and can only be estimated based on the duration of the wet etch. In this case, an estimated 200 nm-thick layer of SiO_2 is expected to remain. A proper estimation of the thickness of the residual BOX is paramount as it greatly impacts the stiffness of the membrane. Fitting of the unknown thickness in the stack is done before fitting the plastic parameters.
Fig. 2.1 illustrates the impact of the SiO_2 thickness in the stack. Five different layers are tested between 200 and 500 nm. Increasing oxide thickness is represented by plain line with squares from dark blue to light blue. The overall maximal deflection profile of the membrane diminishes as the residual BOX thickness increases. For this test, the simulation is done without the plastic module, as visible in the cube-root trend of the deflection profile [177, 178, 179].

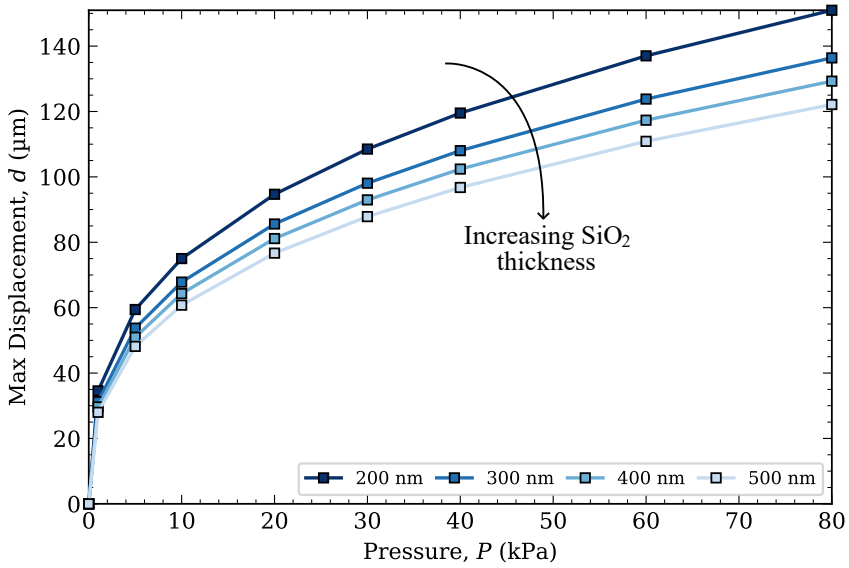


Fig. 2.1 Impact of the thickness of the silicon dioxide layer on the maximal displacement of a 2.5 mm-wide, 2.5 µm-thick, polyimide membrane. Four simulation results from the *Comsol* model are presented by plain blue lines with squares. Dark to light blue is used to represent the tested thicknesses of 200, 300, 400 and 500 nm, respectively. The overlaid arrow represents the increase of silicon dioxide layer thickness.

Yield stress

The yield stress determines when the stack transitions from an elastic deformation to a plastic one. A lower yield stress makes the stack enters earlier in a plastic deformation regime [184]. This is well illustrated in Fig. 2.2. Four yield stresses are tested between 400 and 600 MPa. They are represented by plain lines with squares from dark to light blue for increasing values of the yield stress. The entry in the plastic regime is observed to happen at lower pressure for lower values of the yield stress.

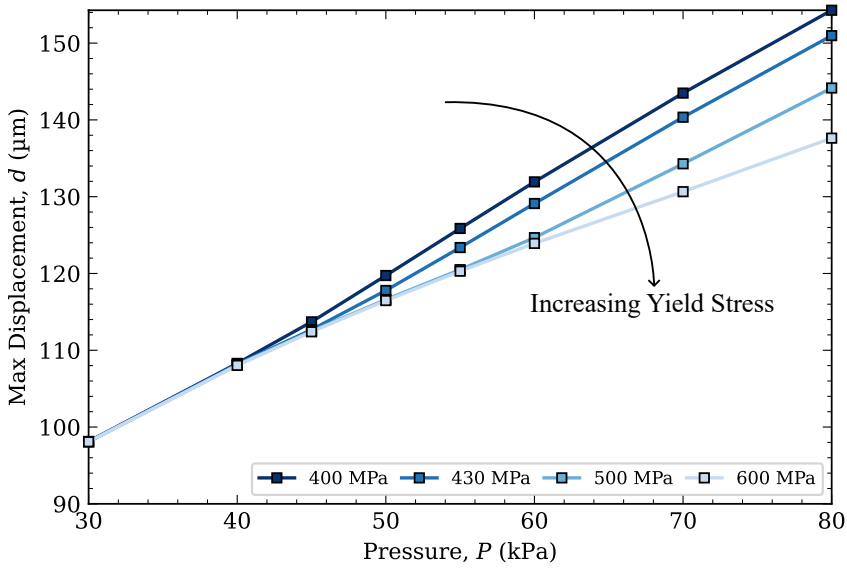


Fig. 2.2 Impact of the yield stress, $\sigma_{y,eff}$, on the plastic regime of an inflated, 2.5 mm-wide, 2.5 µm-thick, polyimide membrane. Four simulation results from the *Comsol* model are presented by plain blue lines with squares. Dark to light blue is used to represent the tested yield stresses of 400, 430, 500 and 600 MPa, respectively. The overlaid arrow represents the increase of the yield stress.

Hardening exponent

The fitting of the hardening exponent is illustrated in Fig. 2.3. The hardening determines the slope of the stress-strain curve once in a plastic deformation regime and, in turn, the slope of the pressure-deflection curve in the plastic deformation regime [184]. Four different hardening exponents are tested from 0.01 to 10 and represented by plain lines with squares from dark to light blue. The slope can be seen to decrease as the hardening exponent increases.

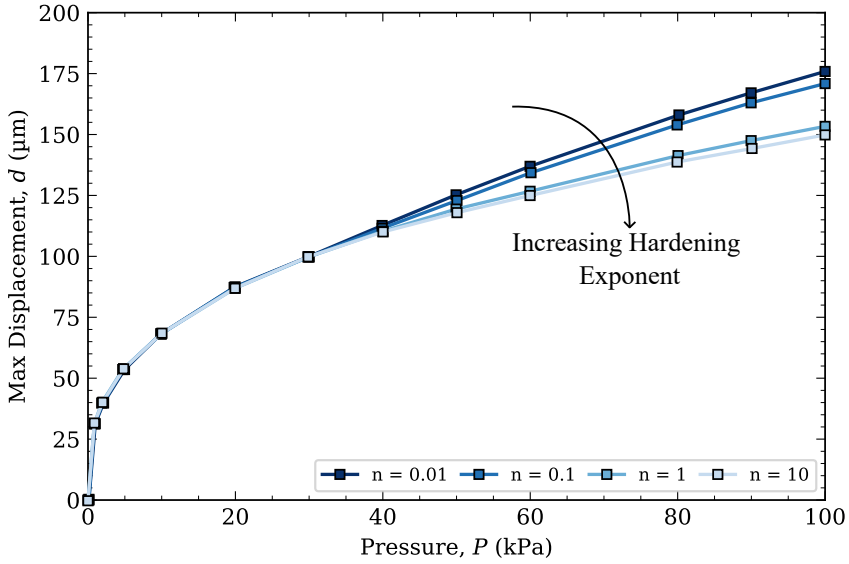


Fig. 2.3 Impact of the hardening exponent, n_{eff}, on the plastic regime of an inflated, 2.5 mm-wide, 2.5 µm-thick, polyimide membrane. Four simulation results from the *Comsol* model are presented by plain blue lines with squares. Dark to light blue is used to represent the tested hardening exponents of 0.01, 0.1, 1 and 10, respectively. The overlaid arrow represents the increase of the hardening exponent.

Experiment modeling

The model is adapted to the particular design of the experiment. It is built according to the real dimensions of the as-fabricated membrane to take into account the process non-idealities such as the over-etch. The simulation model is made out of a stack comprising a 200 nm-thick thermal silicon dioxide layer, the active 300 nm-thick patterned c-Si, the 180 nm-thick PECVD silicon dioxide layer and a 3.6 µm-thick polyimide layer similar to the one presented in Fig. 1.2. A 2.7 mm-diameter circular membrane with c-Si devices located around its perimeter is simulated. The materials Young's moduli are set to 87 GPa [185] and 2.7 GPa [168] for the SiO_2 and PI, respectively. The stiffness matrix of silicon, $\mathbf{C_{Si}}$, is used to take into account the material anisotropy [186, 187]. In our case, the principal strain components, ε_{xx} and ε_{yy}, are along $\mathrm{Si}_{\langle 110 \rangle}$.

Fig. 4.4(a) shows the full 3D model of the membrane. A quarter is simulated to lower the computational cost. Symmetry conditions are applied at the boundaries. Fig. 4.4(b) shows a zoom on the devices. In the model, both the aluminium lines and devices are taken into account according to the real design of the die, as shown in Fig. 1.1. The contact fingers are not simulated because including them requires the use of very small mesh elements which renders the computational cost to high. The over etch of the membrane due to the XeF_2 release in taken into account. A 2.7 mm-wide membrane is simulated as opposed to the 2.5 mm-width originally intended. This affect the position of the devices relative to the edge of the membrane. Fig. 4.4(c) shows the stack of the membrane without the bulk silicon for clarity.

The 180 nm-thick PECVD layer and the 200 nm-thick thermal SiO_2 layer are treated as one layer located below the c-Si device. In practice, the silicon island is located between the two. Preliminary testing showed that building the model as in Fig. 4.4(c) does not impact the computed strain field while allowing to reduce the computational cost. The represented thickness of 320 nm is lower than the initially estimated thickness of 380 nm. This is because the schematic shows the stack used after calibration with an experimental measurement. This is further explained in the next section.

2.2 Deflection results

A die carrying a 2.7 mm-diameter membrane is mounted on the bulge test setup and the deflection profile of the membrane is measured. The additional pressure above atmospheric, ΔP, ranges from 1 to 80 kPa by steps of 1 kPa up to 22 kPa, 2 kPa up to 40 kPa and 4 kPa up to 80 kPa. The pressure is then lowered following identical steps down to 1 kPa. The 0 kPa pressure point is not measured because the released membranes do not have a flat profile because of residual stress in the stack inducing buckling [176].

Deflection results of a 3.6 µm-thick and 2.7 mm-diameter polyimide membrane are presented in Fig. 2.5. A subset of five raw deflection profiles is illustrated in the figure's inset. A gradient of color from light to dark green is used to represent increasing pressure levels at 10, 20, 40, 60 and 80 kPa.

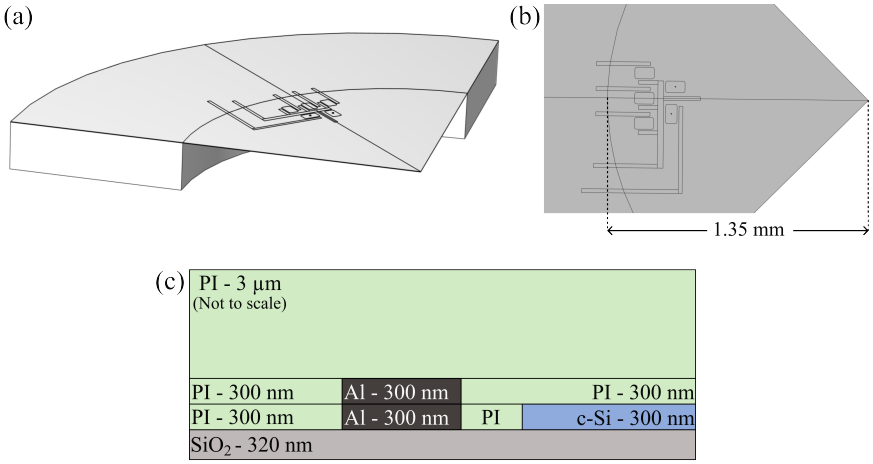


Fig. 2.4 Comsol model of the 2.7 mm-wide and 3.6 µm-thick polyimide membrane: (a) Overview of the complete model. A quarter of the membrane is simulated to reduce computational cost. (b) Zoom on the c-Si devices and aluminium lines. (c) Stack simulated in the model. The thermal and PECVD SiO_2 are treated as a single continuous layer and shown in gray. The aluminium is in black, the c-Si in blue and the polyimide in green.

Green dots are used to represent the experimental data while dashed lines represent the least-square error approximation of a second-order polynomial. The membrane bulge increases with the pressure to reach a maximal deflection of 145 µm relative to the die plane at 80 kPa.

The main plot reports the maximal deflection measured at each intermediary step. Measurements are displayed as light and dark blue dots for increasing and decreasing pressure, respectively. Plain lines are used to display the simulation results using the same color code. The dashed line is a simulation of the stack but without the *Swift* model.

Upon pressurisation, the maximal deflection of the membrane follows a non-linear cube-root trend as expected for large deflection scenarios [177, 178]. The deflection curve follows this trend, which is perfectly modelled by both simulation models up to 50 kPa. Past this point, both the plastic simulation and the experimental data start to diverge from the non-plastic simulation. The deflection continues to increase up to the reported maxima at 80 kPa.

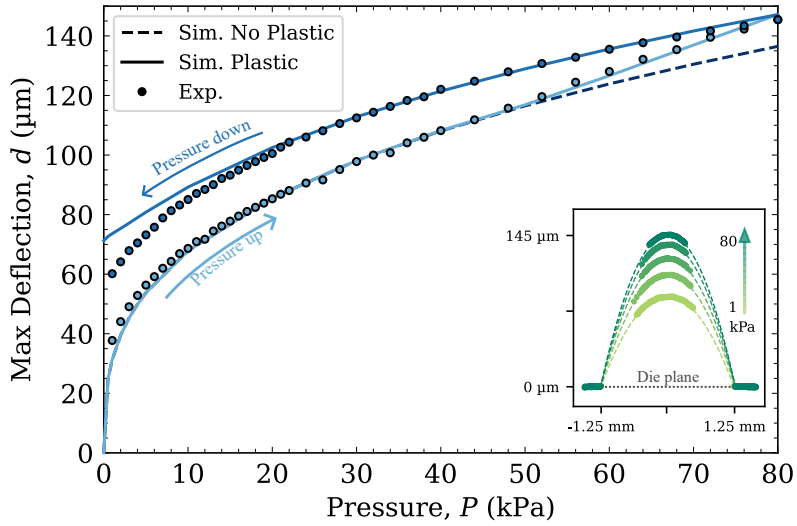


Fig. 2.5 Deflection measurement of a 3.6 µm-thick 2.7 mm-diameter circular polyimide membrane: The inset shows a selection of local deflection profiles under increasing pressure at 10, 20, 40, 60 and 80 kPa taken by a white light interferometer. The main plot shows the maximum of each raw deflection curve for pressure ranging between 1 and 80 kPa and then 80 to 1 kPa. Light and dark blue circles are used for experimental data points for the up and down pressure sweeps, respectively. The plain lines represent the simulation considering plasticity for both the up and down pressure cycles with the same color code. The dashed line represents a simulation that does not consider plasticity.

When the pressure starts diminishing, both the simulated and measured maximal deflections start to decrease. The two curves follow a trend parallel to the dashed line which simulates the expected non-plastic behavior of the stack. This relaxation profile is expected and well documented in literature [188]. Once a material entered in a plastic deformation regime, when stress is released, the stress-strain curve follows a linear trend and reaches a permanently deformed final state, which is the case here at 1 kPa at the end of the bulge test. The final relaxed state features a permanently deformed shape with a residual deflection of 60 µm.

The final fitted values of the *Swift* model parameters are $\sigma_{y,\text{eff}} = 450$ MPa and $n_{\text{eff}} = 0.05$. Those effective parameters allow to simulate the plastic behavior of our specific stack and geometry. The model also allows to estimate the residual BOX thickness at around 160 nm. This is well in line with the process based estimation of 200 nm.

2.3 Strain results

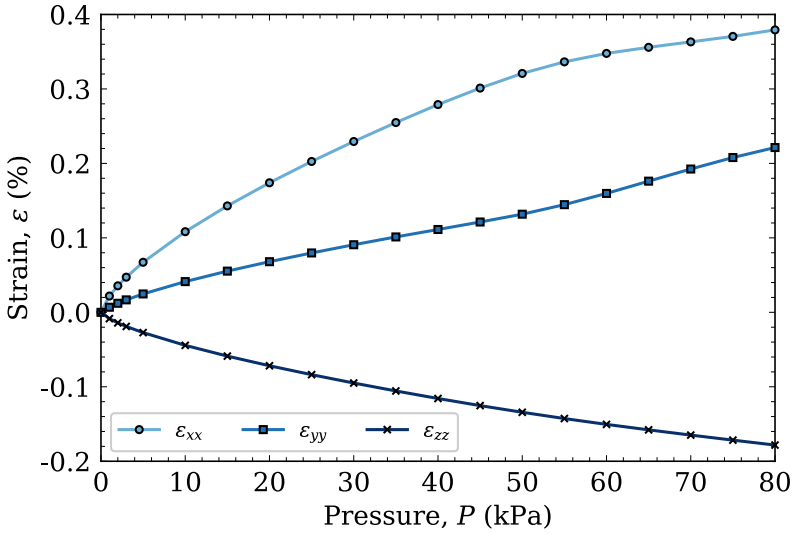


Fig. 2.6 Strain field simulation: Strain field inside a 0.3 µm-thick c-Si device on a 3.6 µm-thick 2.7 mm-diameter polyimide membrane under increasing pressure ranging from 0 to 80 kPa. Circles, squares and crosses are used to represent ε_{xx}, ε_{yy} and ε_{zz}, respectively.

Fig. 2.6 depicts the simulated evolution of the strain field under increasing pressure in R_t. The plot only shows the main x-, y- and z-component as the shear ones are evaluated to be close to zero. As can be read on the graph, the strain field is an asymmetrical biaxial one. This is unlike what is obtained for small deflection setups where devices located on the edge of the membrane undergo uniaxial straining [127, 155].

Upon pressurisation of the membrane, both ε_{xx} and ε_{yy} are steadily increasing and follow a non-linear trend similar to the deflection. This is unlike the linear evolution of strain with pressure reported by the literature for small deflection setups [155, 157].

The entry in the plastic regime of the stack, at around 50 kPa, is visible for both the x and y profiles with a decrease and increase of their respective slope. A maximum of 0.37 % of deformation is obtained for ε_{xx} and 0.23 % for ε_{yy} in R_t. ε_{zz} showcases a steady increase up to -0.18 %. The plasticity of the deformation is not visible for ε_{zz} since it is a linear combination of both the x- and y-component of the strain tensor following:

$$\varepsilon_{zz} = -\nu_{\mathrm{Si}}(\varepsilon_{xx} + \varepsilon_{yy}) \tag{2.2}$$

where $\nu_{\mathrm{Si}} = 0.28$ is the Poisson ratio of silicon [187].

Those results demonstrate the capacity of the flexible PI based platform to induce reasonable strain levels of up to 0.37 % in silicon. This level is more than one order of magnitude bigger than what is achievable with classical bulk micro-machined or stress-compensated membranes that only induce up to 0.04 % of strain in the device under test [127, 128]. The reported deformation is however one order of magnitude lower to the 3.5 % of strain reached by [130]. This is explained by both their thinner 10 nm-thick silicon layer and higher 213 kPa maximum induced pressure.

2.4 Raman validation: theory

In order to properly validate the strain field results obtained from the simulator, a Raman spectroscopy experiment is designed using a LabRAM HR from *Horiba Scientific* equipped with a 514 nm laser. This non-destructive measuring technique allows to obtain Raman spectra which are specific to every material since they depend on their structural configuration [163]. At rest, the Raman spectrum of (100) silicon is made out of three degenerated optical mode centered around 520.7 cm^{-1} [164]. The longitudinal optical mode (LO) dominates the two others (TO) and is the only observable one [164].

Upon straining of the c-Si devices, the modification of the crystal lattice results in a measurable shift of the Raman peak position which is used to validate the simulation model [165].

Similarly to the deflection setup, the peak shift is measured for pressures ranging from 0 to 80 kPa. The measurement is made using a 514 nm laser that first penetrates through the 3.6 µm-thick PI layer. The PI layer does not interfere with the experiment since polyimide features a low absorbance coefficient for green light [189] and only features Raman peaks far from the one of c-Si, at above 1000 cm^{-1} [190].

A 10-point mapping is done at each pressure step by measuring the Raman response of the silicon device at 10 different locations of R_t as illustrated in Fig. 1.4(b). This mapping leads to noise and mismatch measurement reduction and allows the extraction of the average peak-shift value induced by strain in the silicon mesa.

Data processing starts by averaging the 10 Raman spectra of each pressure step. The averaged peak is normalized relative to its own maximum and the obtained data points are fitted by a Lorentzian function [163]. In the case of a (100) top plane c-Si, only the longitudinal optical mode is observable [191]. The maximum value corresponds to this LO peak which is detected around the initial 520.7 cm^{-1} resting position. Doing this for each pressure step provides us with an experimental measurement of the peak shift as a function of the pressure.

To validate our simulation results, we solve the eigen-value problem of [192] based on the secular matrix (2.3) of Ganesan. It is used to compute the pressure-peak shift variation $\hbar\omega_i$ of the three Raman optical modes based on the full non-linear strain tensor given by the FEM simulation. Solving the eigenvalue's problem allows to find the three λ_i and then the shifts using $\hbar\omega_i = \sqrt{\lambda_i - \omega_0^2}$ with $\hbar\omega_0 = 520.7\ cm^{-1}$. Three parameters ($p$, q and r) called the phonon deformation potential (PDP) coefficients are used. In this work, coefficients reported by [193] and [194] are used.

Solving the eigenvalue problem based on (2.3) using the *Comsol* strain tensor provides us with a theoretical estimation of the strain/peak-shift relation that can be compared with the actual Raman experimental data [179].

$$\begin{vmatrix} p\varepsilon_{11}+q(\varepsilon_{22}+\varepsilon_{33}) & 2r\varepsilon_{12} & 2r\varepsilon_{13} \\ 2r\varepsilon_{12} & p\varepsilon_{22}+q(\varepsilon_{33}+\varepsilon_{11}) & 2r\varepsilon_{23} \\ 2r\varepsilon_{13} & 2r\varepsilon_{23} & p\varepsilon_{33}+q(\varepsilon_{11}+\varepsilon_{22}) \end{vmatrix} = 0 \quad (2.3)$$

2.5 Raman validation: results

Fig.2.7 highlights the results of the Raman validation experiment. The inset provides a selection of raw Raman spectra at increasing pressure levels of 10, 20, 40, 60 and 80 kPa. The shift of the maxima can be seen in the inset.

The main plot reports the evolution of the silicon LO peak position as a function of the pressure between 0 and 80 kPa. The experimentally obtained data is represented as blue dots. The simulation of the Raman peak shift is provided by the plain blue lines. They are computed based on the simulated strain tensor for two different sets of p,q and r PDP coefficients provided by [193] and [194].

Contrary to what is usually found in literature, the complete strain field obtained from the FEM model is used to estimate the Raman peak-shift instead of the other way around. Indeed, paper such as [130] uses Raman spectroscopy to get an indirect measurement of a given component of the strain. They rely either on an empirical peak-shift/strain relationship as in [130, 195] or on a simplification of the full Ganesan matrix as in [196] to get a strain measurement based on a Raman experiment. While successful, this approach only works when an empirical peak-shift/strain relation is available and when strong assumptions can be made on the shape of the strain field.

In this work, the opposite is done. Instead of using Raman spectroscopy to measure the strain, we get the strain from an FEM model and use the full tensor to compute the Raman peak-shift and compare it to an experimental measurement. This allows the use of the full strain tensor without *a-priori* knowledge on its shape and components. As visible in Fig.2.7, a good agreement between the simulation and the measurement is obtained.

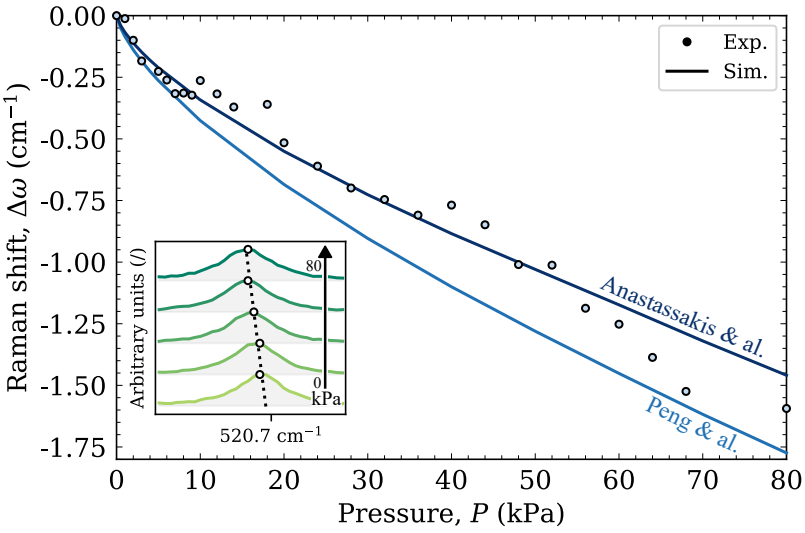


Fig. 2.7 Raman silicon peak shift: Raman peak shift measured into a 0.3 µm-thick c-Si resistor on a 3.6 µm-thick 2.7 mm-diameter polyimide membrane under increasing pressure levels. The inset represents the raw Raman spectrum of the silicon at pressures of 10, 20, 40, 60 and 80 kPa. The main plot shows the evolution of the position of the LO optical mode. Blue dots represent the experimentally obtained peak shifts. Plain light and dark blue lines represent the simulated peak shift obtained using the PDP coefficients from Peng and al. [194] and Anastassakis and al. [193] in R_t, respectively.

Since the experimental peak shift is an expression of the impact of the complete non-linear biaxial strain field in silicon, this gives us strong confidence in the simulated strain tensor. The deviation between the FEM model and the experimental measurement is explained by the angle of incidence of the Raman laser. The important deflection of the membrane leads to the inclination of the c-Si devices. An angle of 3.6° is reached at 5 kPa, 5.6° at 10 kPa and 9.6° at 80 kPa , relative to the die plane. This induces a Raman response from the (TO) phonon optical modes. This additional contribution to the Raman spectrum reduces the accuracy of the LO peak extraction[197, 198].

This validation, made on a canonical material like silicon, implies that our simulation framework is valid and can be used to predict the induction of strain in p-VO_2 devices, as presented in the next chapters. This is because, for the *Comsol* model, the only difference between c-Si and p-VO_2 is its Young's modulus. This is of particular interest since VO_2 features a multi-peaks Raman spectra for which no empirical strain-shift relations are available.

Furthermore, the agreement between the simulated and experimental strain tensor demonstrates that fitting the simulation parameters on a measurement of the deflection of the membrane is sufficient to precisely estimate the strain in the electrical devices. It also demonstrates proper adhesion and hence stress transfer from the membrane to the c-Si device without slippage or delamination of the film.

2.6 Conclusion

This chapter reports the modeling of strain in c-Si resistors fabricated on a 3.6 µm-thick and 2.7 mm-diameter polyimide MEMS membrane using a *Comsol Multiphysics* FEM model fitted on a measurement of the membrane deflection [179]. The *Swift* plastic model [184] is implemented in *Comsol* to simulate the behavior of the membrane. The relative stress, strain and hardening exponent are fitted on an experimental measurement of the membrane deflection under pressure to calibrate de model. An excellent agreement between the simulated and measured deflection is obtained in both the plastic and elastic deformation regime.

The strain field in the c-Si resistors is found to be non-linear and biaxial. This is unlike what is obtained for small deflection setups where devices located on the edge of the membrane are expected to undergo uniaxial straining [127, 155]. A maximal strain of 0.37 % is obtained in the silicon along the x-direction. This is a 10-fold increase compared to conventional bulk micro-machined or stress compensated membranes [127, 128]. It however is 10-times lower than what is reported by [130] but this is linked to their use of ultra-thin 10 nm-thick silicon devices compared to our 300 nm-thick pixels. The shear components are evaluated close to zero.

The validity of the simulated strain field is checked by Raman spectroscopy. A technique based on the resolution of Ganesan secular equation using the simulated strain tensor is used. Excellent agreement of the simulation and Raman experiment allows to have strong confidence in the simulated strain field. This agreement demonstrates that fitting the simulation parameters on a measurement of the membrane deflection is sufficient to predict the local strain field in the device.
This chapter validates the following methodology to perform high-strain studies on any material without the need for *in situ* strain measurement:

i Fabrication of the device to be strained via conventional processing techniques.

ii Integration on flexible substrate.

iii Measurement of the membrane deflection under pressure.

iv Fitting of the simulation parameters to obtain a complete pressure-strain field relation.

The rest of the work details the use of this methodology to characterise strained p-VO_2 resistors.

2.7 Take home messages

- A *Comsol* FEM model is developed to model the deflection profile of a large polyimide membrane in both the elastic and plastic deformation regime. Both the up and down pressure sweeps are properly modelled by the FEM simulation.
- The *Comsol* FEM model fitted on an *in situ* measurement of the maximal deflection of the membrane allows to compute the full strain tensor inside of integrated devices.
- The strain field is validated by simulating the Raman peak-shift in c-Si using the PDP theory and comparing it to an experimental measurement of the shift in the devices.

3

p-VO_2 integration on a thin-polyimide membrane

The previous two chapters established the processing techniques, simulation tools and experimental setups required to fabricate and characterise c-Si devices up to 0.4 % of strain. In this chapter, we explore the process required to integrate thermally annealed p-VO_2 onto polyimide.

As already established, the monolithic process presented in this work renders the integration of materials that require high-temperature processing compatible with soft polymers like polyimide. This is of interest since the integration of VO_2 on polymers relies on the complex and hard to scale transfer of the layer [146, 89] or on low temperature processes [139, 140, 141, 142, 131, 143, 144] which yield layers of low crystallinity [145, 146, 140]. Monolithic direct integration of high-quality [145, 147] sputtered p-VO_2 layers onto flexible substrate is of interest but remains out of reach due to the limited thermal budget of polymers [150, 150, 151] and the high-temperature annealing required to reach the desired level of crystallinity [152, 153, 154].

In this chapter, the monolithic integration of thermally annealed p-VO_2, deposited by sputtering, onto polyimide is presented. First, the synthesis of the material and deposition protocols are detailed. The characterization steps, required to check the quality of the film in terms of grain size

and stoichiometry, are presented. Once done, a proof of concept of the monolithic integration on polyimide is presented. This demonstration integrates a blanket layer of p-VO_2 onto a released polyimide membrane. This demonstration is required for two reasons:

- **Adhesion testing:** Before rushing into the integration of patterned p-VO_2 devices on polyimide, the adhesion between the materials and the process feasibility must be tested.
- **Young's modulus:** A measurement of the Young's modulus of the as-deposited p-VO_2 is critical to get a proper estimation of the strain from the *Comsol* model, in the next chapter. Values from the literature span over a wide range for p-VO_2, which renders the measurement of the modulus of the deposited thin film paramount [161, 160, 162].

This chapter tries to answer the following research question:

How to integrate thermally annealed p-VO_2 on a thin, released, polyimide membrane to recover its Young's modulus?

To answer that question the following elements are tackled:

- **Synthesis:** The processing of vanadium into p-VO_2 via reactive sputtering is presented. The details on recipe calibration as well as the key deposition and annealing parameters are explored. The fundamental characterization steps to attest of the correct stoichiometry of the as-deposited thin film are discussed.
- **Adhesion testing:** A preliminary fabrication process is proposed to demonstrate the feasibility of the integration of p-VO_2 on a polyimide thin film. A blanket layer of p-VO_2 is deposited and covered with an unpatterned PI layer.
- **Young's modulus:** Using the demonstrator, a measurement of the Young's modulus is performed. This is done by fitting a maximal deflection simulation of the stack on an experimental bulge measurement.

The goal of this chapter is to prepare the ground for the integration of p-VO_2 resistors on a thin and wide polyimide membrane for high-strain studies, in the last chapter.

3.1 VO_2 synthesis

This section details the generic process and parameters used to synthesize polycrystalline vanadium dioxide (p-VO_2) thin films. A combination of two techniques is used: room temperature reactive sputtering and thermal annealing [199, 200, 201, 202]. The protocol detailed here below is strongly inspired for the previous work made internally at the Winfab facility of the UCLouvain and well detailed in [154, 203, 204].

The deposition is done in a sputtering chamber from AJA International [205]. The reactor is represented in Fig. 3.1(a) while Fig. 3.1(b) shows a picture of its inside. Sputtering works by the injection of argon gas between two electrically biased electrodes, generating a plasma [206, 207, 208, 209]. The argon ions from the plasma are attracted and accelerated toward a target of material, at the bottom of the schematic in Fig. 3.1(a). The high-energy impact of the argon ions with the target generates a plume of striped atoms from the target that deposits onto the sample. The deposition plume is shown in blue in Fig. 3.1(a). Contrary to a thermal evaporation, the vacuum induced in the chamber is quite low and the atoms from the deposition plume arrive on the sample with high kinetic energy and with a randomised incidence angle. This leads to the deposition of materials with good conformity on the final sample, at the top of Fig. 3.1(a) [210, 211].

In this work, a 99.9 % pure vanadium sputtering target from *Neyco* is used [212]. A 100 % argon sputtering of this target results in the deposition of a metallic layer of amorphous vanadium onto the sample of interest. To obtain a stoichiometric layer of vanadium dioxide, the use of reactive sputtering is required. This works by precisely controlling the power, the pressure and the gaz mixture in the plasma to obtain the oxidation of the sputtered vanadium plume into vanadium dioxide [213, 214, 215, 216]. By controlling those parameters, stoichiometric a-VO_2 is deposited onto the sample of interest. The access ports for the vacuum and the gases are visible in the schematic of Fig. 3.1(a).

The chamber allows to sputter material at room temperature. This means that the growth of VO_2 crystal cannot occur during the deposition step but must be handled afterwards.

After sputtering, the obtained layer is amorphous. Thermal annealing is used to allow the spontaneous growth of VO_2 crystallites from amorphous to polycrystalline [152, 153]. By controlling the annealing temperature, a tuning of the final grain size is achieved [154]. The spontaneous growth of the crystals is possible since the a-VO_2 is deposited on a thermally oxidised bulk silicon wafer. The amorphous SiO_2 allows to separate the VO_2 from the lattice of silicon, which renders its crystallisation possible [154].

This section provides all the details about the specifics of the process required to obtain stoichiometric p-VO_2 using reactive sputtering and thermal annealing.

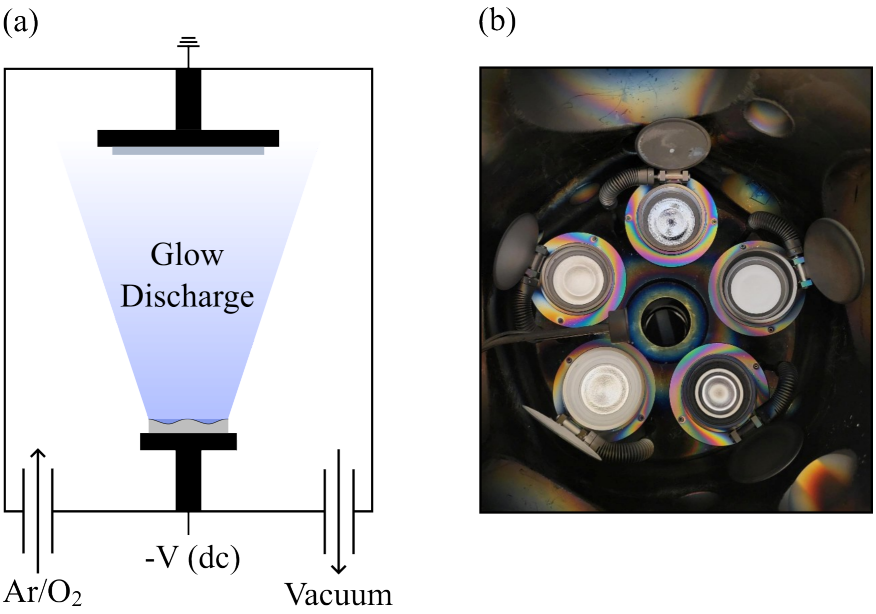


Fig. 3.1 Reactive sputtering setup used to deposit a-VO_2. (a) Schematic of the deposition chamber. Adapted from [209]. An inlet allows the controlled injection of argon and oxygen while an outlet connected to a turbo-pump allows to generate a controlled vacuum. A DC source is used to generate a plasma and the deposition plume, shown in blue. The vanadium target is visible at the bottom of the schematic while the wafer is held upside down at the top. (b) Picture of the inside of the deposition chamber. Five deposition guns holding five different targets of various materials are visible.

Sputtering

Stoichiometry calibration

Since the target used in this work is a 99.9 % pure V target from Neyco [212], reactive sputtering is required. A controlled amount of oxygen is injected in the reactor with the argon in order to oxidise the sputtered vanadium plume. However, many different vanadium oxides exist [217, 218] and only a specific window of deposition parameters allows to obtain stoichiometric VO_2 [219].

As reported in [220, 219], the most important parameter during the deposition is the amount of oxygen injected alongside the argon flow. Oxygen determines the oxidation state of the sputtered vanadium. As explained in [219], for a given set of deposition parameters (notably the sputtering power and chamber pressure), the amount of oxygen directly influences the stoichiometry of the deposited oxide as well as the sputtering rate. Indeed, too little or too much oxygen will lead to either under or over oxidation, leading to the deposition of the wrong vanadium oxide.

A calibration of the deposition is required to determine the amount of oxygen needed to get stoichiometric VO_2 [219]. A calibration procedure, based on a measurement of the relative sputtering rate as a function of the oxygen concentration, is performed for each new vanadium target used. This procedure must also be done at the half life of the target since the calibration curve tends to shift as the target ages. If not taken into account, this shift ultimately leads to the production of the wrong vanadium oxide [219].

The calibration in itself consist in a measurement of the poisoning [221, 222] of the target, as in [219]. It is done as follows:

- **New crystal installation:** For each calibration, the sputtering chamber is vented and a new oscillator crystal is put inside of the sputtering rate measurement unit. The measurement of the sputtering rate is done by measuring the deviation of the oscillation frequency of the crystal compared to its resonance one [223, 224]. As sputtering occurs, material gets deposited on the crystal. This changes its mass and in turn shifts its oscillation frequency. In certain scenario, like thermal evaporation of known metals or compounds, this method is used to get measurements of the deposition rate [223, 224].

The absolute measurement of the rate requires knowledge of the material density as well as fitting parameters that depend on the chamber parameters. In the case of the calibration, the amount of oxygen is swept and different oxides get deposited. Since the different compounds feature different densities, an absolute measurement of the rate is not possible. This is why the results from Fig. 3.2 are normalised.

- **Cleaning:** The vanadium target is cleaned by an argon plasma for five minutes. This is to remove contaminants or native oxide from the new target or remaining oxides from previous depositions in the case of a mid life target. The cleaning is done under a closed shutter for five minutes in a chamber pumped at 5 mTorr, with a 200 W pure argon plasma.

- **Target poisoning:** The shutter is opened and the calibration starts with an oxygen/argon ratio of zero percent (0/50 sccm/sccm of O_2/Ar). The DC source is set in power control mode to let the IV parameters of the plasma floating. The oxygen amount is increased by steps of 2 % up to 24 %. A three minutes stabilisation period is left between two increases of the oxygen amount to let the target reach a steady oxidation regime which in turns leads to a plasma with stable I and V parameters. After the three minutes, the plasma parameters (voltage, current, power) are logged along with the relative sputtering rate. As can be seen in the Fig. 3.2, the sputtering rate decreases quickly as the amount of oxygen increases. This is due to the over oxidation of the vanadium target which becomes insulating and renders the DC sputtering ineffective. This phenomenon is called *poisoning* [221, 214, 213, 222].

- **Range identification:** Fig. 3.2 shows the calibration curve obtained in the *AJA Instrument* [205] sputterer for a new pure vanadium target. Its profile is as expected from [219]. The curve features a sharp increase of the sputtering rate between 0 % and 2 % of oxygen before slowly decreasing to a fully poisoned state at 24 %. The obtained result is compared with [219] which allows us to identify a range of oxygen which should give stoichiometric VO_2. For the considered calibration, the range is illustrated in green in Fig. 3.2 and sits between 5 % and 14 % of oxygen.

- **Range validation:** Once the range is identified, amorphous VO_2 is deposited, on different samples and at different oxygen concentrations located within the range. The sample are then annealed at the same time and under the same conditions. This part is discussed in the next section. This step is critical as it allows to produce samples to be checked by scanning electron microscopy (SEM) and Raman spectroscopy to validate the stoichiometry [217, 218] and topological [225, 226, 152] parameters of the final p-VO_2 thin film.

- **Plasma parameters:** After the SEM and Raman inspection of the samples, an oxygen set point is selected. In order to fix the parameters, the current at which the plasma settled while in power control mode must be used for subsequent depositions.

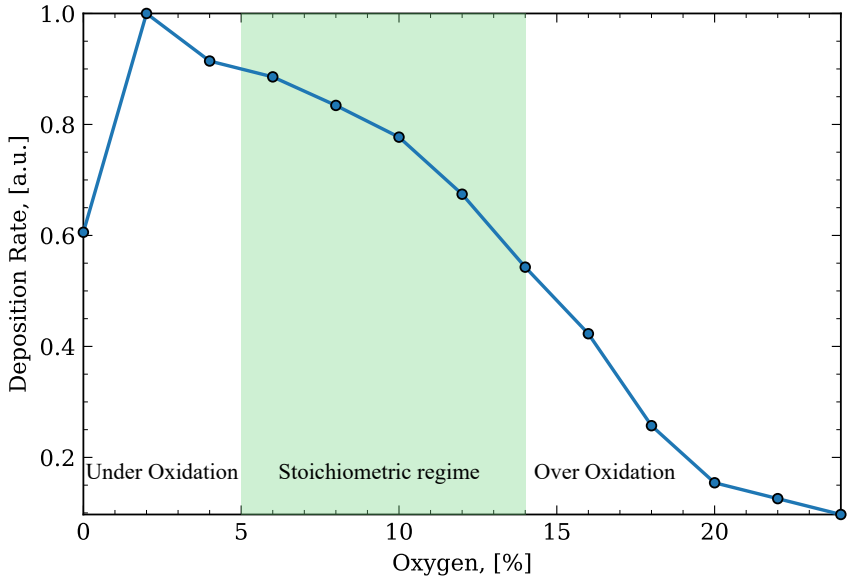


Fig. 3.2 Calibration curve of the reactive sputtering of a V target in reactor from *AJA international*. The relative sputtering rate is measured at different ratios of oxygen ranging from 0 % to 24 % . Experimental measurement is shown by a plain blue line with dots. The green area represents the range in which the reactor produces stoichiometric a-VO_2.

Deposition protocol

A typical deposition can be done following the given protocol. This deposition protocol is adapted from [199, 200, 201, 202, 154]:

- **Cleaning:** First, the vanadium target is cleaned by a pure argon plasma. A shutter, located right above the deposition target is closed to prevent deposition of species on the sample. All shutters can be seen open in Fig. 3.1(b). This step is used to remove potential contaminants or residual V_xO_y phases that might have formed on the surface of the target during previous reactor operation. This step takes place under a vacuum of 5 mTorr, a 200 W plasma, an injection of 50 sccm of argon and 0 sccm of oxygen for a duration of five minutes.

- **Oxidation:** To do so, a precise amount of oxygen is added to the argon flow. This amount must be calibrated by prior testing and by measurement of the calibration curve of the vanadium target. This step takes place under a vacuum of 5 mTorr and a 200 W plasma. A typical ratio of gas is 43.5 sccm of argon and 6.5 sccm of oxygen. The oxidation is done for a duration of three minutes in order to bring the target to a steady state regime prior to the deposition step to avoid evolution of the stoichiometry after the shutter is opened. This duration was previously established in the lab and not challenged in this work [203].

- **Deposition:** The shutter is opened to allow the deposition plume to reach the sample. The deposited material is stoichiometric, amorphous VO_2 if proper oxidation of the target surface was achieved. The deposition parameters are the same as the ones of the oxidation step. A typical sputtering rate between 6 and 12 nm/min is achieved, depending on the age of the target. The actual sputtering rate is measured after the deposition by inspection of the wafer cross section in an SEM.

Annealing

At this stage, the deposited layer is in an amorphous state since the deposition is done at room temperature. No crystal growth happens during the deposition as opposed to some setups where the sample is kept at high-temperature such as in [148, 227, 149].

In this work, the samples is be thermally annealed in order to go from an amorphous state to a polycrystalline one [154, 199, 200, 202, 225]. The annealing takes place in a tubular furnace put under a 2.01 x 10^{-1} hPa vacuum and with an argon flow of 30 sccm. This is done to ensure that no further oxidation occurs during the annealing since the stoichiometry is fixed by the sputtering step. During annealing, only the crystallites size can be tuned by changing the temperature [152, 154, 225, 226].

The annealing in itself follows a thirty minutes ramp up to the desired temperature. The furnace is held for one hour at the nominal temperature to allow for the spontaneous growth of the VO_2 crystals. The annealing temperature sits in the range of 450°C to 650°C, depending on the desired crystal growth.

Temperature impact

The annealing temperature is the most important parameter in the control of the crystallite size in a polycrystalline VO_2 thin film. Indeed, as explained in [152, 154, 225, 226], the grain size in the final thin film increases with the increase in temperature. Control of the grain size is critical as it greatly impacts the electrical and phase transition properties of the material. This is well established in literature [153, 154, 226, 228] but lies beyond the scope of this work.

Fig. 3.3 illustrates the increase of the grain size with increasing temperature. Three thin films are deposited at 12 % of oxygen and subsequently annealed at 550°C, 600°C and 650°C. The increase in the grain size is visible in both the top and cross view of the thin films pictured by SEM.

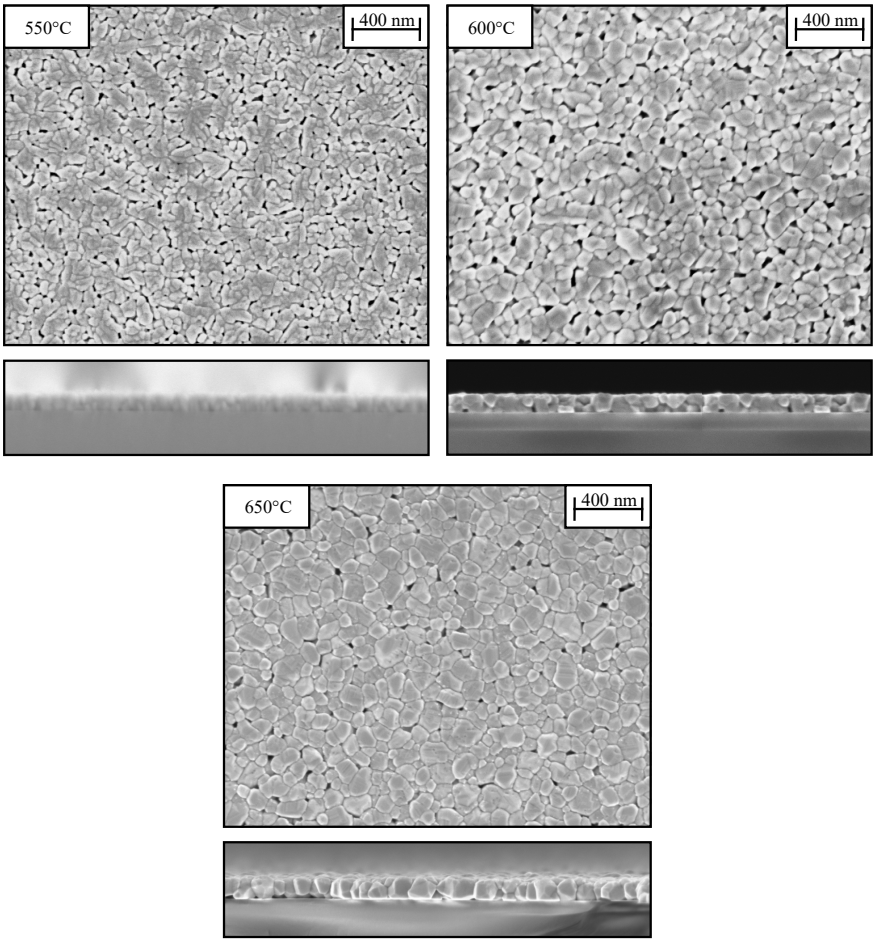


Fig. 3.3 SEM micrographs showing the impact of the annealing temperature on the grain size of p-VO_2. Films annealed at 550°C, 600°C and 650°C for one hour are shown. A cross section, at the same scale, is shown beneath the main micrograph for each annealing temperature.

Oxygen impact

Apart from being the most important parameter to obtain stoichiometric vanadium dioxide [220, 219], the amount of oxygen also plays a role in the final size of the crystallites. This result was established in [203, 229] and reproduced in Fig. 3.4. Six different thin films are deposited with concentrations of oxygen between 6 % and 16 %. All other deposition parameters are kept the same (5 mTorr, 200 W plasma and 13 minutes of deposition) and the samples are annealed at the same time at 650°C four one hour under an argon flow.

Fig. 3.5 shows the Raman spectra of the considered thin film. The top plot represents the spectra of the films deposited between 6 % and 14 % of oxygen. All of them correspond to the Raman signature of stoichiometric VO_2, according to [217, 218] This means that, in the range identified during the calibration process, all ratios of oxygen yield stoichiometric vanadium dioxide thin film. The amount of oxygen does however impact the final grain size with grain size between 20 and 50 nm for the thin film deposited at 6 % of oxygen and between 200 and 400 nm for the thin film deposited at 14 % of oxygen. This means that controlling of the oxygen amount provides another lever of control on the final film topology, in addition with the annealing temperature [203, 229].

Further increase of the oxygen amount yields the production of an over oxidised vanadium oxide. The thin film deposited at 16 % can be seen in Fig. 3.4 and its corresponding Raman spectrum is provided in Fig. 3.5(b). Reading [218], the high-intensity peak located before 150 cm^{-1} is a sign of over oxidation and can be linked to the production of parts of V_6O_{13} or V_2O_5 along with the VO_2

Raman spectroscopy does not provide a quantitative characterization of the crystallised thin-film but only allows to identify the dominating stoichiometry. X-ray diffraction (XRD) is used to characterise VO_2 thin-film [218] as it allows to recover the composition, dominant crystallographic orientation and phases in the thin-film [230]. In this work, this step was skipped as the focus was on device integration rather than process optimisation. This was done on the basis of previous published work of the lab that established XRD characterizations of p-VO_2 thin-films deposited using the same techniques, equipments and parameters as in this work [203, 154].

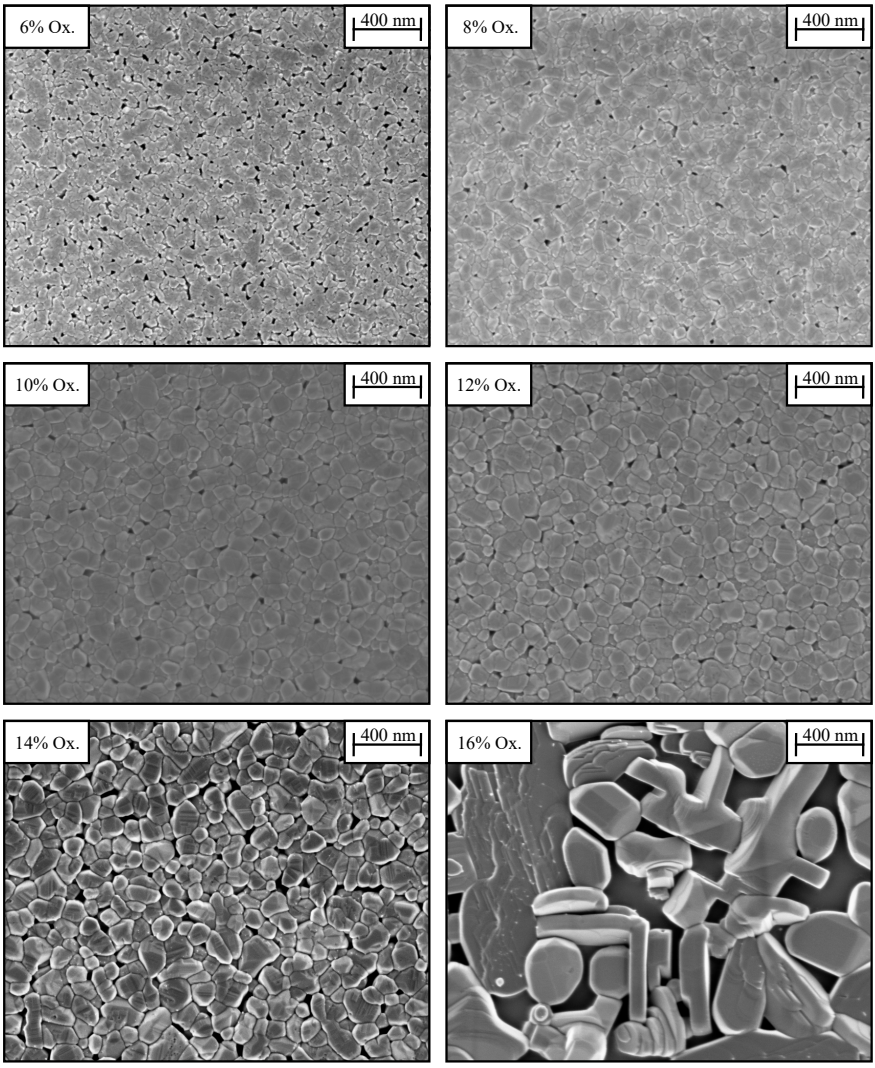


Fig. 3.4 SEM micrographs of p-VO_2 and p-V_xO_y thin films deposited by reactive sputtering with different amounts of oxygen. All films were annealed at 650°C for an hour and at once. Films deposited at 6, 8, 10, 12, 14 and 16 % of oxygen are shown. All films are p-VO_2 except the one deposited at 16 % of oxygen.

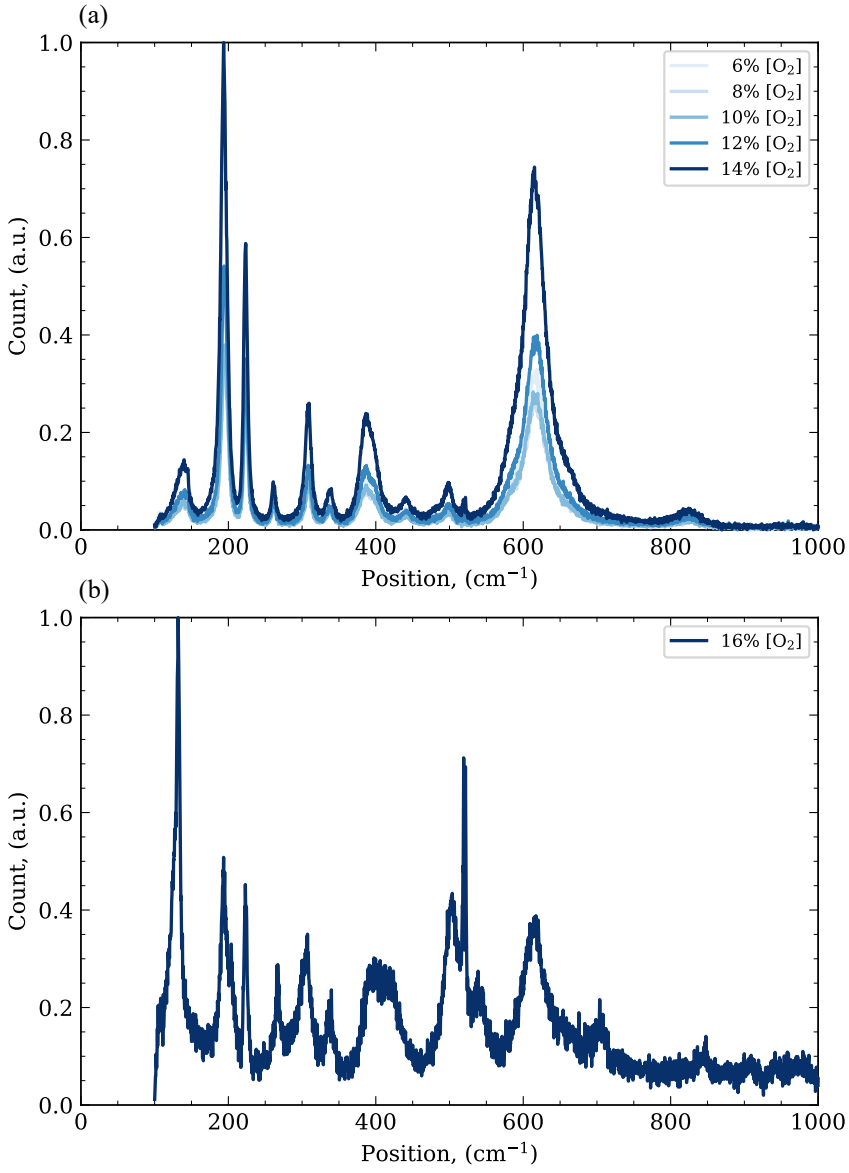


Fig. 3.5 Raman spectrum of p-VO_2 thin films deposited by reactive sputtering with different amounts of oxygen. All films are annealed at 650°C for an hour and at once. (a) Raman spectra of p-VO_2 thin films deposited at 6, 8, 10, 12 and 14 % of [O_2] in the oxygen/argon mix. (b) Raman spectrum of a p-V_xO_y compound deposited at 16 % of [O_2] in the oxygen/argon mix.

RT validation

An additional characterization is to check the transition properties of the material. While the metal-to-insulator transition (MIT) is not the topic of this thesis, it serves as a good indicator whether or not the deposited layer behaves as expected. When heated, the electrical resistance of the material is expected to slowly decrease up to a transition temperature around 70°C [112, 113, 114]. At this temperature, the crystal undergoes a structural phase transition (SPT) from its M1 state to its metallic R one [231, 232, 233]. A resistance variation between one and five orders of magnitudes (OOM) is expected [113], depending on the sizes of the crystallites in the p-VO_2 thin film [234, 235, 236].

When cooled, VO_2 transitions back to its semiconducting state at a lower temperature than the one of the heating sweep [114]. This defines the transition window of the well-known hysteresis of the vanadium dioxide transition [112].

The observation of the resistance/temperature (RT) curve of VO_2 and the measurement of the transition temperature, resistive ratio between the low- and high-resistivity states and the hysteresis window provide good indications on the quality of the as-deposited layer [113].

Fig. 3.6 shows the RT profile of a 130 nm-thick vanadium dioxide layer deposited at 13 % of oxygen in the gas mixture and annealed at 500°C. The transition features a two order of magnitude resistive switch and a MIT temperature of 71°C. The hysteresis window is of 11°C. All those values are well in line with the literature for similar thin films [148, 149].

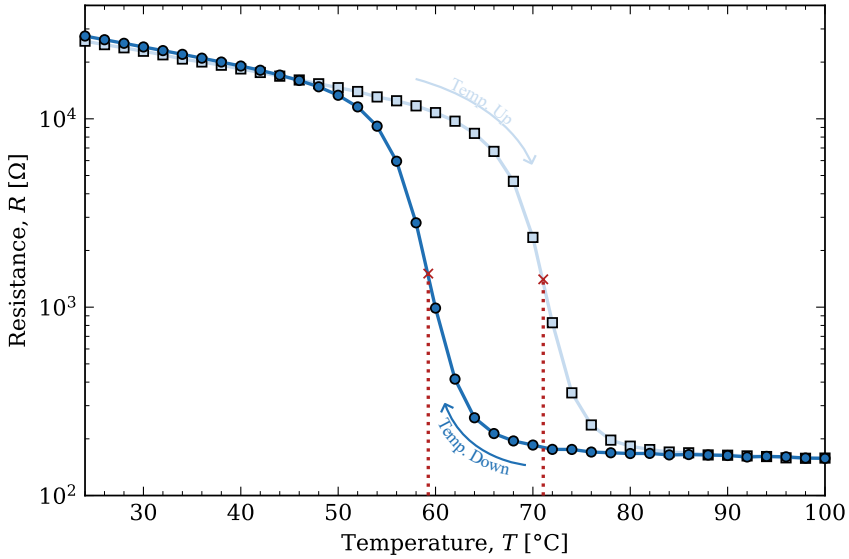


Fig. 3.6 Typical profile of the electrical resistance variation of a p-VO_2 resistor as a function of the temperature. A different path is followed for increasing and decreasing temperature, forming an hysteresis. The measurement is performed in a climatic chamber using a four probes setup for a 130 nm-thick layer of vanadium dioxide deposited at 13 % of oxygen and annealed at 500°C.

3.2 p-VO_2 blanket on polyimide membrane

Motivation

The integration of a vanadium dioxide blanket layer onto a large polyimide membrane is illustrated in Fig. 3.7. The motivation behind the integration of an unpatterned thin-film of the material onto a membrane is two-folds:

- **Adhesion testing:** Before trying to integrate devices via a complete and more complicated fabrication process, the proper adhesion between the PI layer and the p-VO_2 must be verified.

- **Recovery of the Young's modulus of p-VO_2:** In order for the *Comsol* FEM model to properly compute the local strain in p-VO_2 devices built on a polyimide membrane, the exact Young's modulus of the material must be known. The fabricated samples are used to estimate the Young's modulus of the film to solve the high uncertainty reported in the literature. Indeed, a wide range of modulus, from 86 to 170 GPa, are given in the literature due to the important impact of process parameters on film topology [160, 161, 162].

Process

Fig. 3.7 shows the process used to integrate a thermally annealed p-VO_2 blanket layer on a 2.5 mm-wide and 3.2 µm-thick polyimide membrane. The process starts in Fig. 3.7(a) with a 380 µm-thick thermally oxidised bulk silicon wafer. The bottom layer of thermal silicon dioxide is removed by a BHF wet etch. The remaining top layer of silicon dioxide is measured to be 220 nm-thick by ellipsometry.

A 220 nm-thick layer of a-VO_2 is deposited by reactive sputtering in Fig. 3.7(b) following previously established recipe from the Winfab facility of the UCLouvain [154, 203, 204]. The deposition is made in a sputtering chamber from *AJA Instrument* using a 99.9 % pure vanadium target from Neyco [212]. The chamber is held at a pressure of 5 mTorr under an argon flow of 43.5 sccm and an oxygen flow of 6.5 sccm. The plasma is stabilised at 200 W in a current control mode set at 450 mA. The a-VO_2 layer is crystallised to obtain a p-VO_2 blanket layer by a 550°C thermal annealing. The wafer is placed under a 2.01 x 10^{-1} hPa vacuum with a 30 sccm argon flow to prevent re-oxidation of the VO_2 layer. A 30 minutes ramp is used to get to a final temperature of 550°C maintained for an hour. After annealing, the deposited layer is confirmed to be p-VO_2 by both SEM microscopy and Raman spectrometry [217, 218].

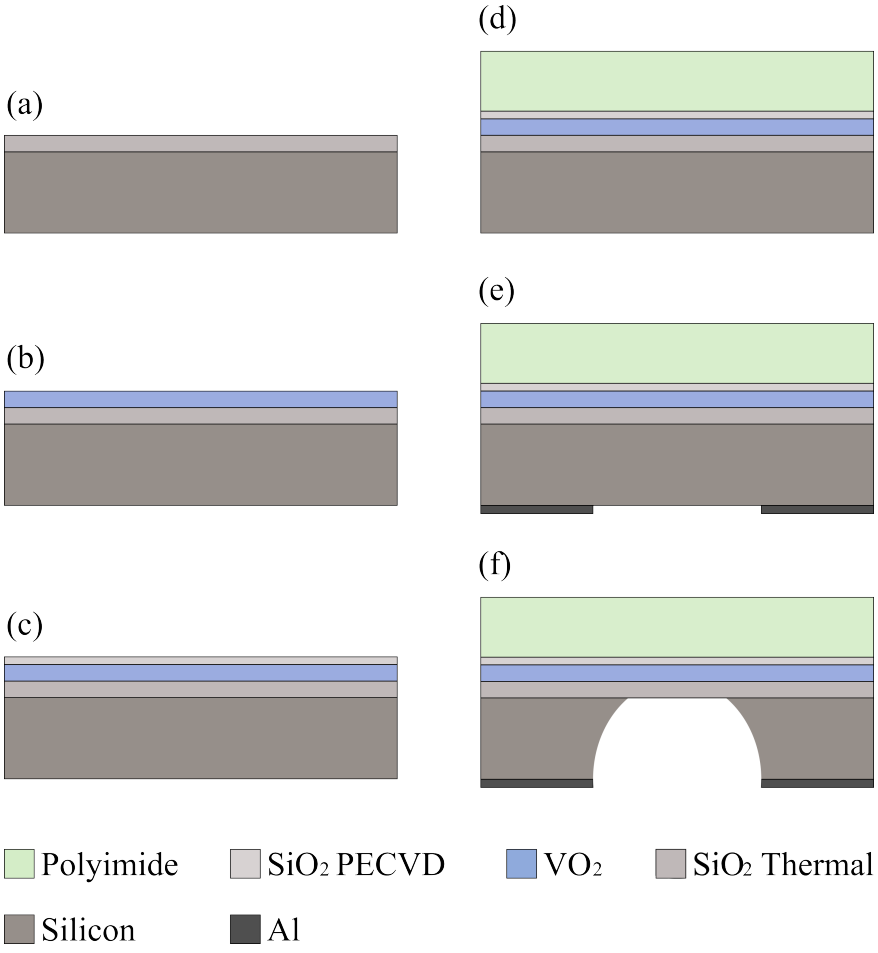


Fig. 3.7 Process flow schematics: Summary of the fabrication process to integrate p-VO_2 thin films on a free standing, 2.5-mm wide, polyimide membrane. (a) Initial bulk silicon wafer with 220 nm of thermal SiO_2 on top. (b) Sputtering of a 220 nm-thick p-VO_2 layer. (c) Deposition of a 50 nm-thick SiO_2 adhesion layer via PECVD. (d) Spin coating of a 3.2 µm-thick layer of polyimide. (e) Backside definition of an Al hard-mask by thermal evaporation and wet etching. (f) Membrane release via XeF_2.

Preliminary testing showed poor adhesion of cured PI precursor on p-VO_2 with a systematic failure of the pull test [237]. To cope with this, a 50 nm-thick layer of silicon dioxide is deposited by PECVD in a reactor from

Oxford Instrument in Fig. 3.7(c). This thin SiO_2 layer acts as an adhesion promoter between the polyimide and the p-VO_2. This proves very effective with a systematic pass of the pull test across multiple samples. Silicon dioxide was chosen as adhesion promotion layer as in the two previous chapters.

As explained in chapter two, the excellent agreement between the Raman peak-shift measurement and Comsol simulation confirms the transfer of strain through the PI/SiO_2 interface without slippage. Additional comments on the proper adhesion between the polyimide layer and the silicon dioxide buffer layer are presented in the next chapter.

The polyimide layer is next integrated in Fig. 3.7(d). First, the wafer is primed using an adhesion promoter, VM652 from *HDMicrochemicals* [169]. PI2545 [168], the PI precursor from the same brand, is spun at 1800 RPM then cured at 350°C, under an argon flow, for one hour. The final layer thickness is measured to be of 3.2 µm-thick by ellipsometry. The higher rotation speed compared to the two first chapters was used to obtain a thinner layer of polyimide as preliminary testing for the next chapter. This is of interest since thinner polyimide leads to higher strain for the same amount of applied pressure.

The shape of the membranes is defined on the back side of the wafer by patterning an hard mask, as in Fig. 3.7(e). A 300 nm-thick layer of aluminium is deposited using a thermal evaporator from *VST*. Patterning of the aluminium is done via photolithography and a timed H_3PO_4/IPA wet etch at 60°C.

Finally, the membrane is released in Fig. 3.7(f). The release is done by an isotropic dry etch of the sample in XeF_2 using a reactor from *Xactix*. The final membrane is a 2.5 mm-diameter circular diaphragm.

Young's modulus recovery

In order to obtain a proper simulation of the local strain field induced in the p-VO_2, the mechanical properties of the material must be known. Among them all, its Young's modulus (E_{VO_2}) plays an important role as it directly links the amount of strain induced in the material to the applied force ($\sigma = E\epsilon$).

Looking in the literature, it quickly appears that the value of E_{VO_2} is strongly impacted by process variation and film topology. Table 3.1 summarises the different values of Young's modulus available for VO_2 in the literature. A wide range of values is presented, even if only looking at the polycrystalline thin-films. This search highlights the need for a proper estimation of the E_{p-VO_2} of our particular thin film. Indeed, depending on the selected value from the literature, an uncertainty of $e = \pm 25.3$ % might be introduced on the strain estimation computed by the *Comsol* FEM model ($e = \pm(86[GPa]/170[GPa]) * 50$, in percent and based on the min. and max. values from 3.1).

E [GPa]	Material Type	Deposition	Measurement	Source
140-170	p-VO_2 Thin film	Reactive Sputtering	Microindentation	[161]
86	p-VO_2 Thin film	Pulse laser Deposition	Cantilever oscillation	[160]
155	c-VO_2 Nanobeam	Vapor transport Epitaxy	Beam deflection AFM	[162]
120	p-VO_2 Thin film	Reactive Sputtering	Membrane deflection	**This work**

Table 3.1 Young's modulus of different types of VO_2 available in the literature.

To properly estimate the Young's modulus of the as-deposited thin-film, a bulge test is performed following a slightly modified routine of the one presented in the first two chapters of this work. This approach is well documented in the literature [238, 239, 240, 241]. The idea is to fit the deflection of a composite membrane stack with a pre-established model of the membrane.

For this to work, the structural material of the membrane must be fully characterised and the bulge of the membrane on its own must be perfectly modelled. By adding a material on top of it, the stiffness of the membrane increases and its bulge profile with pressure changes. This allows to recover mechanical parameters of the deposited thin-film, via fitting of the model. In this work, the proper modeling of the polymeric stack is already demonstrated in the first two chapters. The model is used to recover the Young's modulus of the as-deposited p-VO_2 layer. This technique is well suited for this work since we already have a fabricated PI membrane with a p-VO_2 thin film, the model of the blank membrane and the experimentation setup. It allows to measure the modulus without having to use more complex microindentation measurement, as in [161].

First, a die carrying a 2.5 mm-wide, 3.2 µm-thick polyimide membrane with a 220 nm-thick layer of p-VO_2 is mounted on the *bulge test* setup introduced in the second chapter of this work (Fig. 1.5). The die is glued on an 5 mm-thick aluminium plate which is mounted on a pressure vessel connected to a pressure generator from *Halstrup Walcher*, the *Kal-100* [173]. The pressure vessel is placed under a white light interferometer [174] to measure the displacement of the membrane as a function of the applied pressure.

A pressure cycle, with sweeps from 0 to 100 and 100 to 0 kPa, is applied to the membrane, inducing bulge. For each pressure step the membrane displacement is measured by the white light interferometer and the maximal displacement is recovered after levelling of the results. From the pressure cycle, only the down part is kept in order to obtain a result which is not impacted by plastic effects [188, 179].

Keeping this half of the measurement allows to fit the displacement of a *Comsol* model of the stack presented in Fig. 3.7(f) on the Young's modulus of the p-VO_2 thin film only. Indeed, in the up part of the cycle, the pressure/displacement curve is impacted by the plastic parameters of the *Swift* model, the Young's modulus of the p-VO_2 blanket and the dimensions and layer thickness of the as-fabricated sample. Since the only unknowns to be fitted by the *Comsol* model are the plastic parameters and the Young's modulus, keeping only the relaxation sweep from 100 to 0 kPa allows to get rid of all fitting parameters beside the Young's modulus.

The results of the experiment are visible in Fig. 3.8. Three different values of E_{p-VO_2} are simulated: 100, 120 and 140 GPa, as visible in Fig. 3.8(a) and shown in light to dark blue line with dots, respectively. The graph shows the simulated maximal displacement of the membrane as a function of the pressure for a pressure ranging from 100 to 0 kPa. The simulation is done considering no plastic effect. This hypothesis is made on the basis that the relaxation part of a stress/strain curve follows an elastic path [188]. A maximal deflection of 123 µm is reached at 100 kPa. As can be seen on the plot, the maximal deflection is impacted by the increase in the Young's modulus. As the modulus increases, the membrane becomes stiffer, which leads to lower general deflection.

Fig. 3.8(b) shows an overlay of both the result from the *Comsol* FEM model, in a dashed blue line, and the experimental results, in dark blue dots, from the bulge test. The simulation result is obtained by using a Young's modulus of the p-VO_2 of 120 GPa. An excellent agreement between the experimental result and the FEM model is obtained. Furthermore, the obtained Young's modulus, 120 GPa, falls well in the range obtained by the literature, as visible in 3.1. This result validates the approach adapted from the literature [238, 239, 240, 241]. This value of the Young's modulus of p-VO_2 is the one used in the rest of this work.

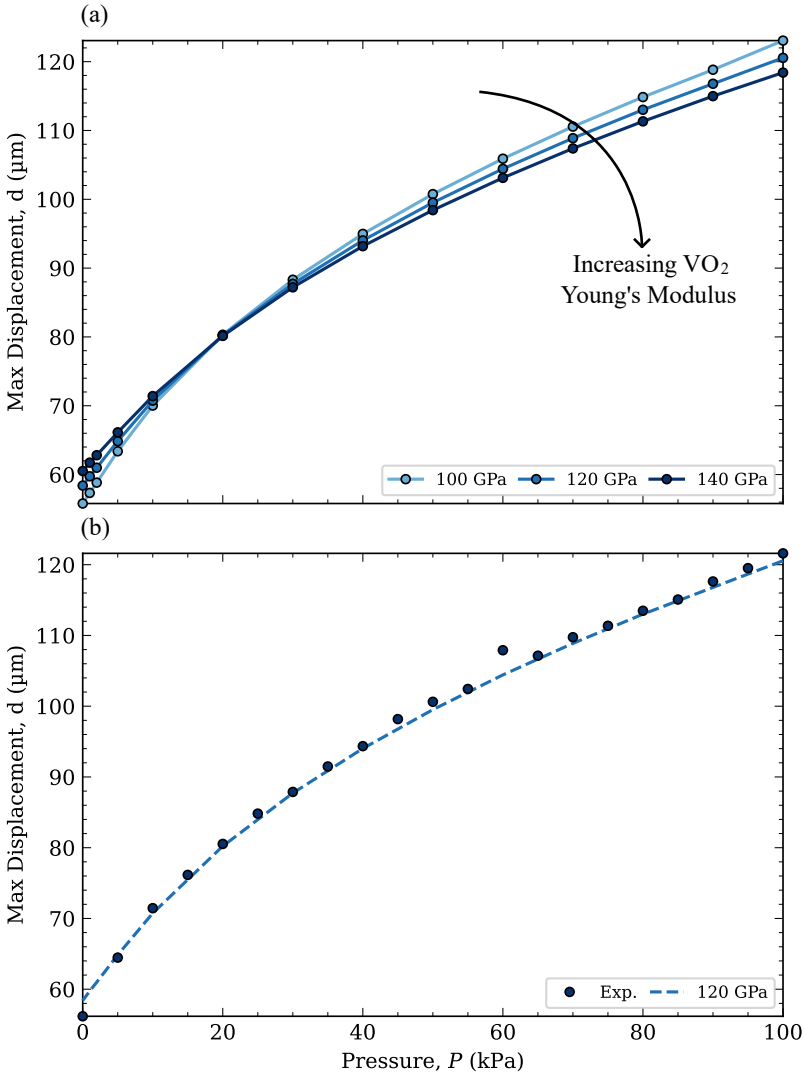


Fig. 3.8 Calibration of the *Comsol* model of a 2.5 mm-wide and 3.2 µm-thick p-VO_2/PI membrane: (a) Simulation results of the 2.5 mm-wide membrane under increasing pressure ranging from 100 to 0 kPa. Three different p-VO_2 Young's moduli are tested. Simulation results for E_{p-VO_2} of 100, 120 and 140 GPa are represented by plain light to dark blue lines with dots. (b) Calibrated *Comsol* Model using a Young's modulus of 120 GPa. The simulation results are shown by a dashed blue line while the experimental measurements are represented by dark blue dots

3.3 Conclusion

This chapter presents all the basics required to process p-VO_2 thin films on large polyimide membranes. The deposition parameters and protocols to obtain stoichiometric p-VO_2 are presented. The monolithic fabrication process to integrate microelectronics on a polyimide membrane is adapted to allow the integration of thermally annealed p-VO_2 in a monolithic way, without layer-transfer or thermal budget.

A 220 nm-thick VO_2 thin film is integrated on a 3.2 µm-thick and 2.5 mm-wide polyimide membrane. This sample serves as a first proof of concept of the feasibility of the integration of p-VO_2 onto polyimide using a monolithic fabrication process. This processes showed that p-VO_2 does not adhere properly to polyimide. This is solved by adding a 50 nm-thick layer of PECVD SiO_2 between the PI and the p-VO_2. It acts as an adhesion promotion layer and allows systematic pass of the pull adhesion test.

The fabricated membrane stack is next used to estimate the Young's modulus of the film to solve the high uncertainty reported in the literature [161, 160, 162]. This is done by performing a bulge test measurement of the stack [238, 239, 240, 241]. The polyimide membrane, made stiffer by the blanket layer of p-VO_2, features an altered maximal deflection profile with pressure. A Young's modulus value of 120 GPa for the as-deposited thin film is computed by fitting the simulation parameters of a *Comsol* model on the experimental data. This is in the reported literature range [238, 239, 240, 241].

3.4 Take home messages

- The integration of thermally annealed sputtered p-VO_2 on polyimide is demonstrated using a monolithic fabrication process. The technique requires the introduction of an SiO_2 adhesion layer to get the PI to stick to the p-VO_2.

- A Young's modulus of 120 GPa is computed for the as-deposited p-VO_2 by fitting a *Comsol* model on a bulge measurement of the membrane stack. This measurement is required to obtain a proper strain estimation in the next chapter.

4

p-VO_2 resistors: Impact of high-strain on the gauge factor

Now that the feasibility of the process has been demonstrated and that the effective modulus of the p-VO_2 has been recovered, the impact of high-strain on the gauge factor of the material can be studied.

As already established in the introduction of this work, vanadium dioxide benefits from an intrinsically high gauge factor. Previous work reports GFs varying from 175 to 150 for c-VO_2 nanobeams [117] and from 620 to 370 for epitaxial layers [121] subjected to 0.3 % of tensile strain. Those values are attributed to a partial transition of the crystal from an M1 to an intermediate M2 phase with strain [113, 114, 115, 116, 117, 118, 119, 120]. This partial reconfiguration is accompanied by an increase of resistance coming from the intrinsic difference in resistivity of both phases ($\rho_{M2} = 3 * \rho_{M1}$) [116, 117].

When looking into the use of VO_2 as strain sensor, the emerging trend is its integration on polymeric flexible substrates for high-strain sensing [117, 89, 121, 131, 132]. As detailed in the previous chapters, attempts were made either using low-crystallinity [145, 146, 140] VO_2 deposited at low-temperature [139, 140, 141, 142, 131, 143, 144] or using complex layer transfer [146, 89].

To the best of our knowledge, no study of the gauge factor of highly strained sputtered p-VO_2 has been made.

This chapter studies the potential of p-VO_2 devices fabricated by sputtering for high-strain sensing and tries to answer the following scientific question:

How does the gauge factor of patterned p-VO_2 fabricated via reactive sputtering and thermal annealing behave under high-strain?

To answer that question, this chapter tackles the following tasks:

- **p-VO_2 resistors on PI:** patterned p-VO_2 resistors are integrated on a 2.5 µm-thick and 1 mm-wide polyimide membrane using the developed monolithic fabrication process.
- **Bulge test:** The membrane is mounted on a *bulge test* setup. The membrane is inflated up to 100 kPa and the maximal deflection of the membrane is measured *in situ* using a white light interferometer. The variation of the electrical resistance of a p-VO_2 resistor is measured at the same time to get the resistance-pressure relation.
- **Strain computation:** The *Comsol* FEM model is adapted to the fabricated sample and fitted on the experimental measurement of the maximal deflection. The fitting of the model allows to recover the full strain field induced in the p-VO_2 device.
- **Gauge factor computation:** Using both the electrical resistance measurement and the strain field extracted from the FEM model, the gauge factor is computed and discussed.

4.1 p-VO_2 resistors on PI membrane

Design

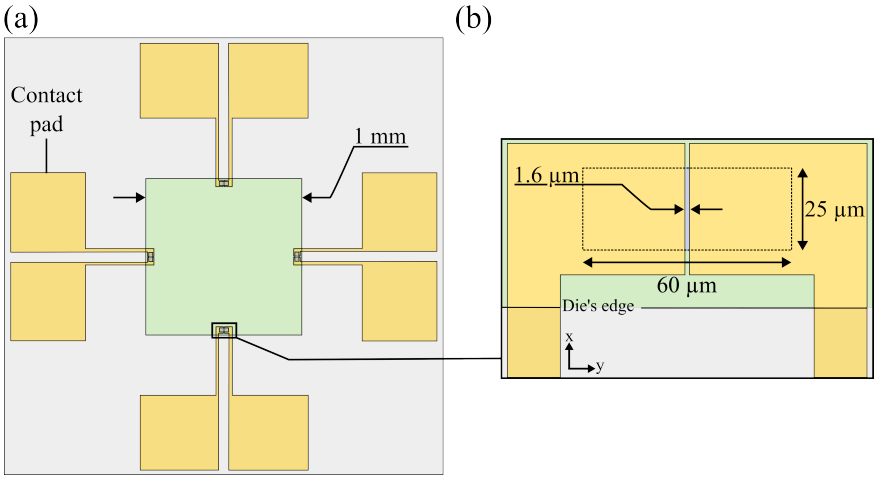


Fig. 4.1 Design schematics: (a) Layout showing a 3 x 3 mm^2 die featuring a 1 x 1 mm^2 square shaped membrane and a set of four electrically contacted p-VO_2 2T devices. The die is shown in light grey, the membrane in light green and the gold contacts in yellow. (b) Zoom on a p-VO_2 2T device. The 25 x 60 μm^2 patterned p-VO_2 patch is located underneath the gold contacts and shown by dashed lines. The channel between the gold contacts is 1.6 µm-long. The *xy*-coordinate system is represented as referential for the strain components.

Fig. 4.1(a) represents the layout used in this chapter. A 3 x 3 mm^2 die carries a 1 x 1 mm^2 square shaped membrane. Each membrane carries a set of four two-terminal (2T) p-VO_2 resistors. The devices are positioned alongside the edge of the membrane to maximise the amount of induced tensile strain [242, 166, 85]. Fig. 4.1(b) shows a zoom on a particular p-VO_2 device. Each resistor is made from a patterned 25 x 60 μm^2 p-VO_2 layer and contacted by two gold electrodes extending from the die onto the membrane. The length of the channel of the device is of 1.6 µm. A local *xy*-reference frame is defined as having the *x*-component perpendicular to the die's edge.

Design motivation

The design used in this last chapter is an updated version of the one used in the three previous chapters. The used set of masks was available at the UCLouvain Winfab facility from the previous work of [203, 154].

- **Membrane shape:** The shape is changed from circular to square to maximise the amount of tensile strain induced locally in the devices. Using square membranes compared to round ones is a common strategy which is well discussed in [242, 166, 85]. The use of a square membrane imposes the use of Bosch which allows for better control of the distance between the device and the designed membrane edge.
- **Electrical connection:** The electrical connections are simple overlaps. In the two first chapters, fingers like contacts were used. Those were fragile and prone to breaking.
- **Membrane dimensions:** Preliminary *Comsol* modeling showed that going from a 2.5 mm-wide and 3.6 µm-thick membrane to a 1 mm-wide and 2.5 µm-thick membrane does not result in a substantial drop in the local strain in the device of interest. This is further discussed when the strain results are presented. This choice is made because working with smaller membranes reduces the risk of rupture during the bulge test or release while increasing the population density of dies on the wafer compared to the 2.5 mm-wide ones.

Process

The integration of p-VO_2 resistors on a polyimide (PI) membrane is illustrated in Fig. 4.2. The process, based on [179], follows a monolithic approach. Fabrication starts with a 380 µm-thick bulk silicon wafer with a (100) top plane. A 104 nm-thick thermal silicon dioxide layer is grown on the wafer to allow recrystallisation of the sputtered amorphous VO_2 (a-VO_2) layer [148]. A three-minute BHF wet-etch is performed to remove the backside SiO_2 layer (Fig. 4.2(a)).

a-VO_2 is deposited by reactive sputtering using a deposition chamber from *AJA Sputtering System*. A 99.9 % pure vanadium target from *Neyco* [212] is used and the sputtering is performed using a 200W argon plasma.

The deposition parameters selected from this study come from previously published work from the Winfab facility of the UCLouvain [154, 203, 204].

Proper stoichiometry is achieved by injecting oxygen into the plasma as described in [219]. A gas mixture of 6.5 sccm of O_2 and 43.5 sccm of argon is used and a pressure of 5 mTorr is maintained as prescribed by [154]. The as-deposited a-VO_2 layer is recrystallised by thermal annealing. A ramp of 30 minutes is used to get to a final temperature of 550°C maintained for one hour. The annealing takes place under a vacuum of 2.01 x 10^{-1} hPa with an argon flow of 30 sccm to prevent further oxidation of the vanadium oxide. Once completed, the thickness of the layer is measured by profilometry and SEM inspection to be 110 nm. The size of the p-VO_2 crystallites, or grains, is measured to be between 150 and 200 nm in width, by SEM inspection. The stoichiometry of the annealed layer is checked by Raman spectroscopy by comparing the peaks of the obtained Raman spectrum with the ones of [217, 218]. XRD characterization of p-VO_2 thin-film deposited using the same equipments and process parameters was performed previously in the lab and presented in [154, 203, 204].

Patterning of the p-VO_2 layer is done by photolithography and RIE using a chamber from *Oxford instrument* (Fig. 4.2(b)). A 30W SF_6 (150 sccm) plasma is used with a table temperature and chamber pressure set at -5°C and 10 mTorrs, respectively. This process yielded a p-VO_2 etch rate of more than 50 nm/min with a selectivity of 2:1 compared to thermal SiO_2.

Metallisation is shown in Fig. 4.2(c). A 20/200 nm-thick stack of Cr/Au is deposited using a *Vacotec* thermal evaporator. Gold is used as the main conductor and chromium as adhesion layer. The Cr/Au stack is patterned by photolithography and subsequent lift-off using dimethylsulfoxide (DMSO). A backside metallisation is done to define an hard mask for use during the membrane release. A BHF rinse of the backside is first performed to remove the native SiO_2 layer and then a 300 nm-thick layer of Al is deposited using an evaporator from *VST*. Patterning is done by wet etching of the layer using an H_3PO_4/IPA solution kept at 60°C.

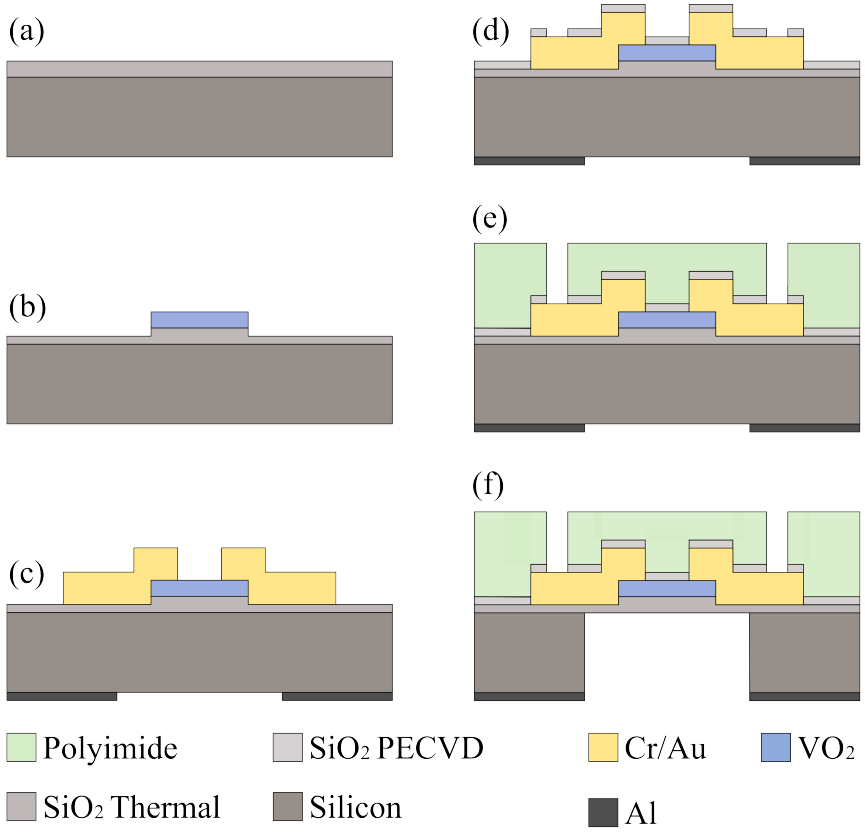


Fig. 4.2 Process flow schematics: Summary of the fabrication process to integrate p-VO_2 resistors on a free standing, 1-mm wide, polyimide membrane. (a) Initial bulk silicon wafer with 104 nm of thermal SiO_2 on top. (b) Sputtering and RIE patterning of a 110 nm-thick p-VO_2 layer. (c) Deposition and patterning of 20/200 nm-thick Cr/Au electrical contacts by thermal evaporation and lift-off. Backside definition of an Al hard-mask by thermal evaporation and wet etching. (d) Deposition and patterning of a 50 nm-thick SiO_2 adhesion layer via PECVD and RIE. (e) Spin coating of a 2.5 µm-thick layer of polyimide and contact opening by wet etching of the precursor. (f) Membrane release via Bosch process.

The 50 nm-thick SiO_2 adhesion layer is deposited by PECVD using a chamber from *Oxford instrument*, as shown in Fig. 4.2(d). The layer is patterned to define contact pads opening. Patterning is done by RIE in a chamber from *Oxford instrument*. A 30W SF_6 (150 sccm) plasma is used with the table temperature and pressure set to -5°C and 10 mTorrs, respectively.

As in [179], polyimide is used as flexible substrate as shown in Fig. 4.2(e). Integration is done by spin coating a precursor, PI2545, from *HDMicrosystems* [168]. The wafer is prepared by degazing it overnight at 120°C under an argon flow. An adhesion promoter, VM652 [169] is applied to prime the surface prior to the dispense of the PI precursor. PI2545 is spin coated at 1800 RPM and patterned via a development transfer method, described in [168], during a conventional photolithography.

The layer is cured at 350°C for one hour under an argon flow. The final thickness of the polyimide is measured by ellipsometry to be of 2.5 µm. The 700 nm difference in thickness compared to the one of the previous chapter, despite the same spin coating speed, comes from the replacement of the PI precursor bottle used in the study. The one used in the three first chapters had long passed it's expiration date. While not affecting the performance of the cured material, it significantly altered the viscosity of the precursor due to the evaporation of the solvent. For this chapter, a fresh bottle of PI2545 was obtained.

The membrane is finally released by a Bosch process using a plasma reactor from *Oxford instrument*. 290 cycles, etching 1.3 µm of silicon per cycle, are used to etch through the bulk silicon substrate and reach the bottom SiO_2 layer. A 1000/30 W of ICP/RF with a 50/140 sccm SF_6/C_4F_8 mixing ratio and pulses of 14/12 seconds for etching/depositing recipe is used. The final stack is shown in Fig. 4.2(f) and process results can be seen in Fig. 4.3.

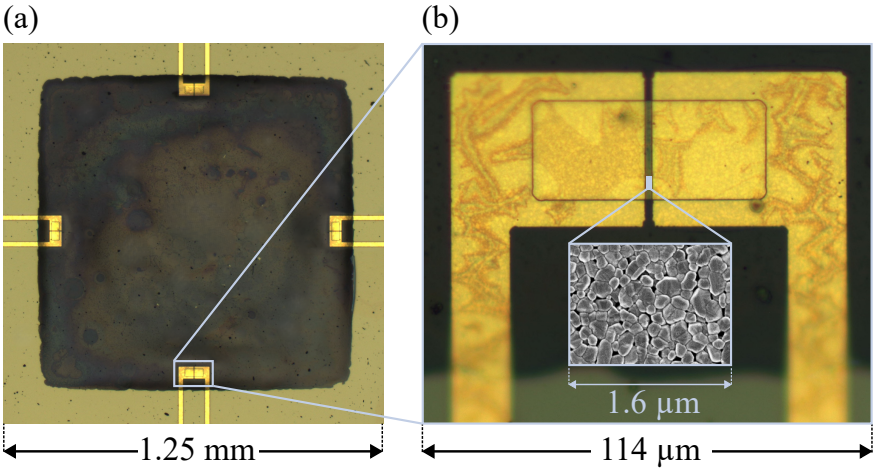


Fig. 4.3 Process results: (a) Microscopic image of a 1 mm-wide, 2.5 µm-thick polyimide membrane carrying a set of four p-VO_2 resistors alongside its edges. (b) Zoom on a particular p-VO_2 resistor. The inset shows an SEM micrograph of the as-produced p-VO_2 thin film.

4.2 Experimental setup

The goal of this experiment is to measure the IV characteristics of the p-VO_2 resistors under different levels of strain to extract the resistance variation and measure the gauge factor (GF) as a function of the strain. To do so, the compact bulge test setup introduced in the second chapter is used. The setup is represented in Fig. 1.5(a). The die carrying the membrane is glued on a 5 mm-thick aluminium plate using M-bond 200 [172]. The aluminium plate is mounted on a pressure vessel connected to a pressure generator from *Halstrup Walcher*. Their *kal-100* is used to apply pressures from 0 to 100 kPa to the membrane with an accuracy of 0.05 % [173]. The setup is shown in Fig. 1.5(b). The measurements of the device are carried out at room temperature under a white light interferometer from *Polytec* that allows to measure the exact deflection profile of the pressurised membrane[174]. Probes are brought under the interferometer's lens to electrically contact the devices. The IV measurement is performed by a 4145B semiconductor parameter analyser from *HP* [243]. An automation software is used to control all three pieces of equipment at the same time. After each pressure step, the

membrane's profile is measured. The interferometer beam is next turned off to allow the IV measurement to be carried out in the dark. This is done to rule out any potential photogeneration effect.

Three pressure cycles are carried out at successively higher maximal pressure. The first cycle is made in the [0-30] kPa range, the second in the [0-60] kPa range and the third one in the [0-100] kPa range. A cycle is defined by the measurement of the devices IV curve and membrane deflection profile for both the pressure up and down sweeps.

As established in the previous chapters, measuring the actual deflection profile is critical due to the construction differences between our PI membranes and classical oxide based ones used in literature. With conventional MEMS membranes, a valid hypothesis is to consider the generated strain field along the edge of the membrane as solely uniaxial toward the center of the membrane [155, 157]. This is not the case for polymer based membrane [179]. The measurement of the membrane maximal displacement allows to fit the *Comsol* model to recover the pressure-strain relation locally in the p-VO_2 devices.

Comsol Setup

The model is adapted to the particular design of the sample used for this experiment. Actual thickness measurements of the stack and other dimensions of the membrane and devices are utilised as input parameters for the model. Fig. 4.4(a) shows the full 3D model. The bulk silicon is removed compared to the model used in the two first chapters and is replaced by a *no displacement* constraint at the interface. The size of the membrane was measured to be of 1.05 mm in width instead of the designed 1 mm due to a lateral over etch during the Bosch process. A quarter of the membrane and only one device are simulated to reduce computational cost.

Fig. 4.4(b) represents the stack used in the experiment. Compared to the first two chapters, the exact stack is implemented into the model. This was made possible by the acquisition of new CPU cores.

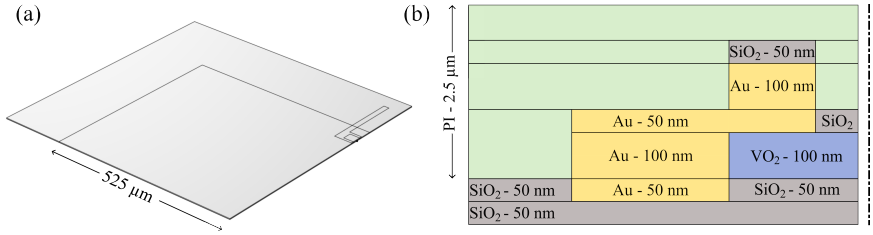


Fig. 4.4 Comsol model of the 2.7 mm-wide and 3.6 µm-thick polyimide membrane: (a) Overview of the complete model. A quarter of the membrane is simulated to reduce computation time. (b) Zoom on the c-Si devices and aluminium lines. (c) Stack simulated in the model. The thermal and PECVD SiO_2 are simulated as a single continuous layer and shown in gray. The aluminium is in black, the c-Si in blue and the polyimide in green.

Young's moduli are set to 87, 2.7 and 120 GPa for SiO_2, PI and p-VO_2, respectively [185, 168, 182]. Fitting parameters for the *Swift* model were calibrated on the experimental results presented in the next section and according to the procedure described in the second chapter of this work. They were found to be of 280 MPa and 0.2 [-] for the effective yield stress and hardening exponent of the stack, respectively.

4.3 Deflection Results

Fig. 4.5 shows both the experimental and theoretical results for progressive bulging of a 1 mm-wide, 2.5 µm-thick polyimide membrane for the three successively higher pressure ranges. This is done to study the effect of increasing maximal strain on the forward and backward resistance variation path. The top panel of Fig. 4.5 contains an inset showing a subset of levelled raw deflection profiles measured by the white light interferometer. Three profiles are displayed and are measured at 10, 20 and 30 kPa. Experimental data points are displayed as green dots and a least-square error approximation of a second-order polynomial is shown in dashed green lines. Once levelled, the maximal displacement is measured for each pressure set point by taking the maximum of the corresponding deflection profile.

The maxima are displayed as a function of the pressure as light blue squares and dark blue dots for the pressure up and down sweeps of each cycle, respectively. The *Comsol* results are displayed as light and dark blue lines for increasing and decreasing pressures.

In Fig. 4.5, the top panel shows the first pressurisation of the membrane from 0 to 30 and then 30 to 0 kPa. Upon pressurisation, the membrane starts to bulge and follows a non-linear cubic trend as described by large deflection models [178, 177]. A maximal deflection of 47 µm is reached at 30 kPa. When the pressure decreases, the membrane starts to deflate but follows a different path. This is expected, from [179], and indicates that the membrane entered in a plastic deformation regime during the initial pressurisation. When the load is progressively removed, the membrane deflates from a deformed shape and reaches a permanently deformed state of 6.9 µm of deflection at zero pressure. This relaxation behaviour is expected from plastically deformed material and applies well in this case [188]. This phenomenon, which fails to be taken into account in models such as [178, 177] is well captured by the *Comsol* model. An excellent agreement in both the followed trend and the absolute values is obtained. The red cross (x) and plus (+) are used to indicate the corresponding data point between consecutive cycles. The pressure cycles are made back-to-back on the same membrane. Hence, the membrane starts its second pressurisation from the previously deformed state. This is captured as well by the *Comsol* model.

The second and third pressure cycles are shown in the central and bottom panels of Fig. 4.5 and span between 0 to 60 and 0 to 100 kPa, respectively. Maximal deformations of 61 and 76 µm are reached at 60 and 100 kPa, respectively. As for the first cycle, the up and down sweeps of the pressure cycle do not follow the same path. The permanent deformation is more significant due to the higher applied pressure.

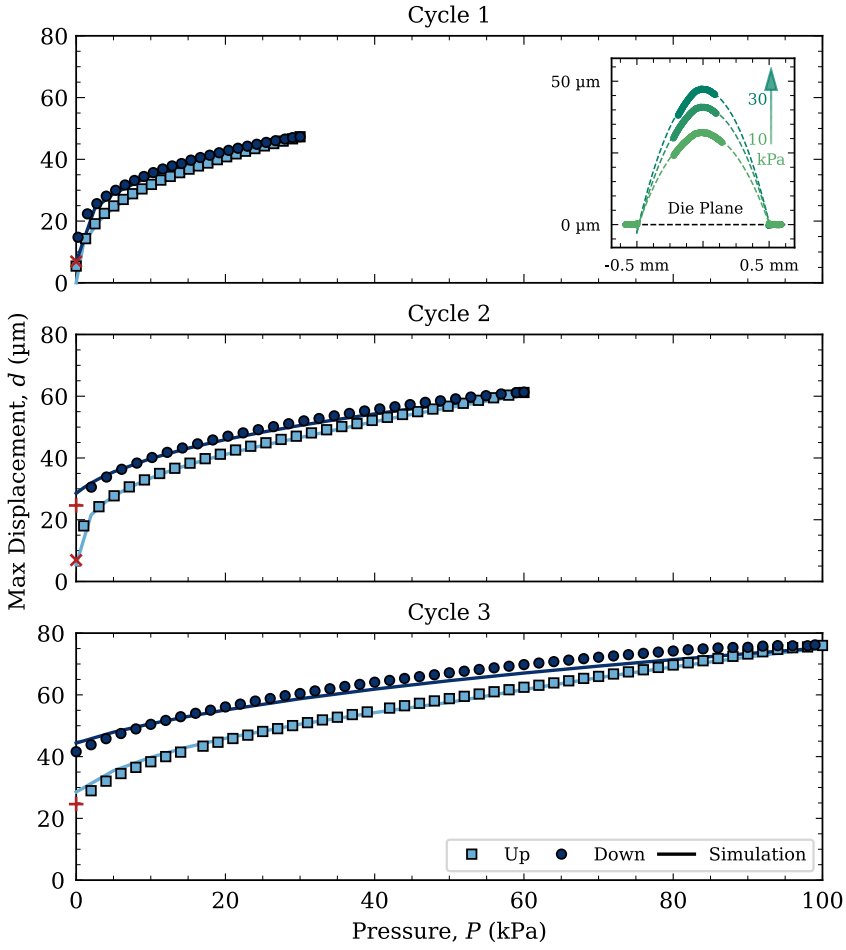


Fig. 4.5 Displacement results of a 1 mm-wide, 2.5 µm-thick polyimide membrane under pressure. Three successive pressure cycles are made on the same membrane and are displayed as Cycle 1, 2 and 3 ranging from 0 to 30, 0 to 60 and 0 to 100 kPa, respectively. Experimental results are displayed as light blue squares and dark blue dots for pressure up and down sweeps. Theoretical fitting from the *Comsol* model is displayed as plain light and dark blue lines for up and down pressure sweeps. The red cross (x) and plus (+) symbols are used to show corresponding data points between cycles. The inset from the top panel shows a subset of raw *Polytec* profile measurements at 10, 20 and 30 kPa, for cycle 1. Experimental data points are shown by green dots. The dashed line represents the least-square error approximation of a second-order polynomial.

4.4 Strain Results

Fig. 4.6 shows the pressure/strain relationship, inside a p-VO_2 device, obtained from the calibrated *Comsol* model. Each panel corresponds to a pressure cycle from Fig. 4.5. Upon recovery of the full strain tensor, an asymmetrical biaxial strain is obtained along the $x-$ and $y-$directions as defined by the referential in Fig. 4.1b. The plotted biaxial strain is defined as the norm of the vectorial sum of both components.

The model reveals that the configuration of the electrical lines, placed straight across the die's edge and extending on the membrane, is at the origin of this biaxial strain. This is expected from [179] and illustrated in the inset of the first panel in Fig. 4.6. The biaxial strain applied to the device must be used from here-on to process the electrical measurements to take into account all the main strain components.

The non-uniaxial strain field in the device further showcases the need to properly assess the strain field in polymeric membranes for high-strain studies. The advantage of using a calibrated *Comsol* model is that it allows to capture the complete trend of the strain field without approximation as in [244, 245, 130] for high-strain (>0.01 %) or [155, 127] for small strain.

The strain induced during the up and down sweeps of the pressure cycle is shown by a light blue line with squares and a dark blue line with dots, respectively. As for the deflection measurement, a non-linear hysteretic path is followed by the strain variation. This is unlike what is obtained for small deformation setups like the ones of [155, 157] but expected for polymer based membranes [179]. As for Fig. 4.5, red crosses (x) and plus (+) indicate matching data points between successive pressure cycles.

During the first cycle, a maximal biaxial strain of 0.15 % is obtained at 30 kPa. This value is already superior to the 0.04 % obtained by [127] on its p-VO_2 devices. When the pressure decreases, the permanent deformation of the membrane leads to a small compressive strain of -0.018 % at 0 kPa. For the next cycles, higher maximal strains of 0.2 % and 0.3 % are obtained at 60 and 100 kPa of pressure, respectively.

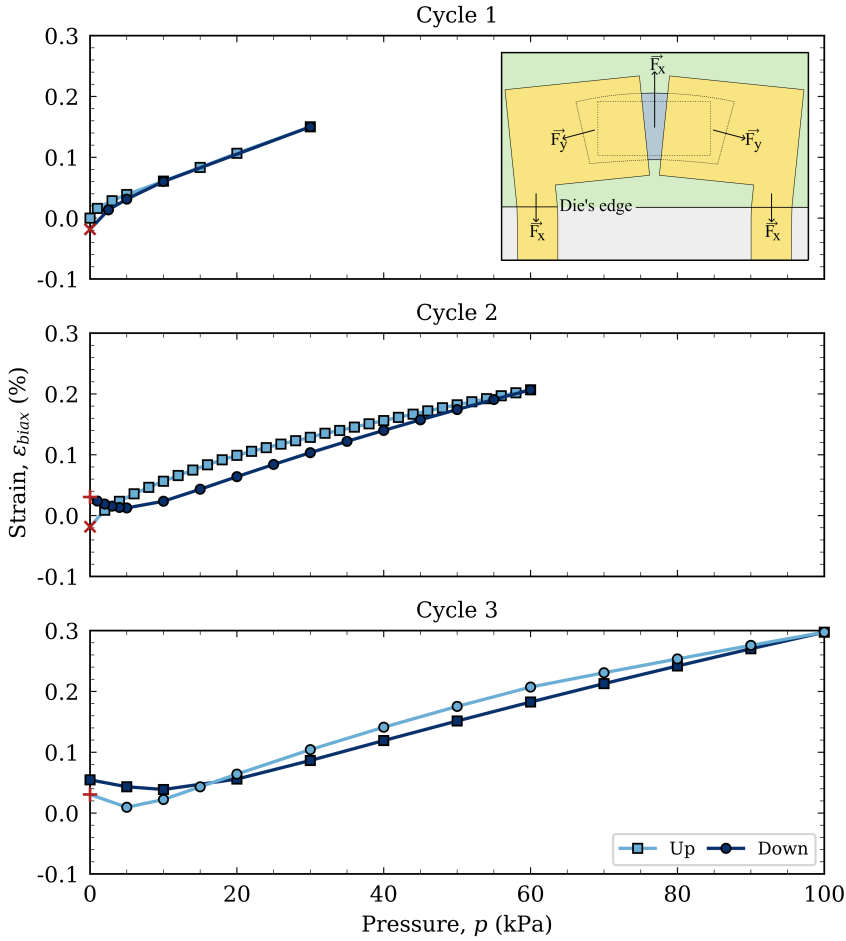


Fig. 4.6 Strain simulation results: Biaxial strain in a p-VO_2 resistor placed alongside the edge of a 1 mm-wide and 2.5 µm-thick polyimide membrane. Each panel provides the strain for its corresponding pressure cycle. The strain induced during the up and down sweeps of the pressure cycle is shown by a light blue line with squares and a dark blue line with dots. The red crosses (x) and plus (+) indicate matching data points between pressure cycles. The inset of the first cycle illustrates the origin of the biaxial strain.

The 0.3% of strain obtained at 100 kPa can be compared to the 0.36% obtained in the second chapter. Both values are close which highlights the benefits of using smaller, square membranes compared to large circular ones. This achievement is to be compared to [89] where strain is induced in a p-VO_2 resistor built on PET via a combination of both PAD and layer transfer. In the paper, a biaxial strain of 0.1 % is applied on the device by bending the entire substrate. The maximal strain is three time inferior to the one obtained in this work. In addition, the bending-radius/strain relationship is not shown and only the increase in strain is reported whereas this work reports both the increase and decrease sweeps of the pressure/strain variation.

Slippage assessment

The interpretation of the results is made under the hypothesis that no slippage occurs at the PI/SiO_2 interface. This hypothesis is supported by the fact that the PI/SiO_2 interface of this chapter is the same as the one of the second chapter of this work. In the second chapter, the excellent agreement between simulated and experimentally measured Raman peak-shift confirmed the absence of slippage at the interface. In addition, in [179], no slippage is observed while a strain of 0.36% is reached. In this chapter, the maximal strain is of 0.3% which decreases the likelihood of slippage.

Furthermore, a microscopic investigation of the membrane was carried out after its pressurisation to 100 kPa. Fig. 4.7 shows four pictures of the 1 mm-wide membrane used in the experiment after being pressurised to 100 kPa. The pictures are taken at various locations and with different filters. No sign of delamination near the edge of the membrane can be seen. While this is not a direct proof that no slippage occurs *in-situ* at the device location, the fact that no delamination is occurring near the edge is a good sign as the local strain at the center of the membrane's edge is computed to reach 4% in the PI/SiO_2 stack according to the *Comsol* model. This is more than ten fold higher to the local strain at the device location.

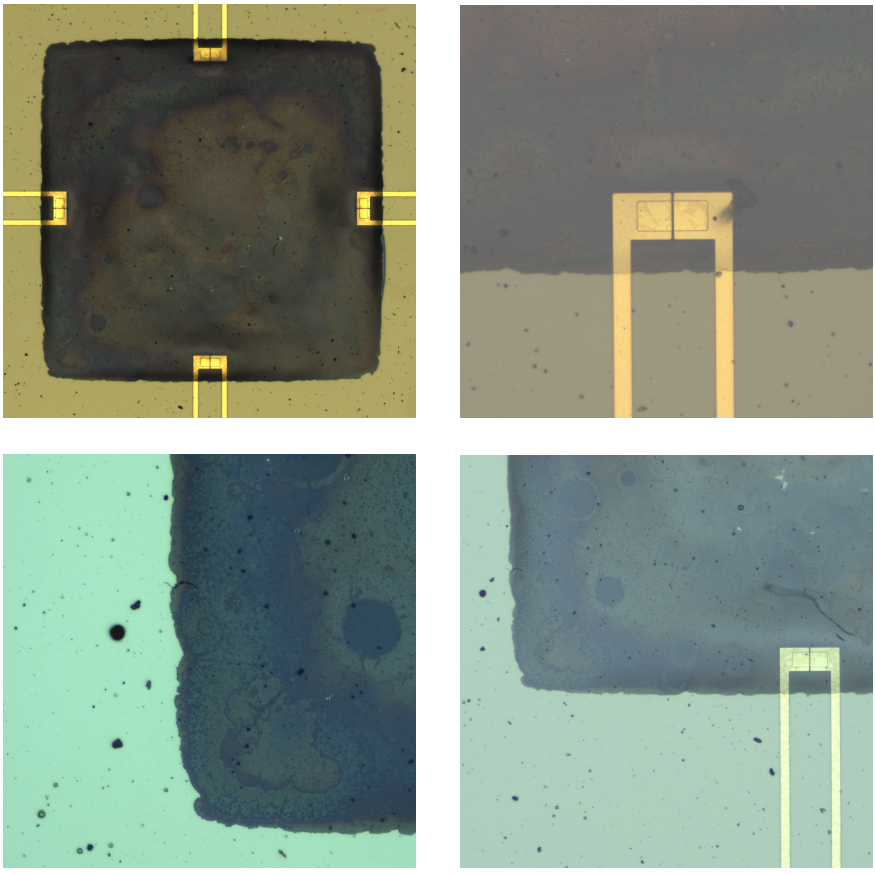


Fig. 4.7 Picture of the 1 mm-wide and 2.5 µm-thick polyimide membrane used in the experiment after being pressurised to 100 kPa. The pictures are taken with various microscope filters and at different locations to highlight the lack of delamination at the membrane's edge.

4.5 Resistance and Gauge Factor

The results of the electrical measurements are displayed in Fig. 4.8. Three panels are used to show the different pressure cycles. The difference with the previous graphs is that the resistance variation is plotted as a function of the strain instead of as a function of the pressure. This is done to remove any trend from the IV that is not linked to a monotonic variation of the applied strain. The data is presented as the relative resistance variation (ΔR) normalised by the initial resistance R_0. In this case, $R_0 = 11.7\,\mathrm{M}\Omega$.

The top panel, cycle 1, contains an inset showing a subset of four raw IV's measured in the quasi-linear region between -0.15V and 0.15V at 0, 10, 20 and 30 kPa. This corresponds to 0 %, 0.06 %, 0.11 % and 0.15 % of applied strain, respectively. The resistance is recovered from the raw IVs by taking the derivative of a first order least-square error approximation fitted on the measurement. The value of the resistance is measured at each pressure step and plotted as a function of the corresponding strain. Resistance values are represented with light blue squares and dark blue circles for increasing and decreasing strain, respectively.

For all three panels, a significant increase of the resistance is observed with increasing strain. This behaviour is expected since tensile strain in VO_2 leads to a partial and reversible transition of the crystal from its M1 to its M2 state when measured at low voltage far from the IMT [113, 114, 115, 116, 117, 118, 119, 120]. This partial transition leads to an increase of the electrical resistance with an M2 phase three times more resistive than the M1 phase [116, 117].

Over the first cycle, the relative change in resistance is of 45 %. This value can be confronted with [89] where a 40 % increase is obtained at 0.1 % of strain. When the pressure is decreased, the resistance drops following a similar but slightly flattened path. Notice that the measurement spans below zero percent of strain which is due to the residual compressive strain visible on the top panel in Fig. 4.6.

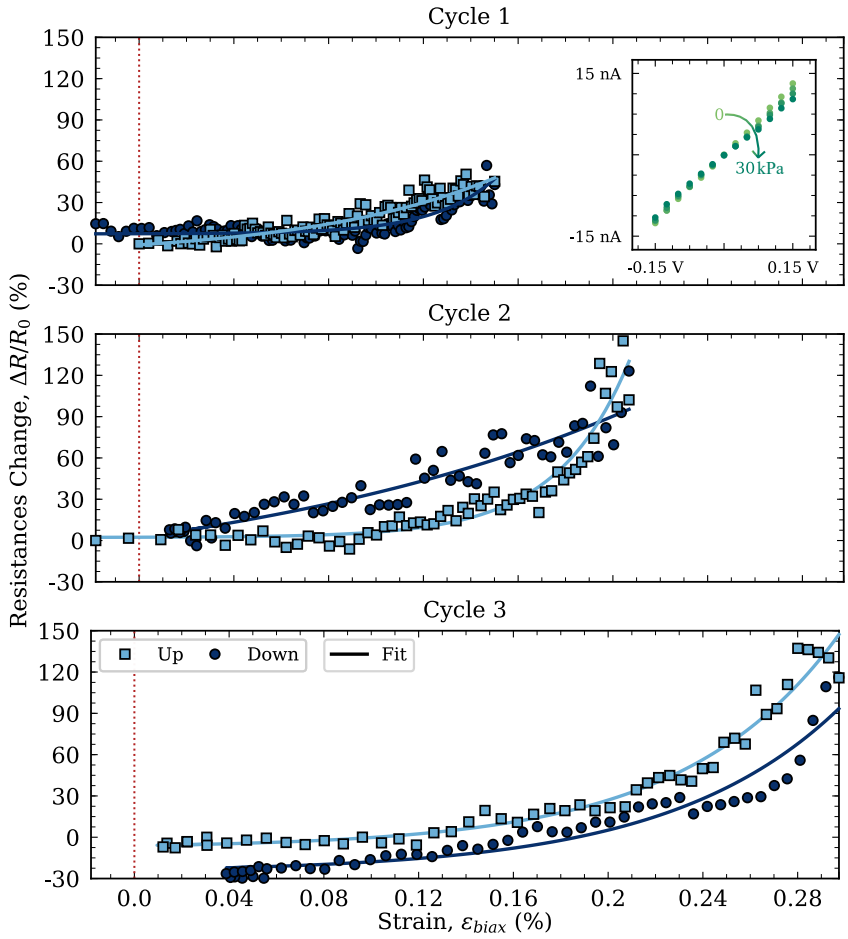


Fig. 4.8 Electrical measurements: IV measurements of p-VO_2 resistors under increasing tensile strain. Each panel corresponds to a pressure cycle but the results are plotted as a function of the obtained strain. Experimental results are plotted using light blue squares and dark blue dots for increasing and decreasing strain sweep, respectively. Data is plotted as relative variation of the resistance compared to R_0. A least-square error approximation of an exponential is fitted on the data points by light and dark blue lines. The inset from the top panel shows a subset of four raw IV measurements at 0, 10, 20 and 30 kPa plotted between -0.15 and 0.15V

For the second cycle, a steep increase of the resistance of 145 % is observed at 0.2 % of tensile strain. An important hysteresis that doesn't return to the initial resistance value appears when the strain decreases. The hysteretic variation of the resistance of strained VO_2 is mentioned for epitaxial layers [121] and nanobeams [117]. However, in those papers, the resistance variation is shown to be fully reversible which is not the case here. [89] explains that the steep variation of the electrical resistance of p-VO_2 comes from a process of grains connections and disconnections with increasing and decreasing strain. This phenomenon, further validated by [246, 247] for other polycrystals, can be used to explain the origin of the hysteresis due to the similarities in the microstructure of the p-VO_2 from this work and the one of [89]. Upon increase of the strain, a grain disconnection process occurs. This disconnection process, when done in a moderate strain range, can be considered reversible. This can be seen in cycle 1 of Fig. 4.8. However, upon further straining, permanent defects or grain repositioning appear in the polycrystal leading to a permanent modification of the device resistance. This is further illustrated in the second and third cycle of the experiment with a clear hysteresis. Random repositioning of the grains inside the device leads to a modified final resistance during the pressure decrease.

Reading [246, 247, 89, 248], it quickly appears that the contribution of the grain dislocation, or cracks, is far from anecdotal in the overall gauge factor of the material. This is made obvious when looking at the experimental values in Fig. 4.9. Those results are obtained by fitting of a least square error approximation of an exponential on the data of Fig. 4.8 and taking its derivative relative to the strain. The fitting is shown by light and dark plain blue lines in Fig. 4.8 and the results are plotted by plain blue lines in Fig. 4.9. Values from literature are reported in plain [127] and dotted [89] red lines for p-VO_2 and in dashed [121] and interrupted dashed [117] pink lines for a c-VO_2 epitaxial layers and nanobeams, respectively.

Since the electrical resistance variation follows an exponential, the gauge factor, its derivative, also follows a continuous exponential increase. This is unlike what is reported for c-VO_2 nanobeams [117] and epitaxial layers [121] subjected to tensile strain, as shown in Fig. 4.9. In those papers, the gauge factor is shown to decrease from 175 to 150 for [117] and from 620 to 370 for [121] when strained to 0.1 %. Further increase of strain yields no change in the gauge factor.

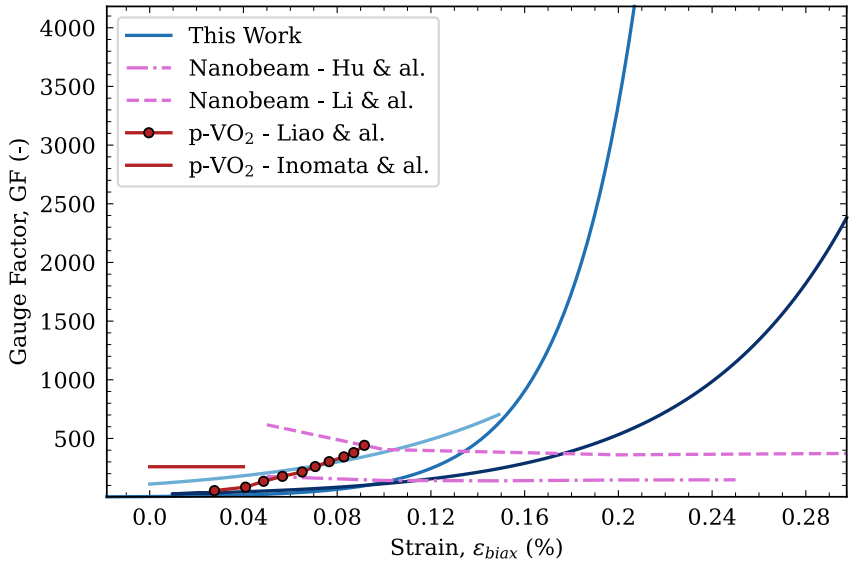


Fig. 4.9 Gauge factor of p-VO_2 and c-VO_2 devices under strain. The gauge factors from the three pressure cycles of this work are represented with plain blue lines. Values from literature are shown in red and pink. The gauge factors of strained p-VO_2 are shown in plain and plain with dots red lines for *Inomata & al.* [127] and *Liao & al.* [89], respectively. Gauge factors for c-VO_2 nanobeams are displayed as dashed pink and interrupted dashed pink lines for *Li & al.*[121] and *Hu & al.* [117], respectively.

Furthermore, looking into c-VO_2, a complete transition from M1 to M2 at room temperature cannot happen below 1.75% of tensile strain [249]. The full M1 to M2 transition comes with a three-fold increase of resistivity [116, 117] which would be compatible with the results from Fig. 4.8 should the strain reach 1.75%. However, the experiment is limited to 0.3% of strain which only allows a partial reconfiguration of the monocrystalline grains in the p-VO_2 thin film from the M1 to the triclinic state. According to [249], between 0 and 1% of strain, a continuous M1 to triclinic transition occurs in the VO_2 crystal. The triclinic state is an intermediate phase of the VO_2 crystal between the M1 and M2 state in which fractions of the two phases coexist. This partial reconfiguration below 1% leads to a fraction of the resistive change compared to the full M1 to M2 transition.

The combination of the gauge factor decrease and saturation with tensile strain and the impossibility to get a complete M1 to M2 transition implies that the exponential increase of the GF in p-VO_2 cannot be attributed to the intrinsic phase change in the material alone but might come from grain dislocation as in [89].

Indeed, [89] reports a similar exponential variation of the gauge factor but for p-VO_2 grown by low-temperature PAD and strained to only 0.1 %. Our work validates this phenomenon and underlines the necessity to report the full GF-strain curve for p-VO_2 instead of a single value at the nominal deformation. For reference, [127] reports a gauge factor of 256 at 0.04 % of strain and considers it constant across the complete strain range. This is also the case for [149] where a gauge factor of 534 is reported at -0.07 % of strain.

The significance of the contribution of grain dislocation in the overall gauge factor is further illustrated in Fig. 4.9. During the second cycle the gauge factor reaches a value of 4180. Considering the grain dislocation phenomenon, it might continue to increase exponentially up to the full disconnection of the grains. After the second cycle, the damage made to the polycrystal structure leads to an overall smaller gauge factor of the p-VO_2 device even at 0.3 % of strain where a maximal value of 2382 is obtained. This illustrates clear limits in the maximal measurable strain with p-VO_2.

4.6 Conclusion

This chapter reports the integration of p-VO_2 resistors on a 2.5 µm-thick and 1 mm-wide polyimide membrane for high-strain studies. The proposed process uses the developed monolithic fabrication scheme to integrate high-quality [145, 147] sputtered p-VO_2 on polyimide without limitation despite the use of thermal annealing. The proposed solution gets rid of the need for complex layer transfer [146, 89], making for simpler integration of the material on flexible substrate.

A biaxial tensile strain of 0.3 % is induced in the p-VO_2 device. This can be compared with [89] where strain is induced in a p-VO_2 resistor built on PET via a combination of both PAD and layer transfer. They report 0.1 % of applied strain. Another comparison could be with [127] where a strain of only 0.04 % is reached.

Careful study of the electrical resistance variation is performed under progressively higher levels of strain. An exponential increase of both the resistance and gauge factor is reported for the first time in sputtered p-VO_2. This is in accordance with the literature for p-VO_2 grown by PAD [89]. This exponential behaviour is attributed to a dislocation phenomenon between the grains of the polycrystal [246, 247, 89, 248]. However, a direct proof of the grain dislocation hypothesis is required in order to completely validate it. To do so, a redesign of the experiment should be carried out to allow the measurement of strained p-VO_2 under an AFM, SEM or TEM. This is left as a prospect as it would require both the abandon of the polyimide layer to allow for imaging and the design of a smaller actuation mechanism compatible with the proposed equipments.

This finding of the exponential variation of the gauge factor with strain highlights the need for proper and complete reporting of its variation in strained p-VO_2. Reporting only one value at the nominal strain does not capture the entire behaviour and, by nature of the exponential, may lead to substantial over or under estimation of the gauge factor which won't allow fair comparisons between results.

Finally, the chapter shows that strain larger than 0.1 % creates permanent defects in the p-VO_2 device. This, in conjugation with the non-constant and exponential nature of the gauge factor, makes the material a poor candidate for wide range strain sensing.

4.7 Take home messages

- The chapter demonstrates the fabrication of thermally annealed sputtered p-VO_2 resistors on a 2.5 µm-thin and 1 mm-wide polyimide membrane using a monolithic fabrication scheme.

- A 0.3 % biaxial strain is induced in the fabricated device upon bulging of the membrane. This represents a three-fold increase compared to literature.
- The gauge factor of p-VO_2 is shown to follow a continuous exponential increase with strain. This is attributed to a superposition of the M1 to M2 phase reconfiguration with strain and with a grain dislocation process.

Conclusions and perspectives

In the recent years, the apparition of new sectors and technical opportunities led to the development of novel strain sensors [3, 4, 5, 6]. In term of sectors, domains like smart packaging [10, 6], smart sensors [7, 8, 9] or health care [11, 12, 13, 14, 15, 16] required the creation of flexible and compliant multifunctional sensors capable to respond to multiple stimuli such as temperature and strain [17, 18, 19, 20, 21, 22]. This development was boosted by progress in terms of signal processing and AI that enable to decorrelate the physical effects in the electrical outputs of the sensors [17, 18, 19, 20, 21, 22].

Researchers worked on multifunctional sensors most often based on piezoresistive materials due to their simple read-out and construction [1, 40, 47, 48]. They have especially been looking for a single inorganic material that can be fabricated onto flexible MEMS with standard microfabrication techniques while featuring a high gauge factor and sensitivity to temperature for multifunctional implantable sensors [89].

Vanadium dioxide is considered as a promising candidate thanks to its intrinsic sensitivity to external energy input [90]. [127, 250] used high-performance annealed sputtered p-VO_2 to build strain and pressure sensor with a gauge factor of 259 reported at 0.04 % of strain. Attempts to integrate VO_2 on flexible sensors to expend the strain range have been made but relied on the use of low-crystallinity [145, 146, 140], low-temperature VO_2 [139, 140, 141, 142, 131, 143, 144] or complex layer transfer processes [146, 89]. Monolithic integration of high-quality [145, 147] sputtered p-VO_2 layers onto flexible substrates is of interest but remained out of reach due to the limited thermal budget of polymers [150, 150, 151] and the high-temperature annealing required to reach the desired level of crystallinity [152, 153, 154].

This work propose to study the piezoresistive properties of highly-strained, thermally annealed p-VO_2 fabricated by sputtering. More specifically, the thesis proposes to characterise the evolution of the gauge factor of sputtered p-VO_2 under high-strain as a first step toward its use in multifunctional sensor. In a nutshell, it tries to answer the following scientific question:

Can thermally annealed sputtered p-VO_2, integrated on a flexible substrate, be used for high-strain multifunctional sensing applications?

This question is split into four smaller inquiries that lead to specific scientific contributions that we re-state here below.

Chapter 1

The first chapter explores the monolithic fabrication, without thermal budget, of inorganic microelectronics on a polyimide membrane. A demonstration of the process is made on silicon devices to evaluate its feasibility with a well known cleanroom material. The question in this chapter is:

How to integrate c-Si devices, in a monolithic way and without process limitation, on a thin polyimide membrane?

The process demonstrates the integration of c-Si devices on a 2.7 mm-wide and 3.6 µm-tick polyimide membrane using conventional monolithic processing.

Up-to-now, high-performance microelectronics requiring the use of thermal annealing relied on complex layer transfer techniques. For instance, [136] used this approach to build a flexible eye-shaped camera based on c-Si pixels. Similarly, layer transfer was used to produce silicon and germanium based sensor on PDMS and polyimide [137, 180, 130]. New materials benefits from the approach as-well with demonstration of graphene and even VO_2 based flexible sensors [251, 89]. While undeniably effective, it is notoriously complex and hard to scale [146].

The approach of this chapter solves those limitations. The thermal budget issue is addressed by adding the polyimide layer at the end. This is done via the spin-coating of a precursor.

By doing so, the fabrication of the devices of interest is carried out normally, without thermal budget or limitation in the choice of the fabrication techniques, temperatures or materials. Furthermore, the integration on the final flexible substrate is simplified since it only requires a spin coater and an oven for the low-temperature curing of polyimide.

The chapter also introduces a *bulge-test* setup to measure the *in situ* properties of the membrane and devices. The setup is made from a pressure vessel that can go up to 100 kPa while being usable with probes, white light interferometry and Raman spectroscopy. This makes the entire setup, with the fabrication, a great candidate for multiphysics characterization of devices under strain.

A preliminary set of experimental measurements and *Comsol* simulations of the membrane maximal deflection is presented. It highlights the fact that the membrane does not deflect following an expected cube-root trend [181, 177, 178] but diverges from it past 50 kPa due to plastic deformation of the stack [179]. It means that the membrane cannot be modelled by conventional MEMS [155, 157] or flexible MEMS models [181, 177, 178]. This is a major limitation since those models are the ones used to get a pressure-strain relation.

Chapter 2

The second chapter extends the introduced *Comsol* model to consider the plastic deformation of the stack and to recover the strain field in the c-Si devices. This is done to obtain a pressure-strain relation in both the elastic and plastic deformation regime. The scientific question of the chapter is:

Can a Comsol simulation model the plastic deformation of a polyimide membrane to compute the local strain field induced in the carried c-Si devices and how much strain can be induced in the c-Si resistors?

The *Swift* plastic model [184] is implemented in *Comsol* to simulate the behavior of the membrane. The relative stress, strain and hardening exponent are fitted on an experimental measurement of the membrane deflection under pressure to calibrate the model.

During the increasing pressure sweep, the membrane deflection follows a cube root trend before entering in plasticity at 50 kPa. Past this pressure point, the stack enters in a plastic deformation regime [179]. This is illustrated by the decrease pressure sweep which leaves the membrane at a permanently deformed state at rest. An excellent agreement of the measurement and the simulation is reached.

The full strain tensor is computed by the calibrated *Comsol* model. It is biaxial and asymmetrical with strain components along the x- and y-direction. This is unlike what is obtained for small deflection setups where devices located on the edge of the membrane are expected to undergo uniaxial straining [127, 155]. A maximal strain of 0.37 % is computed in the c-Si device. This is a 10-fold increase compared to conventional bulk micro-machined or stress compensated membranes [127, 128]. It however is 10-times lower than what is reported by [130] but this is linked to their use of ultra-thin 10 nm-thick silicon devices compared to our 300 nm-thick pixels. Since the strain is directly linked to the device thickness, reducing it leads to an increase in strain.

Finally, the simulated strain field is validated by computing the shift of the silicon Raman peak and comparing it to an experimental measurement. This was, to the best of our knowledge, never done in literature. The Raman peak-shift is usually used to get an estimate of an uniaxial or perfectly biaxial strain in c-Si [130, 195]. This requires to make hypothesis or simplification of the expected strain field which is not possible in this case [130, 195, 196]. An excellent agreement of the simulation and experimental peak-shift is achieved. This means that the strain field inside a device fabricated on a polyimide based membrane can be recovered by a fitted *Comsol* model [179].

Chapter 3

This chapter dives into the integration of thermally annealed sputtered p-VO_2 on a thin polyimide membrane. The goal of this chapter is to check the adhesion of p-VO_2 to poyimide and recover the Young's modulus of the deposited layer. The question under study is:

How to integrate thermally annealed p-VO_2 on a thin, released, polyimide membrane to recover its Young's modulus?

The fabrication process for a monolithic integration of sputtered p-VO_2 is presented with all the synthesis and characterization steps required to obtain stoichiometric VO_2. A 220 nm-thick layer of p-VO_2 is fabricated onto a 2.5 mm-wide and 3.2 µm-thick polyimide membrane without thermal budget. To the best of our knowledge this is the first time that this is done as previous attempt relied on low-temperature deposition of poor quality VO_2 [145, 146, 140] or layer transfer [145, 147]. The integration highlights the need for an adhesion promotion layer between the p-VO_2 and the polyimide. A PECVD SiO_2 layer is used.

The fabricated membrane stack is used to recover the Young's modulus of the material. This physical parameter is critical to obtain a proper estimation of the strain in p-VO_2 devices from the *Comsol* model. Computing the specific modulus is required since a wide range of values are provided in literature between 86 [160] and 170 GPa [161].

To recover the modulus, a bulge test inspired from [238, 239, 240, 241] is used. A membrane with a blanket layer of p-VO_2 is measured and a *Comsol* model is fitted on its maximal deflection relative to pressure. Fitting the parameters gives a measurement of 120 GPa for the Young's modulus of the deposited layer. This is in the reported literature range [238, 239, 240, 241].

Chapter 4

This final chapter integrates thermally annealed, sputtered and patterned p-VO_2 resistors and studies their gauge factor under high-strain. The scientific question covered by this chapter is:

How does the gauge factor of patterned p-VO_2 fabricated via reactive sputtering and thermal annealing behave under high-strain?

A monolithic process is used to integrate p-VO_2 resistors on a 1 mm-wide and 2.5 µm-thick polyimide membrane. The membrane is subjected to increasing pressure sweeps from 0 to 100 kPa and the variation of the electrical resistance of the p-VO_2 is measured along with the deflection of the membrane. The *Comsol* model is adapted to the membrane stack and geometry and the strain field inside of the p-VO_2 resistor is computed.

An asymmetrical biaxial strain field is obtained and reaches 0.3 % of deformation in the resistors. This is to be compared with [89] where strain is induced in a p-VO_2 resistor built on PET via a combination of both PAD and layer transfer. In the paper, the maximal amount of strain only reaches 0.1 %. Another comparison could be with [127] where a strain of only 0.04 % is reached. The 0.3 % of strain in sputtered p-VO_2 reported in this work is, to the best of our knowledge, the highest reported in literature.

Under strain, the gauge factor of p-VO_2 follows an exponential increase up to 4180 at 0.3 % of deformation. This is unlike what is reported for c-VO_2 nanobeams [117] and epitaxial layers [121] where the gauge factor is shown to decrease from 175 to 150 [117] and 620 to 370 [121] between 0 and 0.1 % of strain. This highlights the need to report the complete GF-strain relation. Indeed, looking at 0.1 % of deformation sputtered p-VO_2 and epitaxial c-VO_2 intersect but this does not allow the comparison as their slopes are opposed.

The continuous and exponential increase of the gauge factor is attributed to both the intrinsic sensitivity of the VO_2 crystal with strain [113, 114, 115, 116, 117, 118, 119, 120] and the contribution of grain dislocation [246, 247, 89, 248]. This is in line with [89] which is the only other paper to report the exponential behavior of the p-VO_2 gauge factor with strain. It reports a gauge factor of 400 at a strain of 0.1 % in p-VO_2 fabricated with PAD. Our study is the first one to report this phenomenon for sputtered p-VO_2 and is the only one to reach 0.3 % of strain.

Finally, this chapter shows that strain above 0.1 % induces permanent defects in the polycrystal. The resistance change with strain follows an hysteresis and does not return to its initial state at rest. This is in line with the dislocation hypothesis of [246, 247, 89, 248]. This finding sets clear boundaries for the admissible strain range of sputtered p-VO_2 strain sensors. A proper SEM or AFM experiment would be of interest to image the grain dislocation with strain and formally prove this hypothesis.

Perspectives

The work presented in this thesis studied the monolithic integration with no thermal budget of electronics on polyimide and the behavior of p-VO_2 under strain. Along the way, potential development emerged. They are listed here below.

Multiphysics strain-temperature study of p-VO_2

This thesis characterises p-VO_2 under strain. This is only the first step for the development of multifunctional strain-temperature p-VO_2 sensors such as the one presented in [89]. A possibility is to put the *bulge-test* setup designed in this work inside of a climatic chamber. This will allow the electrical measurement of heated and strained p-VO_2 resistors.

A first preliminary study has been carried out using a *Comsol* model. A multiphysics thermal and mechanical simulation was performed to check the impact of temperatures between 20°C and 90°C on the membrane deflection and strain. Temperatures above 90°C were not tested since VO_2 is expected to be fully metallic at this temperature.

Figure Fig. ⋆.10(b) shows the impact of temperature on the maximal deflection of the membrane. The deflection increases with temperature and reaches a maximal deflection at 40 kPa of 21.2 µm and 22.7 µm at 20°C and 90°C, respectively. This translates into a shift of maximal strain at 40 kPa from 0.46 % to 0.53 % along the membrane edge at 20°C and 90°C, respectively. This is shown in Fig. ⋆.10(a). No modification of the pressure-deflection and pressure-strain profiles is observed.

Those results were obtained with a simplified stack without devices. The strain is measured in the polyimide which explains why it is so high compared to what is presented in chapter two and four. The model should be expanded to study the plastic deformation of the heated membrane.

While challenging, further development of this model and of the experimental setup would allow the use of the polyimide membrane as a great tool for true multiphysics measurements of any materials. This includes electrical, thermal, optical and mechanical characterization.

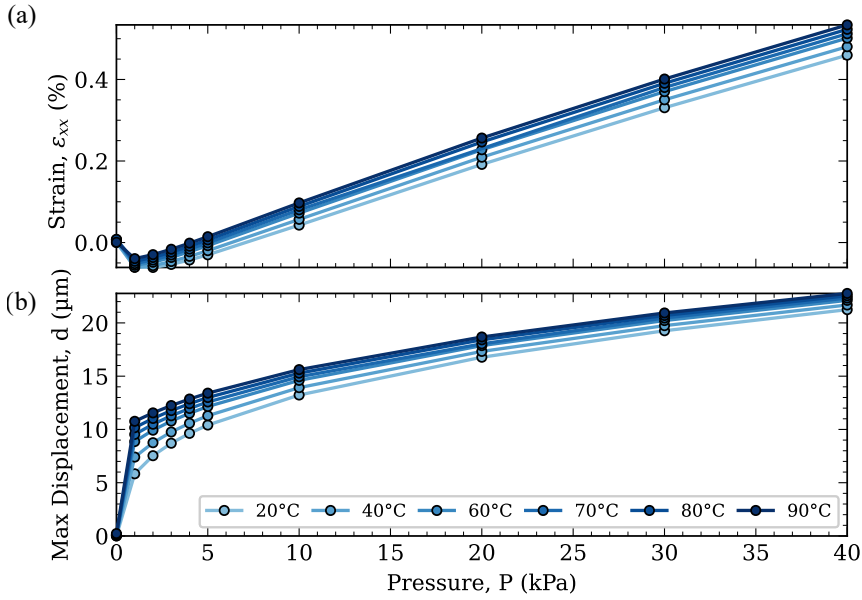


Fig. ⋆.10 Impact of the temperature on a 1mm-wide and 2.5 µm-thick polyimide membrane with no devices. (a) Evolution of the maximal deflection as a function of the pressure and the temperature. Light to dark blue lines with dots are used to represent temperatures from 20°C to 90°C. (b) Strain toward the center of the membrane inside the polyimide as a function of the pressure and the temperature. Light to dark blue lines with dots are used to represent temperatures from 20°C to 90°C.

Fully released polyimide thin films

A variation of the process presented in this work is shown in Fig. ⋆.11. It allows to fabricate fully released polyimide films with integrated microelectronics. During the process back end, the XeF_2 or Bosch membrane release is replaced by an unmasked etching of the bulk silicon. This leaves a fully released thin film.

Fig. ⋆.12 shows the fabrication results of a fully flexible die carrying two-terminal p-VO_2 resistors. Fig. ⋆.12(a) shows the die glued to a piece of office tape while Fig. ⋆.12(b) and Fig. ⋆.12(c) show a microscopic picture and SEM micrograph of the fabricated sample. The micrograph shows a 110 nm-thick layer of p-VO_2 with grains of 200 to 500 nm in width.

The material was checked to be stoichiometric by Raman spectroscopy as visible in Fig. ⋆.13(a).

A preliminary result shows that the fabricated p-VO_2 resistors maintained their MIT property. This is also the case for the devices of chapter 4. Fig. ⋆.13(b) shows a measurement of the electrically triggered MIT. Only the transition from insulating to metallic is shown.

This perspective is of interest for two reasons:

- **Uniaxial high-strain experiment:** The membrane developed in this thesis induces an asymmetrical biaxial strain field in the device under test. The fabrication of fully released devices allows to study p-VO_2, c-Si or other materials under high uniaxial strain. This is of interest for monocrystalline materials for which the response to strain can depend on the relative crystallographic orientation.
- **Implantable and wearable devices:** While being a good platform to characterise the impact of strain on a material or device, the membrane format cannot be conformally implanted on a curved surface. The release process allows to fabricate fully flexible dies carrying any materials or devices. The big downside of this approach is that the fabrication scheme does not allow for large scale manufacturing since it requires the dissolution of the complete bulk silicon. Processes oriented research is required to find a sacrificial layer compatible with the material of interest. This could lead to the fabrication of advanced MEMS flexible sensors with high-performance organic or inorganic materials.

Engineering of smart metal line

In the current membrane design, the electrical lines extend from the die to the membrane via the edge center. This choice is suboptimal since, on a square membrane, the maximal amount of strain is induced at the center of an edge while almost no strain is generated in the corners of the diaphragm [242]. This causes two issues.

The first one is that the metal lines act as anchor points and generate a torque on the device under test. This is, in part, at the origin of the important strain

component along the y-axis. The second issue is that their positioning leads to the tearing of the lines on the die's edge at around 0.4 % of strain in the device under test. A possible improvement to study would be to have the metallic lines extend from the die onto the membrane from the corners, where the strain is null [242].

Proving the grain dislocation hypothesis

This work poses the hypothesis that the movement of the individual grains in the p-VO_2 thin film is at the origin of the exponential increase of the gauge factor. This hypothesis was originally presented in [89] which reports a similar phenomenon for p-VO_2 deposited via PAD. However, a common limitation of this work and [89] is that no direct proof is brought to support this hypothesis. Direct imaging would allow to prove - or disprove - the grain dislocation theory.

Various approaches were considered such as AFM, SEM or TEM but the polyimide layer, acting as a blanket and dielectric, renders their use impossible. A redesign of the experiment could allow such experiment to be performed but would require the following changes.

- **Removal of the PI layer:** As mentioned, the thick polyimide layer renders the use of the proposed techniques impossible. This is because it either acts as a blanket which hides the topology of the p-VO_2 or as a dielectric. A new design, based on the transfer of the p-VO_2 layer on a conductive substrate or the addition of a conductive layer between the p-VO_2 and the PI could allow the use of AFM or SEM, respectively.

- **Redesign of the actuation mechanism:** The bulge test setup is incompatible with the use of an SEM or an AFM. An on-chip actuation, a transfer on a push-to-pull structure or the use of tensile testing equipment compatible with an SEM should be investigated.

Considering both elements, a promising path would be to fabricate a fully released PI die barring a p-VO_2 blanket layer using the presented full release method. The fully released die should be integrated onto a dog bone sample carrier by gluing the die upside down to try to image the p-VO_2 layer through the thermal silicon dioxide layer which will have to be kept as thin as possible. This work established that 50 nm-thick thermal silicon dioxide

allows for proper growth of p-VO_2. Thinner layer could be considered.

The completed sample would, at this stage, be compatible with commercial tensile testing unit designed to work in an SEM.

Another possible approach would be to completely drop the polyimide integration an use an on-chip MEMS tensile test such as the one presented in [124, 252, 253].

Closing thoughts

In the end, the thesis deviated from the production of a multifunctional vanadium dioxide based sensor to the development of a polyimide based platform to study material properties under strain. The main outcome of this work is that the designed platform allowed to measure the gauge factor of highly strained p-VO_2.

Taking a step back, we can try to briefly answer the main question of this thesis which was:

Can thermally annealed sputtered p-VO_2, integrated on a flexible substrate, be used for high-strain multifunctional sensing applications?

At this stage, the main conclusion is that sputtered vanadium dioxide will not be usable for high-strain sensing but might find its place in applications that require highly sensitive strain and thermal sensing. As mentioned in the introduction, the domain that feels the most suited is in implantable devices for cardiovascular diseases prevention. However, with strain mitigation strategies, p-VO_2 devices might someday be used for very high and sensitive strain sensors in spiking based sensing circuits. Such platform would benefit from both the intrinsically high sensitivity of the VO_2 crystal and from its complete transition, making for potential wide range strain sensing.

Concerning the developed models and processing techniques, we strongly believe that they offer a scientific tool of interest for strain studies. Indeed, up-to-now, studies in the field of flexible electronics required the use of specialised transfer equipments which many laboratories do not have. Despite the downsides of the proposed process, be it that the membranes enter in plasticity and that the released film cannot be mass produced due to the

need of substrate etching, they offer a great set of tools for low volume scientific samples production for strain and multiphysics studies.

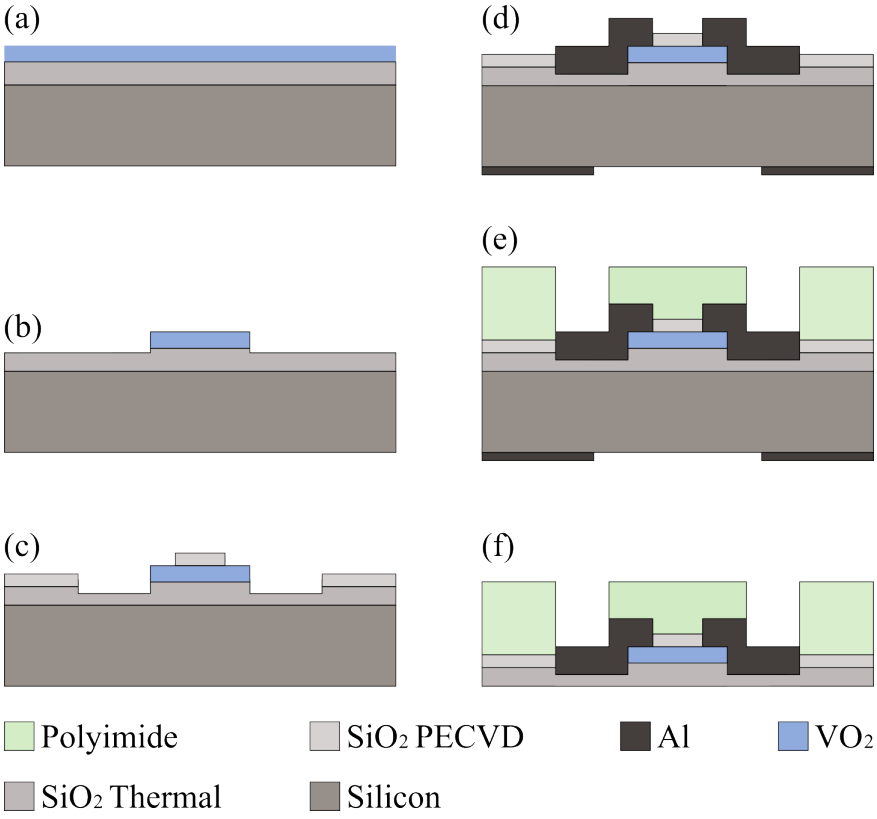


Fig. ⋆.11 Process flow schematics: Summary of the fabrication process to integrate p-VO_2 resistors on fully release, 2.5 µm-thick, polyimide. (a) Initial bulk silicon wafer with 104 nm of thermal SiO_2 on top. (b) Sputtering and RIE patterning of a 110 nm-thick p-VO_2 layer. (c) Deposition and patterning of 20/200 nm-thick Cr/Au electrical contacts by thermal evaporation and lift-off. (d) Deposition and patterning of a 50 nm-thick SiO_2 adhesion layer via PECVD and RIE. (e) Spin coating of a 2.5 µm-thick layer of polyimide and contact opening by wet etching of the precursor. (f) Membrane release via bosh process.

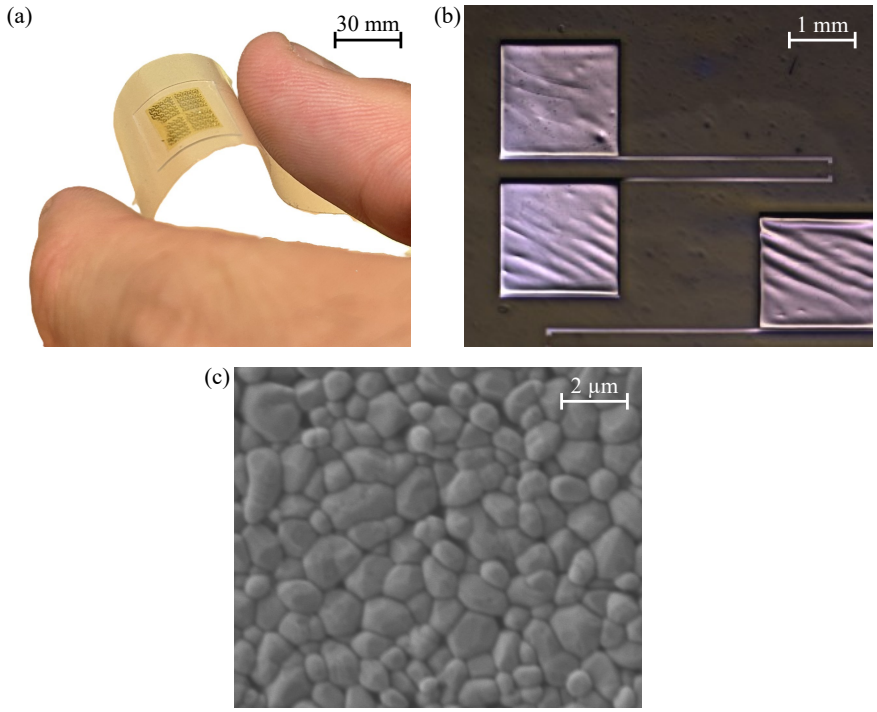


Fig. ⋆.12 Patterned vanadium dioxide resistors on fully released 2.5 µm-thick polyimide thin-film: (a) Macroscopic image of a 1 x 1 cm^2 fully released, 2.5 µm-thick, PI thin film with two-terminal p-VO_2 resistors reported on office tape. (b) Microscopic image of a two-terminal p-VO_2 resistor. (c) SEM micrograph of the p-VO_2.

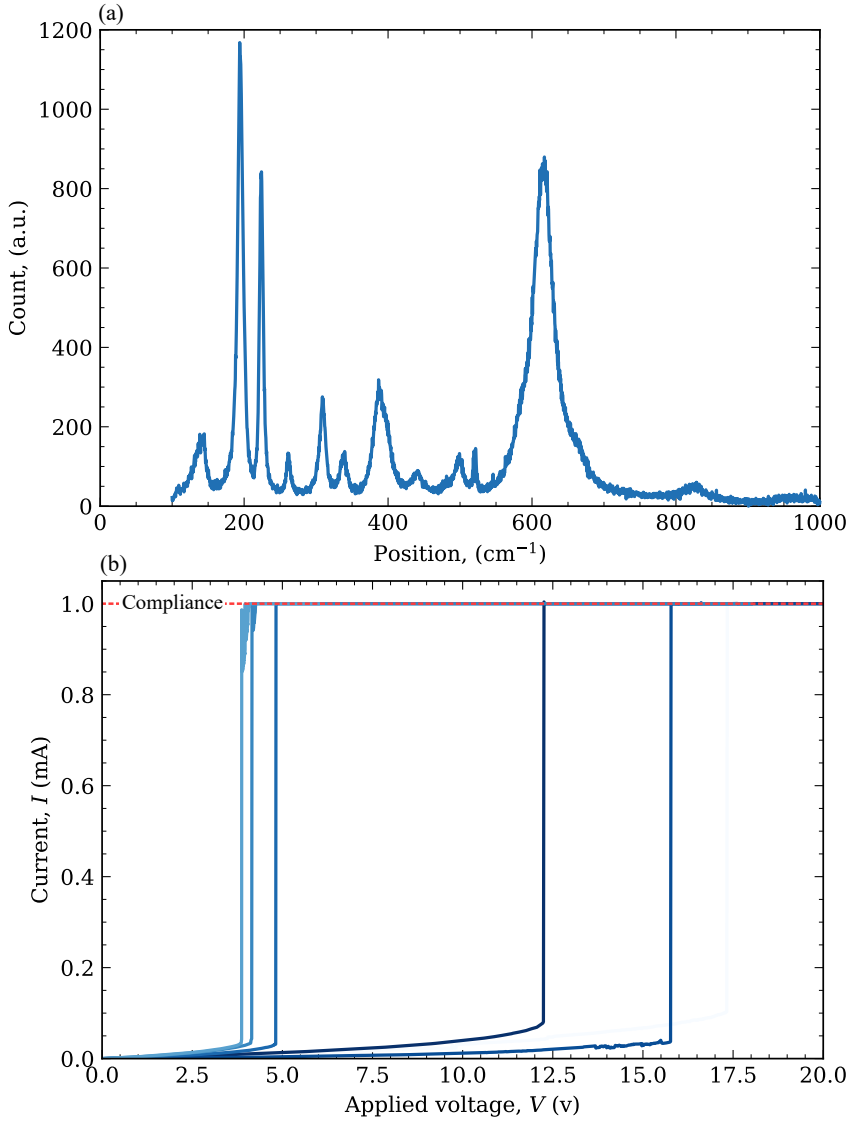


Fig. ⋆.13 Characterization of p-VO_2 two-terminal resistor fabricated on a 2.5 µm-thick fully released polyimide thin film: (a) Raman spectrum of the deposited p-VO_2. (b) Electrical measurement of the transition of the p-VO_2 resistor. A compliance of 1 mA is imposed and represented by a red dashed line. A voltage sweep from zero to 20 V is applied. Successive transition are shown by plain line going from dark to light blue.

Author's publication list

Published work

Parts of the work presented in this manuscript have been published during the doctoral training, either in conferences (CP) or in journals (JP).

[JP1] L. Lahaye, N. Roisin, N. André, D. Flandre and J.-P. Raskin, "Design, Fabrication, Modelling and Characterization of a Polyimide-Based Membrane for High Strain Studies in Microfabricated Devices", in *IEEE Transactions on Materials for Electron Devices*, 2025.

[CP1] L. Lahaye, N. Roisin, J.-P. Raskin and D. Flandre, "Accurate estimation of Young's modulus of VO2 thin film integrated on polyimide for high strain studies", Talk in *Measuring By Light*, 2025.

[CP2] L. Lahaye, J.-P. Raskin and D. Flandre, "Fabrication of Vanadium Dioxide Resistors on Fully-released Polyimide Thin Films for High Strain Studies", Talk in *MNE*, 2025.

[JP2] N. Roisin, L. Lahaye, J.-P. Raskin and D. Flandre, "Electron mobility in silicon under high uniaxial strain", in *Solid-State Electronics*, 2025.

[JP3] T. Ratier, M. Vanbrabant, X. Zeng, L. Lahaye, J.-P. Raskin and D. Flandre, "Electro-Thermal Characterization of Conductive Filament in Vanadium Dioxide Memristors using Thermoreflectance Imaging", in *Applied Electronic Materials*, 2026.

Submitted work

[JP4] L. Lahaye, J.-P. Raskin and D. Flandre, "High-Strain Characterization of Polycrystalline Sputtered Vanadium Dioxide Resistors on Polyimide Membranes", in *Advanced Materials Technologies*, 2026.

[JP5] T. Ratier, L. Lahaye, X. Zeng, J.-P. Raskin and D. Flandre, "Impact of Electrical Initialization Step on Transition Voltage and Power of Vanadium Dioxide Memristors", in *Applied Physics Letters*, 2026.

Bibliography

[1] A. Fiorillo, C. Critello, and S. Pullano, "Theory, technology and applications of piezoresistive sensors: A review," *Sensors and Actuators A: Physical*, vol. 281, pp. 156–175, Oct. 2018. [Online]. Available: https://linkinghub.elsevier.com/retrieve/pii/S0924424718308434

[2] L. Tang, S. Wu, J. Qu, L. Gong, and J. Tang, "A Review of Conductive Hydrogel Used in Flexible Strain Sensor," *Materials*, vol. 13, no. 18, p. 3947, Sep. 2020. [Online]. Available: https://www.mdpi.com/1996-1944/13/18/3947

[3] I. Graz, M. Krause, S. Bauer-Gogonea, S. Bauer, S. P. Lacour, B. Ploss, M. Zirkl, B. Stadlober, and S. Wagner, "Flexible active-matrix cells with selectively poled bifunctional polymer-ceramic nanocomposite for pressure and temperature sensing skin," *Journal of Applied Physics*, vol. 106, no. 3, p. 034503, Aug. 2009. [Online]. Available: https://pubs.aip.org/jap/article/106/3/034503/370438/Flexible-active-matrix-cells-with-selectively

[4] A. D. B. Ferreira, P. R. Nóvoa, and A. T. Marques, "Multifunctional Material Systems: A state-of-the-art review," *Composite Structures*, vol. 151, pp. 3–35, Sep. 2016. [Online]. Available: https://linkinghub.elsevier.com/retrieve/pii/S0263822316000416

[5] W. Chen and X. Yan, "Progress in achieving high-performance piezoresistive and capacitive flexible pressure sensors: A review," *Journal of Materials Science & Technology*, vol. 43, pp. 175–188, Apr. 2020. [Online]. Available: https://linkinghub.elsevier.com/retrieve/pii/S100503022030044X

[6] M. Chao, P. Di, Y. Yuan, Y. Xu, L. Zhang, and P. Wan, "Flexible breathable photothermal-therapy epidermic sensor with

MXene for ultrasensitive wearable human-machine interaction," *Nano Energy*, vol. 108, p. 108201, Apr. 2023. [Online]. Available: https://linkinghub.elsevier.com/retrieve/pii/S221128552300037X

[7] T. Someya, T. Sekitani, S. Iba, Y. Kato, H. Kawaguchi, and T. Sakurai, "A large-area, flexible pressure sensor matrix with organic field-effect transistors for artificial skin applications," *Proceedings of the National Academy of Sciences*, vol. 101, no. 27, pp. 9966–9970, Jul. 2004. [Online]. Available: https://pnas.org/doi/full/10.1073/pnas.0401918101

[8] T. Sekitani, U. Zschieschang, H. Klauk, and T. Someya, "Flexible organic transistors and circuits with extreme bending stability," *Nature Materials*, vol. 9, no. 12, pp. 1015–1022, Dec. 2010. [Online]. Available: https://www.nature.com/articles/nmat2896

[9] S. Xu, Y. Zhang, L. Jia, K. E. Mathewson, K.-I. Jang, J. Kim, H. Fu, X. Huang, P. Chava, R. Wang, S. Bhole, L. Wang, Y. J. Na, Y. Guan, M. Flavin, Z. Han, Y. Huang, and J. A. Rogers, "Soft Microfluidic Assemblies of Sensors, Circuits, and Radios for the Skin," *Science*, vol. 344, no. 6179, pp. 70–74, Apr. 2014. [Online]. Available: https://www.science.org/doi/10.1126/science.1250169

[10] Z. Chen, Z. Wang, X. Li, Y. Lin, N. Luo, M. Long, N. Zhao, and J.-B. Xu, "Flexible Piezoelectric-Induced Pressure Sensors for Static Measurements Based on Nanowires/Graphene Heterostructures," *ACS Nano*, vol. 11, no. 5, pp. 4507–4513, May 2017. [Online]. Available: https://pubs.acs.org/doi/10.1021/acsnano.6b08027

[11] T. Someya, Y. Kato, T. Sekitani, S. Iba, Y. Noguchi, Y. Murase, H. Kawaguchi, and T. Sakurai, "Conformable, flexible, large-area networks of pressure and thermal sensors with organic transistor active matrixes," *Proceedings of the National Academy of Sciences*, vol. 102, no. 35, pp. 12 321–12 325, Aug. 2005. [Online]. Available: https://pnas.org/doi/full/10.1073/pnas.0502392102

[12] J. Chen, J. Zheng, Q. Gao, J. Zhang, J. Zhang, O. Omisore, L. Wang, and H. Li, "Polydimethylsiloxane (PDMS)-Based Flexible Resistive Strain Sensors for Wearable Applications," *Applied Sciences*, vol. 8, no. 3, p. 345, Feb. 2018. [Online]. Available: https://www.mdpi.com/2076-3417/8/3/345

[13] L. Duan, D. R. D'hooge, and L. Cardon, "Recent progress on flexible and stretchable piezoresistive strain sensors: From design to application," *Progress in Materials Science*, vol. 114, p. 100617, Oct. 2020. [Online]. Available: https://linkinghub.elsevier.com/retrieve/pii/S0079642519300994

[14] M. Amjadi, K. Kyung, I. Park, and M. Sitti, "Stretchable, Skin-Mountable, and Wearable Strain Sensors and Their Potential Applications: A Review," *Advanced Functional Materials*, vol. 26, no. 11, pp. 1678–1698, Mar. 2016. [Online]. Available: https://advanced.onlinelibrary.wiley.com/doi/10.1002/adfm.201504755

[15] R. Fu, X. Zhao, X. Zhang, and Z. Su, "Design strategies and applications of wearable piezoresistive strain sensors with dimensionality-based conductive network structures," *Chemical Engineering Journal*, vol. 454, p. 140467, Feb. 2023. [Online]. Available: https://linkinghub.elsevier.com/retrieve/pii/S1385894722059472

[16] J. Li, L. Fang, B. Sun, X. Li, and S. H. Kang, "Review—Recent Progress in Flexible and Stretchable Piezoresistive Sensors and Their Applications," *Journal of The Electrochemical Society*, vol. 167, no. 3, p. 037561, Jan. 2020. [Online]. Available: https://iopscience.iop.org/article/10.1149/1945-7111/ab6828

[17] X. Cao, Y. Xiong, J. Sun, X. Zhu, Q. Sun, and Z. L. Wang, "Piezoelectric Nanogenerators Derived Self-Powered Sensors for Multifunctional Applications and Artificial Intelligence," *Advanced Functional Materials*, vol. 31, no. 33, p. 2102983, Aug. 2021. [Online]. Available: https://advanced.onlinelibrary.wiley.com/doi/10.1002/adfm.202102983

[18] W. Wu, "Anti-Crosstalk Materials and Structural Decoupling Strategies for Multimodal Flexible Sensors," *Advanced Functional Materials*, vol. 36, no. 25, p. e24222, Mar. 2026. [Online]. Available: https://advanced.onlinelibrary.wiley.com/doi/10.1002/adfm.202524222

[19] J. Tao, J. Huang, J. Tong, J. Xu, S. Ma, R. Bao, X. Wu, S. Ding, and C. Pan, "Deep Learning-Enabled Self-Powered Stretchable Triboelectric Sensor Array for Intelligent Posture Monitoring and Regulation," *Advanced Functional Materials*, vol. 36, no. 16, p. e14646,

Feb. 2026. [Online]. Available: https://advanced.onlinelibrary.wiley.com/doi/10.1002/adfm.202514646

[20] Z. Chen, Y. Jin, Z. Li, B. Wang, B. Liu, B. Xu, F. Gong, L. Jiang, and H. Li, "An AI-Powered, All-Printed, Scalable, Stretchable Triboelectric E-Skin for Multifunctional Perception in Dexterous Hand," *Advanced Functional Materials*, vol. 36, no. 35, p. e27673, Apr. 2026. [Online]. Available: https://advanced.onlinelibrary.wiley.com/doi/10.1002/adfm.202527673

[21] C. Wu, X. Gao, H. Zhu, X. Wang, S. Wang, Y. Fu, Y. Han, W. Yuan, Y. Tian, X. Jiang, and W. Lai, "Multiscale Stress Transmission Regulation toward Flexible Strain Sensors with High Stability," *Advanced Functional Materials*, vol. 36, no. 5, p. e10852, Jan. 2026. [Online]. Available: https://advanced.onlinelibrary.wiley.com/doi/10.1002/adfm.202510852

[22] Y. Song, Y. Li, Y. Wang, C. Ye, C. Zhu, and R. Yang, "Artificial Intelligence Powered Smart Multimodal Hand-Wearable Systems for Healthcare and Human–Machine Interaction," *Advanced Functional Materials*, vol. 36, no. 36, p. e32014, May 2026. [Online]. Available: https://advanced.onlinelibrary.wiley.com/doi/10.1002/adfm.202532014

[23] Y. Xu, X. Liang, Z. Hu, X. Yang, Z. Sun, L. Lu, G. Zu, and J. Huang, "Bioinspired Stretchable Multi-Modal Self-Powered Aerogel-Based Pressure/Gas/Temperature-Sensitive Electronic Skins," *Advanced Functional Materials*, p. e00013, Mar. 2026. [Online]. Available: https://advanced.onlinelibrary.wiley.com/doi/10.1002/adfm.202600013

[24] D. Quiquero, R. Noroozi, K. Wang, R. Conliffe, and H. H. Shi, "Evolving Beyond Nature: AI-Driven Rapid Advancements of Bio-Inspired Electronic Skin," *ACS Applied Materials & Interfaces*, vol. 18, no. 13, pp. 18 625–18 657, Apr. 2026. [Online]. Available: https://pubs.acs.org/doi/10.1021/acsami.5c24192

[25] A. Damilano, A. Lince, S. Appendino, H. M. A. Hayat, P. Ariano, D. Demarchi, and M. Crepaldi, "Commercial tactile sensors for hand exoskeletons: practical considerations for ultra-low cost and very-low complexity read-out," *IEEE Instrumentation & Measurement Magazine*, vol. 19, no. 5, pp. 49–56, Oct. 2016. [Online]. Available: http://ieeexplore.ieee.org/document/7579070/

[26] S. Cheng, Y. S. Narang, C. Yang, Z. Suo, and R. D. Howe, "Stick-On Large-Strain Sensors for Soft Robots," *Advanced Materials Interfaces*, vol. 6, no. 20, p. 1900985, Oct. 2019. [Online]. Available: https://advanced.onlinelibrary.wiley.com/doi/10.1002/admi.201900985

[27] H. Yang and W. Wu, "A review: Machine learning for strain sensor-integrated soft robots," *Frontiers in Electronic Materials*, vol. 2, p. 1000781, Nov. 2022. [Online]. Available: https://www.frontiersin.org/articles/10.3389/femat.2022.1000781/full

[28] Q. Liu, Z. Peng, C. Sun, and H. Yang, "Recent advances in multifunctional soft robots: A materials–structures–systems co-design perspective for synergistic integration," *FlexMat*, p. flm2.70053, Mar. 2026. [Online]. Available: https://onlinelibrary.wiley.com/doi/10.1002/flm2.70053

[29] H. Yousef, M. Boukallel, and K. Althoefer, "Tactile sensing for dexterous in-hand manipulation in robotics—A review," *Sensors and Actuators A: Physical*, vol. 167, no. 2, pp. 171–187, Jun. 2011. [Online]. Available: https://linkinghub.elsevier.com/retrieve/pii/S0924424711001105

[30] H. Jeon, S. K. Hong, M. S. Kim, S. J. Cho, and G. Lim, "Omni-Purpose Stretchable Strain Sensor Based on a Highly Dense Nanocracking Structure for Whole-Body Motion Monitoring," *ACS Applied Materials & Interfaces*, vol. 9, no. 48, pp. 41 712–41 721, Dec. 2017. [Online]. Available: https://pubs.acs.org/doi/10.1021/acsami.7b14153

[31] J. Wang, C. Lu, and K. Zhang, "Textile-Based Strain Sensor for Human Motion Detection," *ENERGY & ENVIRONMENTAL MATERIALS*, vol. 3, no. 1, pp. 80–100, Mar. 2020. [Online]. Available: https://onlinelibrary.wiley.com/doi/10.1002/eem2.12041

[32] Y. Wang, L. Wang, T. Yang, X. Li, X. Zang, M. Zhu, K. Wang, D. Wu, and H. Zhu, "Wearable and Highly Sensitive Graphene Strain Sensors for Human Motion Monitoring," *Advanced Functional Materials*, vol. 24, no. 29, pp. 4666–4670, Aug. 2014. [Online]. Available: https://advanced.onlinelibrary.wiley.com/doi/10.1002/adfm.201400379

[33] S. G. Yoon, H.-J. Koo, and S. T. Chang, "Highly Stretchable and Transparent Microfluidic Strain Sensors for Monitoring Human Body Motions," *ACS Applied Materials & Interfaces*,

vol. 7, no. 49, pp. 27 562–27 570, Dec. 2015. [Online]. Available: https://pubs.acs.org/doi/10.1021/acsami.5b08404

[34] X. Liu, Y. Wei, and Y. Qiu, "Advanced Flexible Skin-Like Pressure and Strain Sensors for Human Health Monitoring," *Micromachines*, vol. 12, no. 6, p. 695, Jun. 2021. [Online]. Available: https://www.mdpi.com/2072-666X/12/6/695

[35] T. Yang, X. Jiang, Y. Zhong, X. Zhao, S. Lin, J. Li, X. Li, J. Xu, Z. Li, and H. Zhu, "A Wearable and Highly Sensitive Graphene Strain Sensor for Precise Home-Based Pulse Wave Monitoring," *ACS Sensors*, vol. 2, no. 7, pp. 967–974, Jul. 2017. [Online]. Available: https://pubs.acs.org/doi/10.1021/acssensors.7b00230

[36] S. Li, H. Wang, W. Ma, L. Qiu, K. Xia, Y. Zhang, H. Lu, M. Zhu, X. Liang, X.-E. Wu, H. Liang, and Y. Zhang, "Monitoring blood pressure and cardiac function without positioning via a deep learning–assisted strain sensor array," *Science Advances*, vol. 9, no. 32, p. eadh0615, Aug. 2023. [Online]. Available: https://www.science.org/doi/10.1126/sciadv.adh0615

[37] S. A. Dual, B. Llerena Zambrano, S. Sündermann, N. Cesarovic, M. Kron, K. Magkoutas, J. Hengsteler, V. Falk, C. Starck, M. Meboldt, J. Vörös, and M. Schmid Daners, "Continuous Heart Volume Monitoring by Fully Implantable Soft Strain Sensor," *Advanced Healthcare Materials*, vol. 9, no. 19, p. 2000855, Oct. 2020. [Online]. Available: https://advanced.onlinelibrary.wiley.com/doi/10.1002/adhm.202000855

[38] Y. Shen, W. Yang, F. Hu, X. Zheng, Y. Zheng, H. Liu, H. Algadi, and K. Chen, "Ultrasensitive wearable strain sensor for promising application in cardiac rehabilitation," *Advanced Composites and Hybrid Materials*, vol. 6, no. 1, p. 21, Feb. 2023. [Online]. Available: https://link.springer.com/10.1007/s42114-022-00610-3

[39] R. Herbert, H.-R. Lim, and W.-H. Yeo, "Printed, Soft, Nanostructured Strain Sensors for Monitoring of Structural Health and Human Physiology," *ACS Applied Materials & Interfaces*, vol. 12, no. 22, pp. 25 020–25 030, Jun. 2020. [Online]. Available: https://pubs.acs.org/doi/10.1021/acsami.0c04857

[40] J. Li, L. Fang, B. Sun, X. Li, and S. H. Kang, "Review—Recent Progress in Flexible and Stretchable Piezoresistive Sensors and Their Applications," *Journal of The Electrochemical Society*, vol. 167, no. 3, p. 037561, Jan. 2020. [Online]. Available: https://iopscience.iop.org/article/10.1149/1945-7111/ab6828

[41] R. Fu, X. Zhao, X. Zhang, and Z. Su, "Design strategies and applications of wearable piezoresistive strain sensors with dimensionality-based conductive network structures," *Chemical Engineering Journal*, vol. 454, p. 140467, Feb. 2023. [Online]. Available: https://linkinghub.elsevier.com/retrieve/pii/S1385894722059472

[42] W. Chen and X. Yan, "Progress in achieving high-performance piezoresistive and capacitive flexible pressure sensors: A review," *Journal of Materials Science & Technology*, vol. 43, pp. 175–188, Apr. 2020. [Online]. Available: https://linkinghub.elsevier.com/retrieve/pii/S100503022030044X

[43] T. Dong, Y. Gu, T. Liu, and M. Pecht, "Resistive and capacitive strain sensors based on customized compliant electrode: Comparison and their wearable applications," *Sensors and Actuators A: Physical*, vol. 326, p. 112720, Aug. 2021. [Online]. Available: https://linkinghub.elsevier.com/retrieve/pii/S0924424721001837

[44] Y. Zeng, Y. Qin, Y. Yang, and X. Lu, "A Low-Cost Flexible Capacitive Pressure Sensor for Health Detection," *IEEE Sensors Journal*, vol. 22, no. 8, pp. 7665–7673, Apr. 2022. [Online]. Available: https://ieeexplore.ieee.org/document/9732486/

[45] Min-Xin Zhou, Qing-An Huang, Ming Qin, and Wei Zhou, "A novel capacitive pressure sensor based on sandwich structures," *Journal of Microelectromechanical Systems*, vol. 14, no. 6, pp. 1272–1282, Dec. 2005. [Online]. Available: http://ieeexplore.ieee.org/document/1549862/

[46] S. Ma, J. Tang, T. Yan, and Z. Pan, "Performance of Flexible Strain Sensors With Different Transition Mechanisms: A Review," *IEEE Sensors Journal*, vol. 22, no. 8, pp. 7475–7498, Apr. 2022. [Online]. Available: https://ieeexplore.ieee.org/document/9726149/

[47] S. Stassi, V. Cauda, G. Canavese, and C. Pirri, "Flexible Tactile Sensing Based on Piezoresistive Composites: A Review," *Sensors*,

vol. 14, no. 3, pp. 5296–5332, Mar. 2014. [Online]. Available: https://www.mdpi.com/1424-8220/14/3/5296

[48] L. Duan, D. R. D'hooge, and L. Cardon, "Recent progress on flexible and stretchable piezoresistive strain sensors: From design to application," *Progress in Materials Science*, vol. 114, p. 100617, Oct. 2020. [Online]. Available: https://linkinghub.elsevier.com/retrieve/pii/S0079642519300994

[49] Y. He, X. Xu, S. Xiao, J. Wu, P. Zhou, L. Chen, and H. Liu, "Research Progress and Application of Multimodal Flexible Sensors for Electronic Skin," *ACS Sensors*, vol. 9, no. 5, pp. 2275–2293, May 2024. [Online]. Available: https://pubs.acs.org/doi/10.1021/acssensors.4c00307

[50] F. Zeng, Q. Wang, Q. Mo, Q. Zheng, H. Zhan, and J. Pei, "Intelligent Multimodal Sensors Based on Two-Dimensional Materials: Fabrication, Decoupling, and Applications," *Small*, vol. 22, no. 42, p. e74106, Jul. 2026. [Online]. Available: https://onlinelibrary.wiley.com/doi/10.1002/smll.74106

[51] C. S. Smith, "Piezoresistance Effect in Germanium and Silicon," *Physical Review*, vol. 94, no. 1, pp. 42–49, Apr. 1954.

[52] Y. Kanda, "Piezoresistance effect of silicon," *Sensors and Actuators A-physical*, vol. 28, pp. 83–91, 1991. [Online]. Available: https://api.semanticscholar.org/CorpusID:95848036

[53] S. Yang and N. Lu, "Gauge Factor and Stretchability of Silicon-on-Polymer Strain Gauges," *Sensors*, vol. 13, no. 7, pp. 8577–8594, Jul. 2013. [Online]. Available: https://www.mdpi.com/1424-8220/13/7/8577

[54] N. Gupta, V. Adepu, M. Tathacharya, S. Siraj, S. Pal, P. Sahatiya, and B. K. Kuila, "Piezoresistive pressure sensor based on conjugated polymer framework for pedometer and smart tactile glove applications," *Sensors and Actuators A: Physical*, vol. 350, p. 114139, Feb. 2023. [Online]. Available: https://linkinghub.elsevier.com/retrieve/pii/S0924424722007749

[55] V. Sankar, A. Nambi, V. N. Bhat, D. Sethy, K. Balasubramaniam, S. Das, M. Guha, and R. Sundara, "Waterproof Flexible Polymer-Functionalized Graphene-Based Piezoresistive Strain Sensor for

Structural Health Monitoring and Wearable Devices," *ACS Omega*, vol. 5, no. 22, pp. 12 682–12 691, Jun. 2020. [Online]. Available: https://pubs.acs.org/doi/10.1021/acsomega.9b04205

[56] S. Nauman, "Piezoresistive Sensing Approaches for Structural Health Monitoring of Polymer Composites—A Review," *Eng*, vol. 2, no. 2, pp. 197–226, May 2021. [Online]. Available: https://www.mdpi.com/2673-4117/2/2/13

[57] A. Saxena and K. Patra, "Recent developments in stretchable and flexible tactile sensors towards piezoresistive systems: A review," *Polymers for Advanced Technologies*, vol. 35, no. 1, p. e6251, Jan. 2024. [Online]. Available: https://onlinelibrary.wiley.com/doi/10.1002/pat.6251

[58] T. Chen, L. Ma, R. Gong, H. Huang, F. Wang, and J. Huang, "Advanced Design of Next-Generation Piezoresistive Sensors with Tailored Microstructures for Digital Healthcare," *ACS Sensors*, vol. 10, no. 11, pp. 8170–8194, Nov. 2025. [Online]. Available: https://pubs.acs.org/doi/10.1021/acssensors.5c02599

[59] C. V. Le and H. Yoon, "Advances in the Use of Conducting Polymers for Healthcare Monitoring," *International Journal of Molecular Sciences*, vol. 25, no. 3, p. 1564, Jan. 2024. [Online]. Available: https://www.mdpi.com/1422-0067/25/3/1564

[60] E. Pimentel, P. Costa, J. Vilaça, C. Costa, S. Lanceros-Méndez, and D. Miranda, "Piezoresistive materials based on natural polymers for medical device applications," *Reactive and Functional Polymers*, vol. 217, p. 106502, Dec. 2025. [Online]. Available: https://linkinghub.elsevier.com/retrieve/pii/S1381514825003542

[61] F. Zhao, Y. Zhao, H. Cheng, and L. Qu, "A Graphene Fibriform Responsor for Sensing Heat, Humidity, and Mechanical Changes," *Angewandte Chemie International Edition*, vol. 54, no. 49, pp. 14 951–14 955, Dec. 2015. [Online]. Available: https://onlinelibrary.wiley.com/doi/10.1002/anie.201508300

[62] T. Nezakati, A. Seifalian, A. Tan, and A. M. Seifalian, "Conductive Polymers: Opportunities and Challenges in Biomedical Applications," *Chemical Reviews*, vol. 118, no. 14, pp. 6766–6843, Jul. 2018. [Online]. Available: https://pubs.acs.org/doi/10.1021/acs.chemrev.6b00275

[63] N. A. Mohd Radzuan, A. B. Sulong, and J. Sahari, "A review of electrical conductivity models for conductive polymer composite," *International Journal of Hydrogen Energy*, vol. 42, no. 14, pp. 9262–9273, Apr. 2017. [Online]. Available: https://linkinghub.elsevier.com/retrieve/pii/S0360319915310296

[64] X.-S. Yi, G. Wu, and Y. Pan, "Properties and applications of filled conductive polymer composites," *Polymer International*, vol. 44, no. 2, pp. 117–124, Oct. 1997. [Online]. Available: https://onlinelibrary.wiley.com/doi/10.1002/(SICI)1097-0126(199710)44:2<117::AID-PI811>3.0.CO;2-L

[65] G. Kaur, R. Adhikari, P. Cass, M. Bown, and P. Gunatillake, "Electrically conductive polymers and composites for biomedical applications," *RSC Advances*, vol. 5, no. 47, pp. 37 553–37 567, 2015. [Online]. Available: https://xlink.rsc.org/?DOI=C5RA01851J

[66] Y. Wang, A. Liu, Y. Han, and T. Li, "Sensors based on conductive polymers and their composites: a review," *Polymer International*, vol. 69, no. 1, pp. 7–17, Jan. 2020. [Online]. Available: https://scijournals.onlinelibrary.wiley.com/doi/10.1002/pi.5907

[67] B. Amna and T. Ozturk, "Organic field-effect transistor-based sensors: recent progress, challenges and future outlook," *Journal of Materials Chemistry C*, vol. 13, no. 17, pp. 8354–8424, 2025. [Online]. Available: https://xlink.rsc.org/?DOI=D4TC04265D

[68] Z. A. Lamport, M. R. Cavallari, K. A. Kam, C. K. McGinn, C. Yu, and I. Kymissis, "Organic Thin Film Transistors in Mechanical Sensors," *Advanced Functional Materials*, vol. 30, no. 51, p. 2004700, Dec. 2020. [Online]. Available: https://advanced.onlinelibrary.wiley.com/doi/10.1002/adfm.202004700

[69] D. Thuau, M. Abbas, G. Wantz, L. Hirsch, I. Dufour, and C. Ayela, "Piezoelectric polymer gated OFET: Cutting-edge electro-mechanical transducer for organic MEMS-based sensors," *Scientific Reports*, vol. 6, no. 1, p. 38672, Dec. 2016. [Online]. Available: https://www.nature.com/articles/srep38672

[70] Z. Wang, S. Guo, H. Li, B. Wang, Y. Sun, Z. Xu, X. Chen, K. Wu, X. Zhang, F. Xing, L. Li, and W. Hu, "The Semiconductor/Conductor Interface Piezoresistive Effect in an Organic Transistor for Highly

Sensitive Pressure Sensors," *Advanced Materials*, vol. 31, no. 6, p. 1805630, Feb. 2019. [Online]. Available: https://advanced.onlinelibrary.wiley.com/doi/10.1002/adma.201805630

[71] K. V. Meena and A. R. Sankar, "Biomedical Catheters With Integrated Miniature Piezoresistive Pressure Sensors: A Review," *IEEE Sensors Journal*, vol. 21, no. 9, pp. 10 241–10 290, May 2021. [Online]. Available: https://ieeexplore.ieee.org/document/9347467/

[72] Y. Wang, J. Guo, D. Xu, Z. Gu, and Y. Zhao, "Micro-/nano-structured flexible electronics for biomedical applications," *Biomedical Technology*, vol. 2, pp. 1–14, Jun. 2023. [Online]. Available: https://linkinghub.elsevier.com/retrieve/pii/S2949723X22000150

[73] S. Lyu and D. Untereker, "Degradability of Polymers for Implantable Biomedical Devices," *International Journal of Molecular Sciences*, vol. 10, no. 9, pp. 4033–4065, Sep. 2009. [Online]. Available: https://www.mdpi.com/1422-0067/10/9/4033

[74] "Technology Roadmap for Flexible Sensors," *ACS Nano*, vol. 17, no. 6, pp. 5211–5295, Mar. 2023. [Online]. Available: https://pubs.acs.org/doi/10.1021/acsnano.2c12606

[75] Z. Wang, T. Zhang, L. Zhang, X. Wang, Y. Yao, Q. Liu, Y. Liu, and D. Chen, "Deep Learning-Based Prediction and Compensation of Performance Degradation in Flexible Sensors," *Micromachines*, vol. 17, no. 4, p. 496, Apr. 2026. [Online]. Available: https://www.mdpi.com/2072-666X/17/4/496

[76] J. Li, Z. Yao, X. Meng, X. Zhang, Z. Wang, J. Wang, G. Ma, L. Liu, J. Zhang, S. Niu, Z. Han, and L. Ren, "High-Fidelity, Low-Hysteresis Bionic Flexible Strain Sensors for Soft Machines," *ACS Nano*, vol. 18, no. 3, pp. 2520–2530, Jan. 2024. [Online]. Available: https://pubs.acs.org/doi/10.1021/acsnano.3c11711

[77] M. Amjadi, A. Pichitpajongkit, S. Lee, S. Ryu, and I. Park, "Highly Stretchable and Sensitive Strain Sensor Based on Silver Nanowire–Elastomer Nanocomposite," *ACS Nano*, vol. 8, no. 5, pp. 5154–5163, May 2014. [Online]. Available: https://pubs.acs.org/doi/10.1021/nn501204t

[78] D. Corzo, G. Tostado-Blázquez, and D. Baran, "Flexible Electronics: Status, Challenges and Opportunities," *Frontiers in Electronics*, vol. 1, p. 594003, Sep. 2020. [Online]. Available: https://www.frontiersin.org/article/10.3389/felec.2020.594003/full

[79] J. J. Petronienė, A. Dzedzickis, I. Morkvėnaitė-Vilkončienė, and V. Bučinskas, "Flexible strain sensors: Recent progress 2016-2023," *Sensors and Actuators A: Physical*, vol. 366, p. 114950, Feb. 2024. [Online]. Available: https://linkinghub.elsevier.com/retrieve/pii/S0924424723007999

[80] M. Takakuwa, K. Yamagishi, S. Lee, Y. Tagawa, T. Someya, and T. Yokota, "Device Integration Technology for Practical Flexible Electronics Systems," *Advanced Functional Materials*, vol. 36, no. 13, p. e14330, Feb. 2026. [Online]. Available: https://advanced.onlinelibrary.wiley.com/doi/10.1002/adfm.202514330

[81] M. Xie, K. Hisano, M. Zhu, T. Toyoshi, M. Pan, S. Okada, O. Tsutsumi, S. Kawamura, and C. Bowen, "Flexible Multifunctional Sensors for Wearable and Robotic Applications," *Advanced Materials Technologies*, vol. 4, no. 3, p. 1800626, Mar. 2019. [Online]. Available: https://advanced.onlinelibrary.wiley.com/doi/10.1002/admt.201800626

[82] J. Lee, K. Cho, and J. Kim, "Age of Flexible Electronics: Emerging Trends in Soft Multifunctional Sensors," *Advanced Materials*, vol. 36, no. 16, p. 2310505, Apr. 2024. [Online]. Available: https://advanced.onlinelibrary.wiley.com/doi/10.1002/adma.202310505

[83] M. Mansoor, I. Haneef, S. Akhtar, A. De Luca, and F. Udrea, "Silicon diode temperature sensors—A review of applications," *Sensors and Actuators A: Physical*, vol. 232, pp. 63–74, Aug. 2015. [Online]. Available: https://linkinghub.elsevier.com/retrieve/pii/S0924424715002137

[84] R. Gounella, G. M. Ferreira, M. L. M. Amorim, J. N. Soares, and J. P. Carmo, "A Review of Optical Sensors in CMOS," *Electronics*, vol. 13, no. 4, p. 691, Feb. 2024. [Online]. Available: https://www.mdpi.com/2079-9292/13/4/691

[85] T. P. Delhaye, N. Andre, L. A. Francis, and D. Flandre, "New Universal Figure of Merit for Embedded Si Piezoresistive Pressure

Sensors," *IEEE Sensors Journal*, pp. 1–1, 2020. [Online]. Available: https://ieeexplore.ieee.org/document/9153028/

[86] X. Zeng, N. André, E. Masarweh, O. Bonfanti, and D. Flandre, "Electromechanical Measurements and Modeling of a High-Performance Small-Area Ultra-Thin SOI MEMS Piezoresistive Pressure Sensor," *IEEE Transactions on Instrumentation and Measurement*, vol. 74, pp. 1–9, 2025. [Online]. Available: https://ieeexplore.ieee.org/document/10985850/

[87] D. Meng, H. Zhao, X. Wu, M. Liu, and Q. Guo, "Silicon Nanomembrane Based Flexible Temperature-Bending Strain Dual-Mode Sensor Decoupled by Fast Fourier Transform," *IEEE Electron Device Letters*, vol. 45, no. 12, pp. 2518–2521, Dec. 2024. [Online]. Available: https://ieeexplore.ieee.org/document/10718338/

[88] J. Mireles Jr., A. Jiménez, and A. Sauceda, "SOI-Structured Piezoresistive Pressure Sensor with Integration of Temperature Sensor for Downhole Applications," *Sensors*, vol. 26, no. 7, p. 2076, Mar. 2026. [Online]. Available: https://www.mdpi.com/1424-8220/26/7/2076

[89] F. Liao, C. Lu, G. Yao, Z. Yan, M. Gao, T. Pan, Y. Zhang, X. Feng, and Y. Lin, "Ultrasensitive Flexible Temperature-Mechanical Dual-Parameter Sensor Based on Vanadium Dioxide Films," *IEEE Electron Device Letters*, vol. 38, no. 8, pp. 1128–1131, Aug. 2017. [Online]. Available: http://ieeexplore.ieee.org/document/7945269/

[90] Y. Ke, S. Wang, G. Liu, M. Li, T. J. White, and Y. Long, "Vanadium Dioxide: The Multistimuli Responsive Material and Its Applications," *Small*, vol. 14, no. 39, p. 1802025, Sep. 2018. [Online]. Available: https://onlinelibrary.wiley.com/doi/10.1002/smll.201802025

[91] R. Yuan, Q. Duan, P. J. Tiw, G. Li, Z. Xiao, Z. Jing, K. Yang, C. Liu, C. Ge, R. Huang, and Y. Yang, "A calibratable sensory neuron based on epitaxial VO2 for spike-based neuromorphic multisensory system," *Nature Communications*, vol. 13, no. 1, p. 3973, Jul. 2022. [Online]. Available: https://www.nature.com/articles/s41467-022-31747-w

[92] X. Zhou, "Recent advances in multi-field manipulations of the metal–insulator transition in correlated vanadium oxides enabling interdisciplinary applications," *Journal of Materials Chemistry*

C, vol. 13, no. 7, pp. 3123–3144, 2025. [Online]. Available: https://pubs.rsc.org/tc/article/13/7/3123-3144/878565

[93] Q. Duan, T. Zhang, C. Liu, R. Yuan, G. Li, P. Jun Tiw, K. Yang, C. Ge, Y. Yang, and R. Huang, "Artificial Multisensory Neurons with Fused Haptic and Temperature Perception for Multimodal In-Sensor Computing," *Advanced Intelligent Systems*, vol. 4, no. 8, p. 2200039, Aug. 2022. [Online]. Available: https://advanced.onlinelibrary.wiley.com/doi/10.1002/aisy.202200039

[94] S. L. Fang, C. Y. Han, W. Liu, Z. R. Han, B. Ma, Y. L. Cui, S. Q. Fan, X. Li, X. L. Wang, G. H. Zhang, J. Q. Yin, X. D. Huang, and L. Geng, "A bioinspired flexible artificial mechanoreceptor based on VO2 insulator-metal transition memristor," *Journal of Alloys and Compounds*, vol. 911, p. 165096, Aug. 2022. [Online]. Available: https://linkinghub.elsevier.com/retrieve/pii/S0925838822014876

[95] J. Zhu, X. Zhang, R. Wang, M. Wang, P. Chen, L. Cheng, Z. Wu, Y. Wang, Q. Liu, and M. Liu, "A Heterogeneously Integrated Spiking Neuron Array for Multimode-Fused Perception and Object Classification," *Advanced Materials*, vol. 34, no. 24, p. 2200481, Jun. 2022. [Online]. Available: https://advanced.onlinelibrary.wiley.com/doi/10.1002/adma.202200481

[96] Q. Xia, Y. Qin, A. Zheng, P. Qiu, and X. Zhang, "A Multifunctional Biomimetic Flexible Sensor Based Novel Artificial Tactile Neuron with Perceptual Memory," *Advanced Materials Interfaces*, vol. 8, no. 23, p. 2101068, Dec. 2021. [Online]. Available: https://advanced.onlinelibrary.wiley.com/doi/10.1002/admi.202101068

[97] X. Zeng, T. Ratier, R. Puyol, L. Van Brandt, and D. Flandre, "VO 2 -based energy-efficient artificial spiking sensor emulating human-skin-like high-precision temperature perception," *Physical Review Applied*, vol. 26, no. 2, p. 024052, Aug. 2026. [Online]. Available: https://link.aps.org/doi/10.1103/qksb-q166

[98] T. Yuan, R. Yin, C. Li, Z. Fan, and L. Pan, "Ti3C2Tx MXene-based all-resistive dual-mode sensor with near-zero temperature coefficient of resistance for crosstalk-free pressure and temperature detections," *Chemical Engineering Journal*, vol. 487, p. 150396, May 2024. [Online]. Available: https://linkinghub.elsevier.com/retrieve/pii/S1385894724018837

[99] Y. Cao, Y. Guo, Z. Chen, W. Yang, K. Li, X. He, and J. Li, "Highly sensitive self-powered pressure and strain sensor based on crumpled MXene film for wireless human motion detection," *Nano Energy*, vol. 92, p. 106689, Feb. 2022. [Online]. Available: https://linkinghub.elsevier.com/retrieve/pii/S2211285521009393

[100] K. Wang, J.-N. Ma, Q. Zhao, J.-H. Zhang, K.-D. Zhang, Y. Zhang, L. Wang, and S.-B. Sang, "Ti3C2Tx MXene-based multifunctional wearable integrated sensor for simultaneous detection of humidity and pressure stimuli," *Sensors and Actuators B: Chemical*, vol. 442, p. 138147, Nov. 2025. [Online]. Available: https://linkinghub.elsevier.com/retrieve/pii/S0925400525009232

[101] M. Gao, B. Zhang, X. Du, X. Yang, C. Zhai, C. Chen, Z. Zhang, and W. Zhao, "InSe-Based Sensors and Related Sensing Systems for NO_2 Gas/Temperature Monitoring," *ACS Sensors*, vol. 10, no. 9, pp. 7124–7133, Sep. 2025. [Online]. Available: https://pubs.acs.org/doi/10.1021/acssensors.5c02421

[102] Q. Zhao, T. Wang, R. Frisenda, and A. Castellanos-Gomez, "Giant Piezoresistive Effect and Strong Bandgap Tunability in Ultrathin InSe upon Biaxial Strain," *Advanced Science*, vol. 7, no. 20, p. 2001645, Oct. 2020. [Online]. Available: https://advanced.onlinelibrary.wiley.com/doi/10.1002/advs.202001645

[103] H. Yu, Z. Hu, J. He, Y. Ran, Y. Zhao, Z. Yu, and K. Tai, "Flexible temperature-pressure dual sensor based on 3D spiral thermoelectric Bi2Te3 films," *Nature Communications*, vol. 15, no. 1, p. 2521, Mar. 2024. [Online]. Available: https://www.nature.com/articles/s41467-024-46836-1

[104] Q. Li, T. Wu, W. Zhao, J. Ji, and G. Wang, "Laser-Induced Corrugated Graphene Films for Integrated Multimodal Sensors," *ACS Applied Materials & Interfaces*, vol. 13, no. 31, pp. 37 433–37 444, Aug. 2021. [Online]. Available: https://pubs.acs.org/doi/10.1021/acsami.1c12686

[105] D. H. Ho, Q. Sun, S. Y. Kim, J. T. Han, D. H. Kim, and J. H. Cho, "Stretchable and Multimodal All Graphene Electronic Skin," *Advanced Materials*, vol. 28, no. 13, pp. 2601–2608, Apr. 2016. [Online]. Available: https://advanced.onlinelibrary.wiley.com/doi/10.1002/adma.201505739

[106] Q. Jia, W. Ye, C. Zhang, Z. Jia, J. Liu, T. Wang, L. Zhao, Y. Liu, C. Wang, P. Sun, Z. Fan, and G. Lu, "Wearable Multimodal Sensing System for Synchronously Health–Environmental Monitoring via Hybrid Neuroevolutionary Signal Decoupling," *Nano Letters*, vol. 25, no. 24, pp. 9726–9733, Jun. 2025. [Online]. Available: https://pubs.acs.org/doi/10.1021/acs.nanolett.5c01881

[107] Z. Chen, S. Liu, P. Kang, Y. Wang, H. Liu, C. Liu, and C. Shen, "Decoupled Temperature–Pressure Sensing System for Deep Learning Assisted Human–Machine Interaction," *Advanced Functional Materials*, vol. 34, no. 52, p. 2411688, Dec. 2024. [Online]. Available: https://advanced.onlinelibrary.wiley.com/doi/10.1002/adfm.202411688

[108] C. Bai, X. Dong, Q. Liu, M. Zhao, K. Yang, Y. Niu, H. Zhang, and W. Zhai, "A self-powered hydrogel electronic skin with decoupled multimodal sensing for closed-loop human-machine interactions," *Nature Communications*, vol. 17, no. 1, p. 2675, Feb. 2026. [Online]. Available: https://www.nature.com/articles/s41467-026-69450-9

[109] J. Lee, E. Kim, H. Zhang, H. Chen, H. Venkatesan, K. Chan, J. Yang, X. Shen, J. Yang, S. Jeon, and J. Kim, "Rational Design of All Resistive Multifunctional Sensors with Stimulus Discriminability," *Advanced Functional Materials*, vol. 32, no. 1, p. 2107570, Jan. 2022. [Online]. Available: https://advanced.onlinelibrary.wiley.com/doi/10.1002/adfm.202107570

[110] X. Yang, S. Lv, T. Li, S. Hao, H. Zhu, Y. Cheng, S. Li, and H. Song, "Dual Thermo-Responsive and Strain-Responsive Ionogels for Smart Windows and Temperature/Motion Monitoring," *ACS Applied Materials & Interfaces*, vol. 14, no. 17, pp. 20 083–20 092, May 2022. [Online]. Available: https://pubs.acs.org/doi/10.1021/acsami.2c03142

[111] M. Darwish, Y. Zhabura, and L. Pohl, "Recent Advances of VO2 in Sensors and Actuators," *Nanomaterials*, vol. 14, no. 7, p. 582, Mar. 2024. [Online]. Available: https://www.mdpi.com/2079-4991/14/7/582

[112] F. J. Morin, "Oxides Which Show a Metal-to-Insulator Transition at the Neel Temperature," *Physical Review Letters*, vol. 3, no. 1, pp. 34–36, Jul. 1959. [Online]. Available: https://link.aps.org/doi/10.1103/PhysRevLett.3.34

[113] Z. Shao, X. Cao, H. Luo, and P. Jin, "Recent progress in the phase-transition mechanism and modulation of vanadium dioxide materials," *NPG Asia Materials*, vol. 10, no. 7, pp. 581–605, Jul. 2018. [Online]. Available: http://www.nature.com/articles/s41427-018-0061-2

[114] Y. Choi, D. Lee, S. Song, J. Kim, T. Ju, H. Kim, J. Kim, S. Yoon, Y. Kim, T. B. Phan, J. Bae, and S. Park, "Correlation between Symmetry and Phase Transition Temperature of VO $_2$ Films Deposited on Al $_2$ O $_3$ Substrates with Various Orientations," *Advanced Electronic Materials*, vol. 7, no. 4, p. 2000874, Apr. 2021. [Online]. Available: https://onlinelibrary.wiley.com/doi/10.1002/aelm.202000874

[115] J. Cao, E. Ertekin, V. Srinivasan, W. Fan, S. Huang, H. Zheng, J. W. L. Yim, D. R. Khanal, D. F. Ogletree, J. C. Grossman, and J. Wu, "Strain engineering and one-dimensional organization of metal–insulator domains in single-crystal vanadium dioxide beams," *Nature Nanotechnology*, vol. 4, no. 11, pp. 732–737, Nov. 2009. [Online]. Available: http://www.nature.com/articles/nnano.2009.266

[116] J. Cao, Y. Gu, W. Fan, L. Q. Chen, D. F. Ogletree, K. Chen, N. Tamura, M. Kunz, C. Barrett, J. Seidel, and J. Wu, "Extended Mapping and Exploration of the Vanadium Dioxide Stress-Temperature Phase Diagram," *Nano Letters*, vol. 10, no. 7, pp. 2667–2673, Jul. 2010. [Online]. Available: https://pubs.acs.org/doi/10.1021/nl101457k

[117] B. Hu, Y. Ding, W. Chen, D. Kulkarni, Y. Shen, V. V. Tsukruk, and Z. L. Wang, "External-Strain Induced Insulating Phase Transition in VO_2 Nanobeam and Its Application as Flexible Strain Sensor," *Advanced Materials*, vol. 22, no. 45, pp. 5134–5139, Dec. 2010. [Online]. Available: https://advanced.onlinelibrary.wiley.com/doi/10.1002/adma.201002868

[118] Y. Gu, J. Cao, J. Wu, and L.-Q. Chen, "Thermodynamics of strained vanadium dioxide single crystals," *Journal of Applied Physics*, vol. 108, no. 8, p. 083517, Oct. 2010. [Online]. Available: https://pubs.aip.org/jap/article/108/8/083517/935693/Thermodynamics-of-strained-vanadium-dioxide-single

[119] H. Guo, K. Chen, Y. Oh, K. Wang, C. Dejoie, S. A. Syed Asif, O. L. Warren, Z. W. Shan, J. Wu, and A. M. Minor, "Mechanics

and Dynamics of the Strain-Induced M1–M2 Structural Phase Transition in Individual VO $_2$ Nanowires," *Nano Letters*, vol. 11, no. 8, pp. 3207–3213, Aug. 2011. [Online]. Available: https://pubs.acs.org/doi/10.1021/nl201460v

[120] J. P. Pouget, H. Launois, J. P. D'Haenens, P. Merenda, and T. M. Rice, "Electron Localization Induced by Uniaxial Stress in Pure V O 2," *Physical Review Letters*, vol. 35, no. 13, pp. 873–875, Sep. 1975. [Online]. Available: https://link.aps.org/doi/10.1103/PhysRevLett.35.873

[121] X. Li, Z. Yin, X. Zhang, Y. Wang, D. Wang, M. Gao, J. Meng, J. Wu, and J. You, "Epitaxial Liftoff of Wafer-Scale VO_2 Nanomembranes for Flexible, Ultrasensitive Tactile Sensors," *Advanced Materials Technologies*, vol. 4, no. 7, p. 1800695, Jul. 2019. [Online]. Available: https://advanced.onlinelibrary.wiley.com/doi/10.1002/admt.201800695

[122] W. Fang and C.-Y. Lo, "On the thermal expansion coefficients of thin films," *Sensors and Actuators A: Physical*, vol. 84, no. 3, pp. 310–314, Sep. 2000.

[123] J. Laconte, F. Iker, S. Jorez, N. André, J. Proost, T. Pardoen, D. Flandre, and J.-P. Raskin, "Thin films stress extraction using micromachined structures and wafer curvature measurements," *Microelectronic Engineering*, vol. 76, no. 1-4, pp. 219–226, Oct. 2004.

[124] U. Bhaskar, V. Passi, S. Houri, E. Escobedo-Cousin, S. H. Olsen, T. Pardoen, and J.-P. Raskin, "On-chip tensile testing of nanoscale silicon free-standing beams," *Journal of Materials Research*, vol. 27, no. 3, pp. 571–579, Feb. 2012.

[125] T. Zabel, R. Geiger, E. Marin, E. Müller, A. Diaz, C. Bonzon, M. J. Süess, R. Spolenak, J. Faist, and H. Sigg, "Top-down method to introduce ultra-high elastic strain," *Journal of Materials Research*, vol. 32, no. 4, pp. 726–736, Feb. 2017.

[126] A. Barlian, W.-T. Park, J. Mallon, A. Rastegar, and B. Pruitt, "Review: Semiconductor Piezoresistance for Microsystems," *Proceedings of the IEEE*, vol. 97, no. 3, pp. 513–552, Mar. 2009.

[127] N. Inomata, N. Van Toan, M. Toda, and T. Ono, "Evaluation of Piezoresistive Property of Vanadium Oxide Thin Film Deposited by Sputter-

ing," *IEEE Sensors Letters*, vol. 2, no. 1, pp. 1–4, Mar. 2018, conference Name: IEEE Sensors Letters.

[128] J. Su, X. Zhang, G. Zhou, J. Gu, C. Xia, Z.-F. Zhou, and Q.-A. Huang, "Fabrication of a Piezoresistive Barometric Pressure Sensor by a Silicon-on-Nothing Technology," *Journal of Sensors*, vol. 2019, no. 1, p. 5408268, 2019.

[129] R. Yang, J. Lee, S. Ghosh, H. Tang, R. M. Sankaran, C. A. Zorman, and P. X.-L. Feng, "Tuning Optical Signatures of Single- and Few-Layer MoS_2 by Blown-Bubble Bulge Straining up to Fracture," *Nano Letters*, vol. 17, no. 8, pp. 4568–4575, Aug. 2017.

[130] A. K. Katiyar, K. Y. Thai, W. S. Yun, J. Lee, and J.-H. Ahn, "Breaking the absorption limit of Si toward SWIR wavelength range via strain engineering," *Science Advances*, vol. 6, no. 31, p. eabb0576, Jul. 2020. [Online]. Available: https://www.science.org/doi/10.1126/sciadv.abb0576

[131] H. Han, Y. Cheng, C. Fang, T. Zhao, J. Liu, and H. Du, "Flexible Strain Sensors Based on Direct-Writing VO_2 Nanobelts Inks for Monitoring Human Motions and Human–Machine Interaction," *ACS Applied Nano Materials*, vol. 6, no. 16, pp. 14 680–14 691, Aug. 2023. [Online]. Available: https://pubs.acs.org/doi/10.1021/acsanm.3c02020

[132] Z. Ma, S. Yan, F. Chen, Y. Dai, Z. Liu, K. Xu, T. Xu, Z. Tong, M. Chen, L. Wang, P. Wang, L. Sun, B. Cheng, S.-J. Liang, and F. Miao, "Ultrasensitive Mechanical Sensor Using Tunable Ordered Array of Metallic and Insulating States in Vanadium Dioxide," *Chinese Physics Letters*, vol. 41, no. 7, p. 077101, Jul. 2024. [Online]. Available: https://iopscience.iop.org/article/10.1088/0256-307X/41/7/077101

[133] H. Okaniwa, K. Nakatani, M. Yano, M. Asano, and K. Suzuki, "Preparation and Properties of a-Si: H Solar Cells on Organic Polymer Film Substrate," *Japanese Journal of Applied Physics*, vol. 21, no. S2, p. 239, Jan. 1982.

[134] S. Gupta, W. T. Navaraj, L. Lorenzelli, and R. Dahiya, "Ultra-thin chips for high-performance flexible electronics," *npj Flexible Electronics*, vol. 2, no. 1, p. 8, Mar. 2018.

[135] J. Biggs, J. Myers, J. Kufel, E. Ozer, S. Craske, A. Sou, C. Ramsdale, K. Williamson, R. Price, and S. White, "A natively flexible 32-bit Arm microprocessor," *Nature*, vol. 595, no. 7868, pp. 532–536, Jul. 2021, number: 7868 Publisher: Nature Publishing Group.

[136] H. C. Ko, M. P. Stoykovich, J. Song, V. Malyarchuk, W. M. Choi, C.-J. Yu, J. B. Geddes III, J. Xiao, S. Wang, Y. Huang, and J. A. Rogers, "A hemispherical electronic eye camera based on compressible silicon optoelectronics," *Nature*, vol. 454, no. 7205, pp. 748–753, Aug. 2008.

[137] Q. Guo, Z. Di, M. G. Lagally, and Y. Mei, "Strain engineering and mechanical assembly of silicon/germanium nanomembranes," *Materials Science and Engineering: R: Reports*, vol. 128, pp. 1–31, Jun. 2018.

[138] Y. Zhang, W. Xiong, W. Chen, and Y. Zheng, "Recent Progress on Vanadium Dioxide Nanostructures and Devices: Fabrication, Properties, Applications and Perspectives," *Nanomaterials*, vol. 11, no. 2, p. 338, Jan. 2021. [Online]. Available: https://www.mdpi.com/2079-4991/11/2/338

[139] C. Cao, B. Hu, G. Tu, X. Ji, Z. Li, F. Xu, T. Chang, P. Jin, and X. Cao, "Sputtering Flexible VO_2 Films for Effective Thermal Modulation," *ACS Applied Materials & Interfaces*, vol. 14, no. 24, pp. 28 105–28 113, Jun. 2022. [Online]. Available: https://pubs.acs.org/doi/10.1021/acsami.2c05482

[140] Y. Du, C. Wheeler, C. H. K. De Groot, O. L. Muskens, X. Fang, and K. Sun, "Low-temperature vanadium dioxide for CMOS integration and flexible polyimide applications," *Optical Materials Express*, vol. 15, no. 3, p. 465, Mar. 2025. [Online]. Available: https://opg.optica.org/abstract.cfm?URI=ome-15-3-465

[141] D. H. Jung, H. S. So, J. S. Ahn, H. Lee, T. T. T. Nguyen, S. Yoon, S. Y. Kim, and H.-Y. Jung, "Low temperature growth of amorphous VO2 films on flexible polyimide substrates with a TiO2 buffer layer," *Journal of Vacuum Science & Technology A: Vacuum, Surfaces, and Films*, vol. 36, no. 3, p. 03E102, May 2018. [Online]. Available: https://pubs.aip.org/jva/article/36/3/03E102/443074/Low-temperature-growth-of-amorphous-VO2-films-on

[142] Q. Chang, D. Wang, Z. Zhao, C. Ling, C. Wang, H. Jin, and J. Li, "Size-Controllable M-Phase VO_2 Nanocrystals for Flexible

Thermochromic Energy-Saving Windows," *ACS Applied Nano Materials*, vol. 4, no. 7, pp. 6778–6785, Jul. 2021. [Online]. Available: https://pubs.acs.org/doi/10.1021/acsanm.1c00835

[143] H. Han, C. Fang, Y. Cheng, J. Liu, M. Li, X. Zhang, Y. Zhao, and X. Yao, "Temperature-Switching Flexible Strain Sensors Based on Vanadium Dioxide for Intelligent Packaging Applications," *ACS Applied Materials & Interfaces*, p. acsami.4c04519, Jul. 2024. [Online]. Available: https://pubs.acs.org/doi/10.1021/acsami.4c04519

[144] Y. Wang, Y. Hong, X. Hu, Y. Ye, P. Wang, J. Luo, A. Yin, Z. Ren, H. Liu, X. Qi, J. Liu, S. He, S. Yu, and J. Wei, "Flexible Fabric Temperature Sensor Based on Vo_2 /Pedot:Pss with High Performance," *Advanced Materials Technologies*, vol. 8, no. 21, p. 2300898, Nov. 2023. [Online]. Available: https://onlinelibrary.wiley.com/doi/10.1002/admt.202300898

[145] T. Chang, Y. Zhu, C. Cao, C. Yang, H. Luo, P. Jin, and X. Cao, "Multifunctional Flexible Vanadium Dioxide Films," *Accounts of Materials Research*, vol. 2, no. 9, pp. 714–725, Sep. 2021. [Online]. Available: https://pubs.acs.org/doi/10.1021/accountsmr.1c00044

[146] Y. Li, H. Ma, R. Shi, Y. Wu, S. Feng, Y. Fu, Y. Wei, X. Zhao, K. Dong, K. Jiang, K. Liu, and X. Zhang, "Wafer-Scale Transfer and Integration of Tungsten-Doped Vanadium Dioxide Films," *ACS Nano*, p. acsnano.4c15059, Feb. 2025. [Online]. Available: https://pubs.acs.org/doi/10.1021/acsnano.4c15059

[147] E.-N. Sirjita, A. Boulle, J.-C. Orlianges, R. Mayet, and A. Crunteanu, "Structural and electrical properties of high-performance vanadium dioxide thin layers obtained by reactive magnetron sputtering," *Thin Solid Films*, vol. 759, p. 139461, Oct. 2022. [Online]. Available: https://linkinghub.elsevier.com/retrieve/pii/S0040609022003753

[148] A. Varini, C. Masserey, V. Conti, Z. Saadat Somaehsofla, E. Ansari, I. Stolichnov, and A. M. Ionescu, "Pulsed Laser and Atomic Layer Deposition of CMOS-Compatible Vanadium Dioxide: Enabling Ultrathin Phase-Change Films," *ACS Applied Electronic Materials*, Jul. 2025, publisher: American Chemical Society (ACS). [Online]. Available: https://pubs.acs.org/doi/10.1021/acsaelm.5c01132

[149] Z. S. Somaehsofla, C. Masserey, A. Varini, D. Flandre, and A. M. Ionescu, "Wafer-Scale Demonstration of a Highly Sensitive Srain Sensor Based on Polycrystalline VO2."

[150] R. Sharangpani, K. Cherukuri, and R. Singh, "Low thermal budget processing of organic dielectrics," *IEEE Transactions on Electron Devices*, vol. 43, no. 7, pp. 1168–1170, Jul. 1996. [Online]. Available: http://ieeexplore.ieee.org/document/502430/

[151] V. Daghigh, H. Daghigh, and R. Harrison, "High-Temperature Polyimide Composites—A Review on Polyimide Types, Manufacturing, and Mechanical and Thermal Behavior," *Journal of Composites Science*, vol. 9, no. 10, p. 526, Oct. 2025. [Online]. Available: https://www.mdpi.com/2504-477X/9/10/526

[152] Y. Liu, J. Liu, Y. Li, D. Wang, L. Ren, and K. Zou, "Effect of annealing temperature on the structure and properties of vanadium oxide films," *Optical Materials Express*, vol. 6, no. 5, p. 1552, May 2016. [Online]. Available: https://opg.optica.org/abstract.cfm?URI=ome-6-5-1552

[153] D. Liu, P. Yang, Y. Zhang, Y. Chen, H. Dai, T. Li, R. Xue, J. Chen, Y. Su, and Z. Chen, "Effects of microdefects and grain size on the phase transition properties of Nano-VO2(M)," *Journal of Solid State Chemistry*, vol. 288, p. 121450, Aug. 2020. [Online]. Available: https://linkinghub.elsevier.com/retrieve/pii/S0022459620302802

[154] N. Bidoul, N. Roisin, and D. Flandre, "Tuning the Intrinsic Stochasticity of Resistive Switching in VO_2 Microresistors," *Nano Letters*, vol. 24, no. 21, pp. 6201–6209, May 2024. [Online]. Available: https://pubs.acs.org/doi/10.1021/acs.nanolett.4c00184

[155] V. Kaajakari, *Practical MEMS*. Las Vegas, NV, USA: Small gear Publishing, 2009.

[156] F. R. M. Rashidi, O. Hussein, and W. Z. W. Hasan, "Investigation on developing of a piezoresistive pressure sensor for foot plantar measurement system," pp. 1–4, Aug. 2015.

[157] V. Belwanshi, "Analytical modeling to estimate the sensitivity of MEMS technology-based piezoresistive pressure sensor," *Journal of Computational Electronics*, vol. 20, no. 1, pp. 668–680, Feb. 2021. [Online]. Available: http://link.springer.com/10.1007/s10825-020-01592-5

[158] V. Belwanshi and A. Topkar, "Quantitative Analysis of MEMS Piezoresistive Pressure Sensors Based on Wide Band Gap Materials," *IETE Journal of Research*, vol. 68, no. 1, pp. 667–677, Jan. 2022.

[159] V. Belwanshi, S. Philip, and A. Topkar, "Performance Study of MEMS Piezoresistive Pressure Sensors at Elevated Temperatures," *IEEE Sensors Journal*, vol. 22, no. 10, pp. 9313–9320, May 2022.

[160] N. Sepúlveda, A. Rúa, R. Cabrera, and F. Fernández, "Young's modulus of VO2 thin films as a function of temperature including insulator-to-metal transition regime," *Applied Physics Letters*, vol. 92, no. 19, p. 191913, May 2008. [Online]. Available: https://pubs.aip.org/apl/article/92/19/191913/969365/Young-s-modulus-of-VO2-thin-films-as-a-function-of

[161] P. Jin, S. Nakao, S. Tanemura, T. Bell, L. Wielunski, and M. Swain, "Characterization of mechanical properties of VO2 thin films on sapphire and silicon by ultra-microindentation," *Thin Solid Films*, vol. 343-344, pp. 134–137, Apr. 1999. [Online]. Available: https://linkinghub.elsevier.com/retrieve/pii/S0040609098016460

[162] W. Fan, S. Huang, J. Cao, E. Ertekin, C. Barrett, D. R. Khanal, J. C. Grossman, and J. Wu, "Superelastic metal-insulator phase transition in single-crystal VO 2 nanobeams," *Physical Review B*, vol. 80, no. 24, p. 241105, Dec. 2009. [Online]. Available: https://link.aps.org/doi/10.1103/PhysRevB.80.241105

[163] R. Loudon and N. Kurti, "Theory of the first-order Raman effect in crystals," *Proceedings of the Royal Society of London. Series A. Mathematical and Physical Sciences*, vol. 275, no. 1361, pp. 218–232, 1963.

[164] J. H. Parker, D. W. Feldman, and M. Ashkin, "Raman Scattering by Silicon and Germanium," *Physical Review*, vol. 155, no. 3, pp. 712–714, Mar. 1967.

[165] N. Roisin, M.-S. Colla, J.-P. Raskin, and D. Flandre, "Raman strain–shift measurements and prediction from first-principles in highly strained silicon," *Journal of Materials Science: Materials in Electronics*, vol. 34, no. 5, p. 373, Feb. 2023.

[166] J. Su, X. Zhang, G. Zhou, J. Gu, C. Xia, Z.-F. Zhou, and Q.-A. Huang, "Fabrication of a Piezoresistive Barometric Pressure

Sensor by a Silicon-on-Nothing Technology," *Journal of Sensors*, vol. 2019, pp. 1–10, Apr. 2019. [Online]. Available: https://www.hindawi.com/journals/js/2019/5408268/

[167] T. Sterken, J. Vanfleteren, T. Torfs, M. Op de Beeck, F. Bossuyt, and C. Van Hoof, "Ultra-Thin Chip Package (UTCP) and stretchable circuit technologies for wearable ECG system," pp. 6886–6889, Aug. 2011.

[168] HDMicroSystems. (2026) PI2545 Polyimide. [Online]. Available: https://www.hdmicrosystems.com/products/pi2545

[169] HDMicroSystems. (2026) VM651 and VM652 Adhesion Promoters. [Online]. Available: https://www.hdmicrosystems.com/

[170] Merck, *AZ MIF Developers: Technical Datasheet*, Merck, Darmstadt, Germany, 03 2021, technical Datasheet, Rev. 03/21. [Online]. Available: https://www.microchemicals.com/dokumente/datenblaetter/tds/merck/en/tds_az_mif_developer.pdf

[171] *AZ MiR 701 Series: Positive Tone Photoresist*, Merck, Darmstadt, Germany, 03 2021, technical Datasheet, Rev. 03/21. [Online]. Available: https://www.microchemicals.com/dokumente/datenblaetter/tds/merck/en/tds_az_mir701_series.pdf

[172] Micro-Measurements. (2026) B-127: Strain gage installations with M-Bond 200 adhesive-3. [Online]. Available: https://www.micro-measurements.com/knowledge-base/instruction-bulletins

[173] Halstrup. (2026) Product bulletin kal100. [Online]. Available: https://www.halstrup-walcher.de/en/

[174] Polytec. (2026) White-light interferometry. [Online]. Available: https://www.polytec.com/us/surface-metrology/technology/white-light-interferometry

[175] C. O Mahony, M. Hill, M. Brunet, R. Duane, and A. Mathewson, "Characterization of micromechanical structures using white-light interferometry," *Measurement Science and Technology*, vol. 14, no. 10, pp. 1807–1814, Oct. 2003.

[176] G. Abadias, E. Chason, J. Keckes, M. Sebastiani, G. B. Thompson, E. Barthel, G. L. Doll, C. E. Murray, C. H. Stoessel, and L. Martinu, "Review Article: Stress in thin films and coatings: Current status,

challenges, and prospects," *Journal of Vacuum Science & Technology A: Vacuum, Surfaces, and Films*, vol. 36, no. 2, p. 020801, Mar. 2018. [Online]. Available: https://pubs.aip.org/jva/article/36/2/020801/246484/Review-Article-Stress-in-thin-films-and-coatings

[177] W. K. Schomburg, *Introduction to Microsystem Design*, ser. RWTHedition. Berlin, Heidelberg: Springer Berlin Heidelberg, 2011, vol. 1. [Online]. Available: https://link.springer.com/10.1007/978-3-642-19489-4

[178] D. Maier-Schneider, J. Maibach, and E. Obermeier, "A new analytical solution for the load-deflection of square membranes," *Journal of Microelectromechanical Systems*, vol. 4, no. 4, pp. 238–241, Dec. 1995. [Online]. Available: http://ieeexplore.ieee.org/document/475551/

[179] L. Lahaye, N. Roisin, N. André, D. Flandre, and J.-P. Raskin, "Design, Fabrication, Modeling and Characterization of a Polyimide-Based Membrane for High Strain Studies in Microfabricated Devices," *IEEE Transactions on Materials for Electron Devices*, vol. 2, pp. 26–33, 2025. [Online]. Available: https://ieeexplore.ieee.org/document/10948909/

[180] A. K. Katiyar, B. J. Kim, G. Lee, Y. Kim, J. S. Kim, J. M. Kim, S. Nam, J. Lee, H. Kim, and J.-H. Ahn, "Strain modulation in crumpled Si nanomembranes: Light detection beyond the Si absorption limit," *Science Advances*, vol. 10, no. 2, p. eadg7200, Jan. 2024. [Online]. Available: https://www.science.org/doi/10.1126/sciadv.adg7200

[181] H. Xiao and L. S. Chen, "Hencky's elasticity model and linear stress-strain relations in isotropic finite hyperelasticity," *Acta Mechanica*, vol. 157, no. 1-4, pp. 51–60, Mar. 2002. [Online]. Available: http://link.springer.com/10.1007/BF01182154

[182] L. Lahaye, N. Roisin, J.-P. Raskin, and D. Flandre, "Accurate estimation of Young's modulus of VO2 thin film integrated on polyimide for high strain studies," 2024.

[183] Comsol. (2017) COMSOL Multiphysics Structural Mechanics Module User's Guide. [Online]. Available: https://doc.comsol.com/5.3a/doc/com.comsol.help.sme/StructuralMechanicsModuleUsersGuide.pdf

[184] S. Tu, X. Ren, J. He, and Z. Zhang, "Stress–strain curves of metallic materials and post-necking strain hardening characterization: A review," *Fatigue & Fracture of Engineering Materials & Structures*, vol. 43, no. 1, pp. 3–19, 2020.

[185] S. Franssila, *Introduction to Microfabrication*. Hoboken, NJ, USA: Wiley, 2010.

[186] W. A. Brantley, "Calculated elastic constants for stress problems associated with semiconductor devices," *Journal of Applied Physics*, vol. 44, no. 1, pp. 534–535, 01 1973. [Online]. Available: https://doi.org/10.1063/1.1661935

[187] M. A. Hopcroft, W. D. Nix, and T. W. Kenny, "What is the Young's Modulus of Silicon?" *Journal of Microelectromechanical Systems*, vol. 19, no. 2, pp. 229–238, Apr. 2010.

[188] J. Lubliner, *Plasticity Theory*, ser. Dover Books on Engineering. New York, NY, USA: Dover Publications, 1990.

[189] H. S. Virk, P. S. Chandi, and A. K. Srivastava, "Physical and chemical response of 70 MeV carbon ion irradiated Kapton-H polymer," *Bulletin of Materials Science*, vol. 24, no. 5, pp. 529–534, Oct. 2001.

[190] I. Savatinova, S. Tonchev, R. Todorov, E. Venkova, E. Liarokapis, and E. Anastassakis, "Polyimide thin-film waveguides: Optical and Raman spectroscopic studies," *Journal of Applied Physics*, vol. 67, no. 4, pp. 2051–2055, Feb. 1990.

[191] I. D. Wolf, "Micro-Raman spectroscopy to study local mechanical stress in silicon integrated circuits," *Semiconductor Science and Technology*, vol. 11, no. 2, pp. 139–154, Feb. 1996.

[192] S. Ganesan, A. Maradudin, and J. Oitmaa, "A lattice theory of morphic effects in crystals of the diamond structure," *Annals of Physics*, vol. 56, no. 2, pp. 556–594, Feb. 1970.

[193] E. Anastassakis, A. Pinczuk, and E. Burstein, "Effect of static uniaxial stress on the Raman spectrum of silicon," vol. 8, no. 2.

[194] C.-Y. Peng, C.-F. Huang, Y.-C. Fu, Y.-H. Yang, C.-Y. Lai, S.-T. Chang, and C. W. Liu, "Comprehensive study of the Raman shifts of strained silicon and germanium," *Journal of Applied Physics*, vol. 105, no. 8, p. 083537, 04 2009.

[195] Y.-Y. Fang, J. Tolle, R. Roucka, A. V. G. Chizmeshya, J. Kouvetakis, V. R. D'Costa, and J. Menéndez, "Perfectly tetragonal, tensile-strained Ge on Ge1ySny buffered Si(100)," *Applied Physics Letters*, vol. 90, no. 6, p. 061915, Feb. 2007.

[196] A. Shchepetov, M. Prunnila, F. Alzina, L. Schneider, J. Cuffe, H. Jiang, E. I. Kauppinen, C. M. Sotomayor Torres, and J. Ahopelto, "Ultra-thin free-standing single crystalline silicon membranes with strain control," *Applied Physics Letters*, vol. 102, no. 19, p. 192108, May 2013.

[197] W. S. Yoo, H. Harima, and M. Yoshimoto, "Polarized Raman Signals from Si Wafers: Dependence of In-Plane Incident Orientation of Probing Light," *ECS Journal of Solid State Science and Technology*, vol. 4, no. 9, pp. P356–P363, 2015.

[198] U. Ramabadran and B. Roughani, "Intensity analysis of polarized Raman spectra for off axis single crystal silicon," *Materials Science and Engineering: B*, vol. 230, pp. 31–42, Apr. 2018.

[199] G. Fu, A. Polity, N. Volbers, and B. K. Meyer, "Annealing effects on VO2 thin films deposited by reactive sputtering," *Thin Solid Films*, vol. 515, no. 4, pp. 2519–2522, Dec. 2006. [Online]. Available: https://linkinghub.elsevier.com/retrieve/pii/S0040609006005888

[200] K. Sieradzka, D. Wojcieszak, D. Kaczmarek, J. Domaradzki, G. Kiriakidis, E. Aperathitis, V. Kambilafka, F. Placido, and S. Song, "Structural and optical properties of vanadium oxides prepared by microwave-assisted reactive magnetron sputtering," *Optica Applicata*, vol. 41, no. 2, pp. 463–469, 2011.

[201] D. Kim, M. Kim, J. Yi, S.-H. Nam, J.-H. Boo, Y. S. Park, and J. Lee, "Growth and Characterization of VO_2 Thin Film by Pulsed DC Sputtering of Optical Switching Applications," *Science of Advanced Materials*, vol. 9, no. 8, pp. 1415–1419, Aug. 2017. [Online]. Available: http://www.ingentaconnect.com/content/10.1166/sam.2017.2937

[202] S. S. Maklakov, V. I. Polozov, S. A. Maklakov, A. D. Mishin, I. A. Ryzhikov, A. L. Trigub, V. A. Amelichev, K. I. Maslakov, and V. N. Kisel, "Post-deposition annealing of thin RF magnetron sputter-deposited VO2 films above the melting point," *Journal of Alloys and Compounds*, vol. 763, pp. 558–569, Sep. 2018. [Online]. Available: https://linkinghub.elsevier.com/retrieve/pii/S0925838818321248

[203] N. Bidoul, "Potential of vanadium dioxide for artificial sensory neurons," PhD Thesis, Université catholique de Louvain (UCLouvain), Louvain-la-Neuve, Belgium, October 2024, defence date: 17 October 2024. Supervised by Denis Flandre. Chapter 2, pp. 45–51.

[204] L. Van Brandt, N. Bidoul, T. Ratier, X. Zeng, J.-C. Delvenne, and D. Flandre, "Experimental Demonstration of a Temperature-Sensitive VO_2 Memristor-Based Spiking Circuit in Stochastic Bursting Regime," pp. 1–5, Feb. 2026. [Online]. Available: https://ieeexplore.ieee.org/document/11457126/

[205] AJA International, Inc. (2024) Orion Series Sputtering Systems. [Online]. Available: https://www.ajaint.com/orion-series

[206] C. Lehmann and P. Sigmund, "On the Mechanism of Sputtering," *physica status solidi (b)*, vol. 16, no. 2, pp. 507–511, Jan. 1966. [Online]. Available: https://onlinelibrary.wiley.com/doi/10.1002/pssb.19660160216

[207] P. Sigmund, "Theory of Sputtering. I. Sputtering Yield of Amorphous and Polycrystalline Targets," *Physical Review*, vol. 184, no. 2, pp. 383–416, Aug. 1969. [Online]. Available: https://link.aps.org/doi/10.1103/PhysRev.184.383

[208] S. Swann, "Magnetron Sputtering," *Physics in Technology*, vol. 19, no. 2, pp. 67–75, 1988, article téléchargé depuis IOPscience le 16/07/2013. [Online]. Available: http://iopscience.iop.org/0305-4624/19/2/304

[209] S. Franssila, *Introduction to Microfabrication*, 2nd ed. Chichester, West Sussex, England ; Hoboken, NJ: John Wiley & Sons, Ltd, 2010, chapter 33 : "Vacuum and Plasma" (pp. 428–430).

[210] ——, *Introduction to Microfabrication*, 2nd ed. Chichester, West Sussex, England ; Hoboken, NJ: John Wiley & Sons, Ltd, 2010, chapter 5: "Thin-film Materials and Processes" (pp. 57–58).

[211] A. Thomann, C. Vahlas, L. Aloui, D. Samelor, A. Caillard, N. Shaharil, R. Blanc, and E. Millon, "Conformity of Aluminum Thin Films Deposited onto Micro-Patterned Silicon Wafers by Pulsed Laser Deposition, Magnetron Sputtering, and CVD," *Chemical Vapor Deposition*, vol. 17, no. 10-12, pp. 366–374, Dec. 2011. [Online]. Available: https://onlinelibrary.wiley.com/doi/10.1002/cvde.201106936

[212] Neyco. (2026) Sputtering Targets. [Online]. Available: https://www.neyco.fr/en/our-products/materials/targets/sputtering-targets/materiaux/cibles/cibles-de-pulverisation/cibles-base-vanadium-v

[213] W. Sproul, D. Christie, and D. Carter, "Control of reactive sputtering processes," *Thin Solid Films*, vol. 491, no. 1-2, pp. 1–17, Nov. 2005. [Online]. Available: https://linkinghub.elsevier.com/retrieve/pii/S0040609005005389

[214] S. Berg and T. Nyberg, "Fundamental understanding and modeling of reactive sputtering processes," *Thin Solid Films*, vol. 476, no. 2, pp. 215–230, Apr. 2005. [Online]. Available: https://linkinghub.elsevier.com/retrieve/pii/S0040609004016876

[215] D. Depla and S. Mahieu, Eds., *Reactive Sputter Deposition*, ser. Springer Series in Materials Science. Berlin Heidelberg: Springer, 2008, no. 109.

[216] V. I. Shapovalov, "Modeling of Reactive Sputtering—History and Development," *Materials*, vol. 16, no. 8, p. 3258, Apr. 2023. [Online]. Available: https://www.mdpi.com/1996-1944/16/8/3258

[217] Y. Hong-Tao, F. Ke-Cheng, W. Xue-Jin, L. Chao, H. Chen-Juan, and N. Yu-Xin, "Effect of nonstoichiometry on Raman scattering of VO_2 films," *Chinese Physics*, vol. 13, no. 1, pp. 82–84, Jan. 2004. [Online]. Available: https://iopscience.iop.org/article/10.1088/1009-1963/13/1/015

[218] P. Shvets, O. Dikaya, K. Maksimova, and A. Goikhman, "A review of Raman spectroscopy of vanadium oxides," *Journal of Raman Spectroscopy*, vol. 50, no. 8, pp. 1226–1244, Aug. 2019. [Online]. Available: https://onlinelibrary.wiley.com/doi/10.1002/jrs.5616

[219] Q. Van Overmeere and S. Ramanathan, "Thin film fuel cells with vanadium oxide anodes: Strain and stoichiometry effects," *Electrochimica Acta*, vol. 150, pp. 83–88, Dec. 2014. [Online]. Available: https://linkinghub.elsevier.com/retrieve/pii/S0013468614021732

[220] S. Lafane, T. Kerdja, S. Abdelli-Messaci, Y. Khereddine, M. Kechouane, and O. Nemraoui, "Correlation of plume dynamics and oxygen pressure with VO2 stoichiometry during pulsed laser deposition," *Applied Physics A*, vol. 112, no. 1, pp. 159–164, Jul. 2013. [Online]. Available: http://link.springer.com/10.1007/s00339-012-7223-9

[221] D. Depla and R. De Gryse, "Target poisoning during reactive magnetron sputtering: Part I: the influence of ion implantation," *Surface and Coatings Technology*, vol. 183, no. 2-3, pp. 184–189, May 2004. [Online]. Available: https://linkinghub.elsevier.com/retrieve/pii/S0257897203011344

[222] M. Waite and S. I. Shah, "Target poisoning during reactive sputtering of silicon with oxygen and nitrogen," *Materials Science and Engineering: B*, vol. 140, no. 1-2, pp. 64–68, May 2007. [Online]. Available: https://linkinghub.elsevier.com/retrieve/pii/S0921510707001924

[223] "Commercial quartz crystal microbalances – theory and applications," *Biosensors and Bioelectronics*, vol. 14, no. 8, pp. 663–670, 1999. [Online]. Available: https://www.sciencedirect.com/science/article/pii/S0956566399000408

[224] A. Yalin, B. Rubin, J. Topper, and C. Farnell, "Differential Sputter Yield Measurements of Single-and Multi-Element Targets due to Ion Beam Bombardment," 2009.

[225] Y. Wang, M. Li, and L. Zhao, "The effects of vacuum annealing on the structure of VO2 thin films," *Surface and Coatings Technology*, vol. 201, no. 15, pp. 6772–6776, Apr. 2007. [Online]. Available: https://linkinghub.elsevier.com/retrieve/pii/S0257897206010942

[226] Y. Guo, H. Xu, C. Zou, Z. Yang, B. Tong, J. Yu, Y. Zhang, L. Zhao, and Y. Wang, "Evolution of structure and electrical properties with annealing time in solution-based VO2 thin films," *Journal of Alloys and Compounds*, vol. 622, pp. 913–917, Feb. 2015. [Online]. Available: https://linkinghub.elsevier.com/retrieve/pii/S092583881402670X

[227] A. Varini, C. Masserey, V. Conti, Z. S. Somaehsofla, E. Ansari, and A. M. Ionescu, "CMOS-compatible vanadium dioxide via Pulsed Laser and Atomic Layer deposition: towards ultra- thin film phase-change layers."

[228] J. Jian, W. Zhang, C. Jacob, A. Chen, H. Wang, J. Huang, and H. Wang, "Roles of grain boundaries on the semiconductor to metal phase transition of VO2 thin films," *Applied Physics Letters*, vol. 107, no. 10, p. 102105, Sep. 2015. [Online]. Available: https://pubs.aip.org/apl/article/107/10/102105/28630/Roles-of-grain-boundaries-on-the-semiconductor-to

[229] C. Zhang, Y. Guo, Z. Yang, L. Liu, K. Guo, J. Bai, H. Liu, Y. Xiao, L. Hu, Q. Hu, and Q. Wang, "Effect of oxygen flow rate on magnetron-sputtering-based preparation and photoelectric properties of vanadium dioxide films," *Thin Solid Films*, vol. 809, p. 140595, Jan. 2025. [Online]. Available: https://linkinghub.elsevier.com/retrieve/pii/S0040609024003961

[230] H. F Mahmood, S. A. Ahmad, and M. Abu-Bakr, "Comprehensive Overview of X-Ray Diffraction: Principles, Techniques, and Applications in Material Science," *Technobius Physics*, vol. 3, no. 3, p. 0035, Aug. 2025. [Online]. Available: https://www.technobius.kz/index.php/phys/article/view/260

[231] G. Gopalakrishnan, D. Ruzmetov, and S. Ramanathan, "On the triggering mechanism for the metal–insulator transition in thin film VO2 devices: electric field versus thermal effects," *Journal of Materials Science*, vol. 44, no. 19, pp. 5345–5353, Oct. 2009. [Online]. Available: https://link.springer.com/10.1007/s10853-009-3442-7

[232] C. Xu, C. Jin, Z. Chen, Q. Lu, Y. Cheng, B. Zhang, F. Qi, J. Chen, X. Yin, G. Wang, D. Xiang, and D. Qian, "Transient dynamics of the phase transition in VO2 revealed by mega-electron-volt ultrafast electron diffraction," *Nature Communications*, vol. 14, no. 1, p. 1265, Mar. 2023. [Online]. Available: https://www.nature.com/articles/s41467-023-37000-2

[233] Y. Zhou, S. Su, Z. Zhu, D. Hou, H. Zhang, and Y. Cao, "Thermal-stimulated phase transition of vanadium dioxide enabling versatile transduction and smart applications," *Journal of Applied Physics*, vol. 136, no. 13, p. 130901, Oct. 2024. [Online]. Available: https://pubs.aip.org/jap/article/136/13/130901/3315294/Thermal-stimulated-phase-transition-of-vanadium

[234] M. J. Miller and J. Wang, "Influence of grain size on transition temperature of thermochromic VO2," *Journal of Applied Physics*, vol. 117, no. 3, p. 034307, Jan. 2015. [Online]. Available: https://pubs.aip.org/jap/article/117/3/034307/167619/Influence-of-grain-size-on-transition-temperature

[235] K. M. Niang, G. Bai, H. Lu, and J. Robertson, "Microstructure scaling of metal–insulator transition properties of VO2 films," *Applied Physics*

Letters, vol. 118, no. 12, p. 121901, Mar. 2021. [Online]. Available: https://pubs.aip.org/apl/article/118/12/121901/39671/Microstructure-scaling-of-metal-insulator

[236] A. Ainabayev, D. Mullarkey, B. Walls, D. Caffrey, K. Zhussupbekov, A. Zhussupbekova, C. Ilhan, A. Kaisha, P. Biswas, A. Tikhonov, O. Murtagh, and I. Shvets, "Epitaxial Grown VO_2 with Suppressed Hysteresis and Low Room Temperature Resistivity for High-Performance Thermal Sensor Applications," *ACS Applied Nano Materials*, vol. 6, no. 4, pp. 2917–2927, Feb. 2023. [Online]. Available: https://pubs.acs.org/doi/10.1021/acsanm.2c05297

[237] T. Hull, J. Colligon, and A. Hill, "Measurement of thin film adhesion," *Vacuum*, vol. 37, no. 3-4, pp. 327–330, Jan. 1987. [Online]. Available: https://linkinghub.elsevier.com/retrieve/pii/0042207X87900182

[238] O. Tabata, K. Kawahata, S. Sugiyama, and I. Igarashi, "Mechanical property measurements of thin films using load-deflection of composite rectangular membranes," *Sensors and Actuators*, vol. 20, no. 1-2, pp. 135–141, Nov. 1989. [Online]. Available: https://linkinghub.elsevier.com/retrieve/pii/0250687489871112

[239] J. Vlassak and W. Nix, "A new bulge test technique for the determination of Young's modulus and Poisson's ratio of thin films," *Journal of Materials Research*, vol. 7, no. 12, pp. 3242–3249, Dec. 1992. [Online]. Available: http://link.springer.com/10.1557/JMR.1992.3242

[240] C. Poilane, P. Delobelle, C. Lexcellent, S. Hayashi, and H. Tobushi, "Analysis of the mechanical behavior of shape memory polymer membranes by nanoindentation, bulging and point membrane deflection tests," *Thin Solid Films*, vol. 379, no. 1-2, pp. 156–165, Dec. 2000. [Online]. Available: https://linkinghub.elsevier.com/retrieve/pii/S0040609000014012

[241] Y.-H. Huh, D.-I. Kim, D.-J. Kim, H.-M. Lee, S.-G. Hong, J.-H. Park, and C.-D. Kee, "Measurement of Mechanical Properties of Thin Film by Membrane Deflection Test," *Experimental Mechanics*, vol. 50, no. 4, pp. 429–435, Apr. 2010. [Online]. Available: http://link.springer.com/10.1007/s11340-009-9247-4

[242] S. S. Kumar and B. D. Pant, "Design principles and considerations for the 'ideal' silicon piezoresistive pressure sensor: a focused review," *Microsystem Technologies*, vol. 20, no. 7, pp. 1213–1247, Jul. 2014. [Online]. Available: http://link.springer.com/10.1007/s00542-014-2215-7

[243] HP. (2026) HP4145B. [Online]. Available: https://wiki.epfl.ch/carplat/documents/PDF/HP4145B.pdf

[244] M. El Kurdi, H. Bertin, E. Martincic, M. De Kersauson, G. Fishman, S. Sauvage, A. Bosseboeuf, and P. Boucaud, "Control of direct band gap emission of bulk germanium by mechanical tensile strain," *Applied Physics Letters*, vol. 96, no. 4, p. 041909, Jan. 2010. [Online]. Available: https://pubs.aip.org/apl/article/96/4/041909/132160/Control-of-direct-band-gap-emission-of-bulk

[245] D. Lloyd, X. Liu, J. W. Christopher, L. Cantley, A. Wadehra, B. L. Kim, B. B. Goldberg, A. K. Swan, and J. S. Bunch, "Band Gap Engineering with Ultralarge Biaxial Strains in Suspended Monolayer MoS_2," *Nano Letters*, vol. 16, no. 9, pp. 5836–5841, Sep. 2016. [Online]. Available: https://pubs.acs.org/doi/10.1021/acs.nanolett.6b02615

[246] D. Kang, P. V. Pikhitsa, Y. W. Choi, C. Lee, S. S. Shin, L. Piao, B. Park, K.-Y. Suh, T.-i. Kim, and M. Choi, "Ultrasensitive mechanical crack-based sensor inspired by the spider sensory system," *Nature*, vol. 516, no. 7530, pp. 222–226, Dec. 2014. [Online]. Available: https://www.nature.com/articles/nature14002

[247] F. Di Gioacchino, T. E. J. Edwards, G. N. Wells, and W. J. Clegg, "A new mechanism of strain transfer in polycrystals," *Scientific Reports*, vol. 10, no. 1, p. 10082, Jun. 2020. [Online]. Available: https://www.nature.com/articles/s41598-020-66569-7

[248] D. D. L. Chung, "A critical review of piezoresistivity and its application in electrical-resistance-based strain sensing," *Journal of Materials Science*, vol. 55, no. 32, pp. 15 367–15 396, Nov. 2020. [Online]. Available: https://link.springer.com/10.1007/s10853-020-05099-z

[249] J. M. Atkin, S. Berweger, E. K. Chavez, M. B. Raschke, J. Cao, W. Fan, and J. Wu, "Strain and temperature dependence of the insulating phases of VO 2 near the metal-insulator transition,"

Physical Review B, vol. 85, no. 2, p. 020101, Jan. 2012. [Online]. Available: https://link.aps.org/doi/10.1103/PhysRevB.85.020101

[250] N. Inomata, T. Usuda, Y. Yamamoto, M. H. Zoellner, I. Costina, and T. Ono, "Effects of temperature and doping concentration on the piezoresistive property of vanadium dioxide thin film," *Sensors and Actuators A: Physical*, vol. 346, p. 113823, Oct. 2022. [Online]. Available: https://linkinghub.elsevier.com/retrieve/pii/S0924424722004587

[251] F. S. Irani, A. H. Shafaghi, M. C. Tasdelen, T. Delipinar, C. E. Kaya, G. G. Yapici, and M. K. Yapici, "Graphene as a Piezoresistive Material in Strain Sensing Applications," *Micromachines*, vol. 13, no. 1, p. 119, Jan. 2022. [Online]. Available: https://www.mdpi.com/2072-666X/13/1/119

[252] F. Ureña, S. H. Olsen, and J.-P. Raskin, "Raman measurements of uniaxial strain in silicon nanostructures," *Journal of Applied Physics*, vol. 114, no. 14, p. 144507, Oct. 2013.

[253] U. Kumar Bhaskar, T. Pardoen, V. Passi, and J.-P. Raskin, "Piezoresistance of nano-scale silicon up to 2 GPa in tension," *Applied Physics Letters*, vol. 102, no. 3, p. 031911, 01 2013. [Online]. Available: https://doi.org/10.1063/1.4788919